PROJECT REPORT

DOE Award Number- DE-FC26-06NT42857

1. Performer

University of California Santa Barbara

2. Project Title

High-Efficiency Nitride-Base Photonic Crystal Light Sources

3. Principal Investigators

James S. Speck
Professor
Materials Department
University of California
Santa Barbara, CA 93106
(805) 893-8005 (ph)
speck@mrl.ucsb.edu
Evelyn L. Hu
Professor
Materials Department
University of California
Santa Barbara, CA 93106
Claude Weisbuch
Professor
Materials Department
University of California
Santa Barbara, CA 93106

4. Other Team Members

Yong-Seok Choi (Post-doc) - Currently at Luminus Devices, Inc., USA
Kelly McGroddy - PhD in 2008
Gregor Koblmüller (Post-doc) - Currently at Walter Schottky Institute, Germany
Elison Matioli - PhD in 2010
Elizabeth Rangel - PhD in progress
Fabian Rol (Post-doc) – Currently at Harvard University, USA
Dobri Simeonov (Post-doc)

5. Distribution limitation notices

None

DISCLAIMER

6. Executive summary

The research activities performed in the framework of this project represent a major breakthrough in the demonstration of Photonic Crystals (PhC) as a competitive technology for LEDs with high light extraction efficiency.

The goals of the project were to explore the viable approaches to manufacturability of PhC LEDS through proven standard industrial processes, establish the limits of light extraction by various concepts of PhC LEDs, and determine the possible advantages of PhC LEDs over current and forthcoming LED extraction concepts.

We have developed three very different geometries for PhC light extraction in LEDs. In addition, we have demonstrated reliable methods for their in-depth analysis allowing the extraction of important parameters such as light extraction efficiency, modal extraction length, directionality, internal and external quantum efficiency. The information gained allows better understanding of the physical processes and the effect of the design parameters on the light directionality and extraction efficiency. As a result, we produced LEDs with controllable emission directionality and a state of the art extraction efficiency that goes up to 94%. Those devices are based on embedded air-gap PhC – a novel technology concept developed in the framework of this project. They rely on a simple and planar fabrication process that is very interesting for industrial implementation due to its robustness and scalability. In fact, besides the additional patterning and regrowth steps, the process is identical as that for standard industrially used *p*-side-up LEDs. The final devices exhibit the same good electrical characteristics and high process yield as a series of test standard LEDs obtained in comparable conditions. Finally, the technology of embedded air-gap patterns (PhC) has significant potential in other related fields such as: increasing the optical mode interaction with the active region in semiconductor lasers; increasing the coupling of the incident light into the active region of solar cells; increasing the efficiency of the phosphorous light conversion in white light LEDs *etc.*

In addition to the technology of embedded PhC LEDs, we demonstrate a technique for improvement of the light extraction and emission directionality for existing flip-chip microcavity (thin) LEDs by introducing PhC grating into the top *n*-contact. Although, the performances of these devices in terms of increase of the extraction efficiency are not significantly superior compared to those obtained by other techniques like surface roughening, the use of PhC offers some significant advantages such as improved and controllable emission directionality and a process that is directly applicable to any material system. The PhC microcavity LEDs have also potential for industrial implementation as the fabrication process has only minor differences to that already used for flip-chip thin LEDs. Finally, we have demonstrated that achieving good electrical properties and high fabrication yield for these devices is straightforward.

HIGHLIGHTS

- Large scale nanoimprint fabrication of both surface and embedded photonic crystals demonstrated.

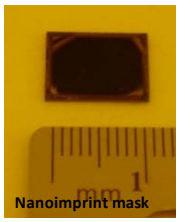

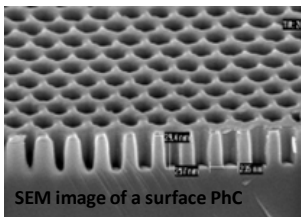

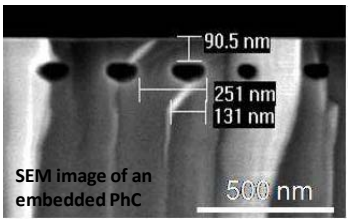

- Basic parameters for efficient light extraction determined and measured.

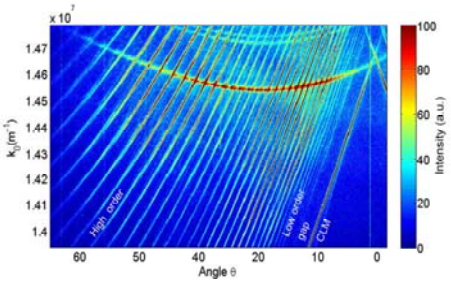

High resolution angular-resolved electroluminescence.

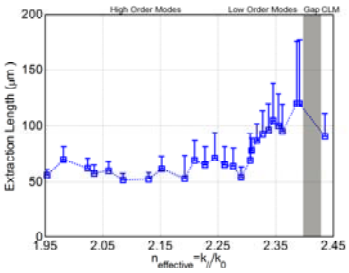

Measurement of the extraction length of different guided modes.

- High directionality of PhC LED demonstrated, with enhancements up to 3.5 times for the vertically outcoupled light.

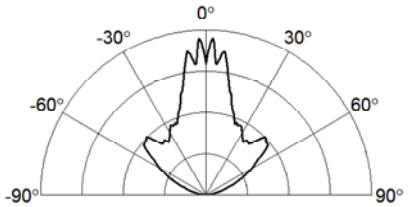

Example of highly directional emission in MC PhC LEDs

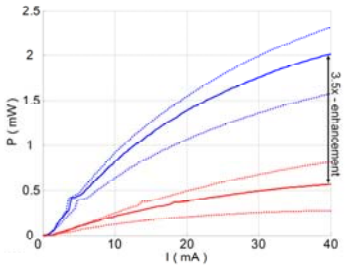

Enhancement of the vertically outcoupled light in Embedded PhC LEDs

- Near unity (94%) extraction efficiency demonstrated in a planar, scalable fabrication process.

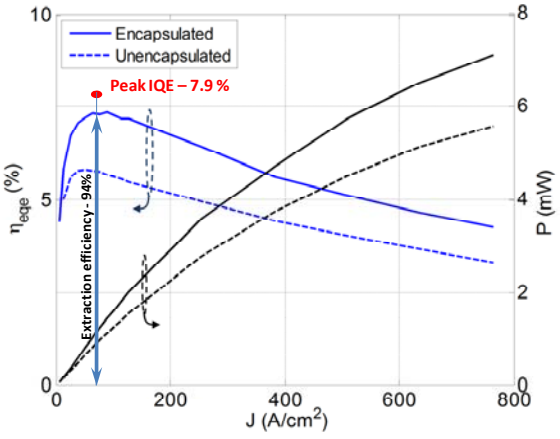

External quantum efficiency of embedded PhC LEDs

7. Achievements

Milestones		Achievements
Task 1		
Achieve uniform, reproducible sub-micron mask patterning and etching over areas of at least 1x1 cm^2		• This milestone is achieved by optimizing a nanoimprint lithography technique.
Optimize dry etching methods to achieve PhC depths of at least 300 nm.		• Dry etching methods to achieve PhC depth larger than 300 nm have been developed both for ICP and RIE etching systems and by using Cl_2/N_2 based chemistry.
Demonstrate photonic crystal light extraction efficiency enhancement by a factor of 2 with respect to planar samples, in photoluminescence (PL).		• The use of photoluminescence measurements to quantify the change of the light extraction is found to be unreliable. In fact, any change of the wafer structure leads to an unknown modification of the coupling of the excitation source (laser) to the active region. Therefore the light extraction enhancement is very difficult to estimate and generally remains unknown.
Task 2		
Develop low-index epitaxial layers that are crack-free over a typical LED area (300 x 300 µm), consisting of at least 500 nm of AlGaN with 12% of Al (or another optically equivalent layer).		• A technique to overgrow cracks has been demonstrated during the growth of high Al content AlGaN layers in PA-MBE. The latter allows achieving uncracked templates containing 700 nm thick $Al_{0.7}Ga_{0.3}N$ layers. • We have equally demonstrated uncracked LED AlGaN layers grown by MOCVD with Al composition up to 15% and layer thickness up to 500 nm. • We have experimentally established the cracking limit for various AlGaN thicknesses and compositions. Based on these results we have calculated that an optimal uncracked structure should contain a 120 nm thick AlGaN layer with Al composition of 21%.

Demonstrate the beneficial role of the low-index layer by evidencing that it contributes to 30% of the light extracted by the PC, in PL experiments.		• The use of photoluminesnce measurements to quantify the change of the light extraction is found to be unreliable. Besides, results of electrically pumped LEDs where available soon after the fabrication of first LED wafers.
Task 3		
Demonstrate PhC-LEDs with total resistivity within 20% of the resistivity of standard LEDs.		• This milestone is achieved for devices where the *n*-type (bottom) contact is placed above the AlGaN layer. • In addition, ITO contacts and PhC etching procedure have been developed for efficient current spreading underneath the p-contact.
Demonstrate the beneficial role of the low-index layer by evidencing that it contributes to 30% of the light extracted by the PhC, in electroluminescence experiments.		• We have demonstrated an increase of 17% of the total extracted light to be due to the introduction of AlGaN index guiding layer. • We have also demonstrated an increase of over 75% for the vertically outcoupled light. The latter is achieved after careful optimization of the PhC parameters.
Task 4		
Demonstrate reproducible lift-off and cavity thinning techniques for sample size of 25 mm^2 or greater.		• We have demonstrated reproducible Au-Au bonding procedure and lift-off process. Its yield is over 80% for a 1x1 cm^2 sample. • Precise control of the thinning procedure is achieved by introducing a thin AlGaN etch stopping layer and developing a selective etching process for N-face GaN and AlGaN.

Fabricate electrically injected lifted-off PhC-LEDs with an output power 3x of a conventional LED.		• We have demonstrated that an introduction of a PhC to a standard MCLEDs leads to an increase of 2.5 times of the total output power. This effect comes in addition to already increased direct light out-coupling due to the microcavity effect. The simulated values show that for our structures 30% of the light should be directly extracted compared to only 6% (per side) for the conventional LEDs. However, a direct experimental comparison between our devices and conventional LED is difficult because of the large differences in geometry and processing steps.
Task 5		
Achieve GaN coalescence and planarization over a 2D patterned mask within 500 nm of overgrowth, over at least 60 nm of SiO_2.		• Coalescence of thin GaN layer is achieved for three different patterned structures (SiO_2 pattern, SiO_2 + air-gap pattern, and air-gap pattern). The thinnest coalescence layer of 70 nm is obtained for the air-gap pattern. The latter also offers the best performance as PhC due to the highest refractive index contrast. • A procedure to effectively control the thickness and filling factor of the embedded air-gap PhC is demonstrated. Thicknesses up to 300 nm have been achieved.
Demonstrate electrically injected LEO PhC LED where at least 50% of the guided light is extracted over a distance smaller than 500 μm.		• We have demonstrated electrically injected LEDs with embedded air-gap PhC gratings. • We have developed a reliable technique to directly assess the extraction length of the guided modes. • We have demonstrated that all guided modes are extracted for distances ranging 64 – 90 μm.

Task 6		
Optimize the best-performing design of the above three PhC-LED approaches, such that the output power is three times that of a good conventional LED (defined as an LED with 70% of the output power of the best-achieved conventional LED at UCSB).		• We consider that embedded air-gap PhC LEDs are the best performing devices. • For embedded air-gap PhC LEDs we have demonstrated a light extraction efficiency of up to 94%. In addition, we have demonstrated that the regrowth procedure does not modify the LED template internal quantum efficiency and devices with electrical performances similar to standard LEDs are consistently obtained. • In addition, we have significantly improved both the output power and electrical characteristics of our PhC MC LEDs. The latter are considered to have large potential for industrialization due to the small differences to some currently used LED technologies. Note: Direct comparison of the output powers of our LEDs to other sources is inadequate as an optimized growth process for high quality *c*-plane LEDs is currently unavailable at UCSB.

8. Summary of the project activities

In this section we present a resume of the development details and performances for all three approaches that have been undertaken – AlGaN index guiding layer light emitting diodes (AlGaN IGL PhC-LEDs), micro-cavity photonic crystal light emitting diodes (MC PhC-LEDs), and embedded photonic crystal light emitting diodes (embedded PhC-LEDs). The presented data correspond to the state by the end of the present project. The development of AlGaN IGL PhC LEDs has been limited in the framework of Task 3 during the second year of the project. Meanwhile, the optimization of both MC PhC LEDs and embedded PhC LEDs has been pursued during the final year (Task 6) due to the substantially greater potential of the two structures. In conclusion, an analysis of the obtained performances is presented.

Large-area submicron patterning of photonic crystals (Task 1)

(1) E-beam lithography

Electron beam lithography provides the means to explore various photonic crystal (PhC) structures, allowing periodic nanometer scale air hole patterns as well as non-periodic macroscopic layouts. The optimal light extraction requires PhC with period (the spacing between two centers nearest holes - **a**) in the range of 200 nm. The radius (**r**) of the hole is limited by the e-beam setup to 60 nm. Thus, our optimal PhC patterns that have typical hole filing factor **r/a = 0.3** are easily achievable. Currently, 300 × 300 μm^2 sized PhC patterns with a lattice constant of 180 nm and larger can be easily obtained with the developed process. Obtaining, patterns with larger sizes is generally limited by time and cost. Example of a PhC fabricated by the means of e-beam lithography is presented in Figure 1. The deepest PhC structure presented is more than ~400 nm deep.

(2) Holographic lithography

Holographic lithography is a technique that allows producing nanometer scale PhC patterns over a large area by the means of laser beam interference. It is characterized by a relatively low cost and high yield. The method can be used to pattern either directly the GaN template or to produce imprint masks for Nanoimprint lithography. Significant amount of research has been carried out

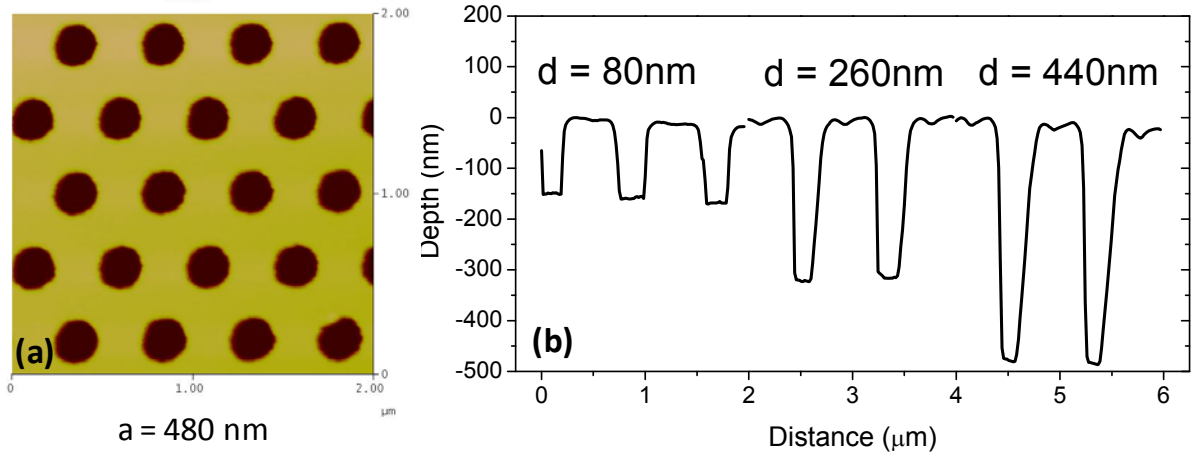

Figure 1 (a) AFM image of PhC pattern made by the means of e-beam lithography; (b) Depth profile of various PhC patterns. Note that ~10 nm thick SiO_2 layer is still present on top of the GaN PhC.

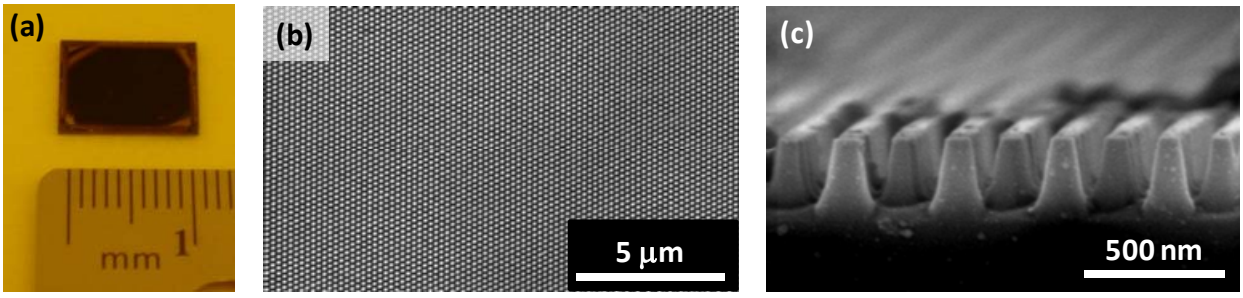

Figure 2 (a) Image of a 1x1 cm^2 Si nanoimprint mask; SEM image of a segment of the Si nanoimprint mask illustrating the lack of defects; (c) Close-up cross-section view of a Si nanoimprint mask.

to establish a reliable process, applicable for PhC lattices of 210 nm or greater. The latter is limited by the wavelength of the used HeCd laser (emission wavelength 325 nm). The method has been optimized for the preparation of large area Si hard masks for nano-imprint lithography. An example of such mask is presented in Figure 2. Its period is 220 nm and the actual mask size allows nanoimpritng PhC patterns as large as 1 cm^2. Producing larger masks by holographic lithography is also possible but would require modifications of our setup.

(3) Nano-imprint lithography

Supported by the progress in holographic lithography, we have produced nanoimprint masks made of Si. We have optimized the imprint conditions (pressure, temperature and process time) in order to obtain repeatable process with high yield. An example of PhC nanoimprint patterning with period of 235 nm and hole dept of 294 nm is presented in Figure 3. As a first step of the process the pattern from the Si mask (Figure 3a) has been transferred to the imprint resist (Figure 3b,c). The latter is then used as mask for a dry etching the PhC pattern in the GaN template. Optional SiO_2 hard mask can be used here as an intermediate step if one needs deeper PhC and/or more vertical hole sidewalls. As seen in Figure 3 high quality short period PhC patterns can be easily achieved with nanoimprint lithography where the pattern size is only limited by the mask size. In addition hole depth of 300 nm can be easily achieved.

(4) Dry etching methods

Our research on dry etching methods has been carried out with principal two objectives. The first objective is to guarantee successful pattern transfer from the initial resist layer to the hard etch mask layers and then to the final GaN template with high integrity. The second objective is to investigate the etch process for the N-face GaN substrate, important for the laser lift-off (LLO) LED processing that is described in Task 4 of this project.

Regarding the first objective, we have established reliable process recipes for both reactive ion etching (RIE) and inductively coupled plasma (ICP) etching systems. These processes allow the fabrication of PhCs with lattice constants of 180 nm or larger and depth profiles of 300 nm (Figure 3d). Unfortunately, we were unable to obtain conclusive information for possible degradation of the internal quantum efficiency of the quantum well (QW) active region. Successful etch process for the N-face GaN was also developed. More details on some important considerations regarding this objective will be given in the progress report of Task 4 below.

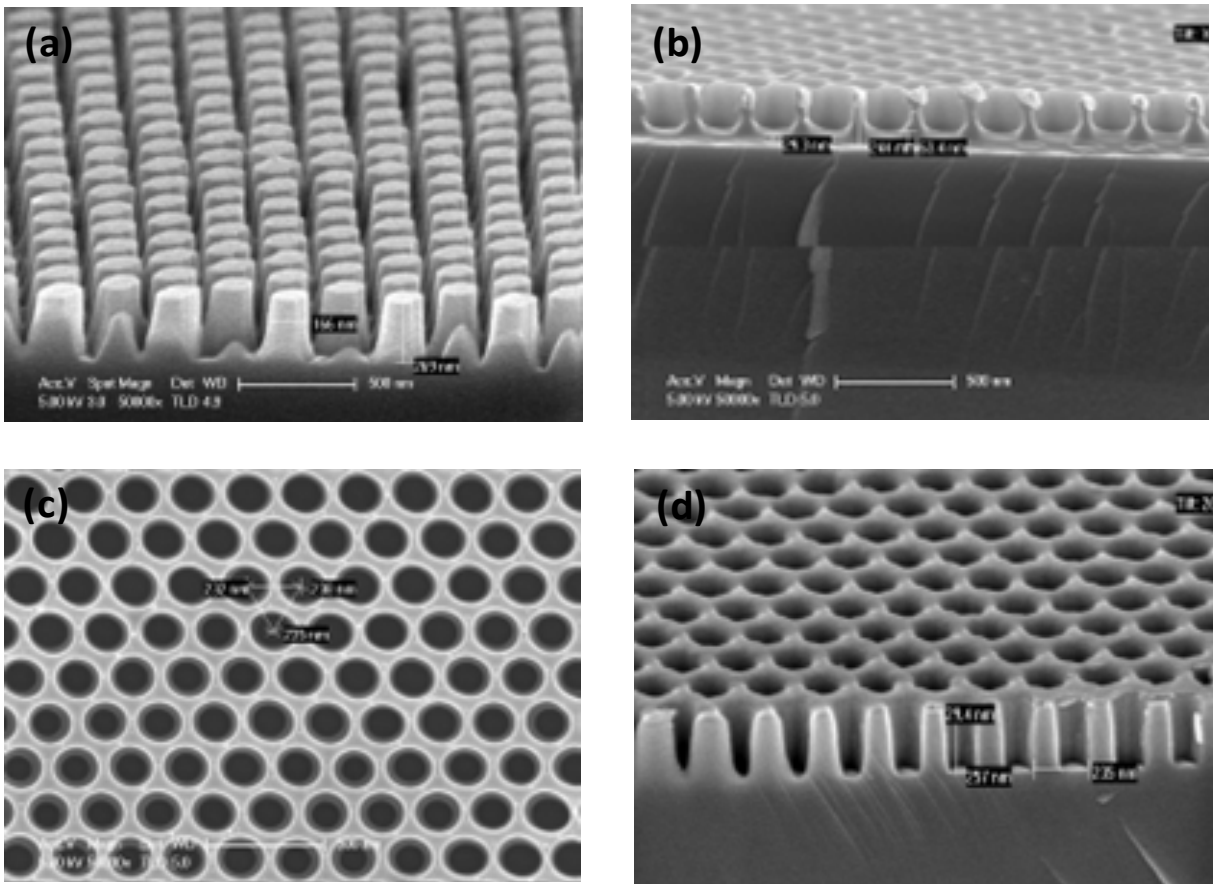

Figure 3 Scanning electron microscope (SEM) images. (a) Si nanoimprint mask obtained by holographic lithography and dry etching (b) Top view and (c) side view of PhC patterns formed in a resist layer by Nanoimprint lithography. (d) The PhC pattern is transferred to the dielectric etch mask and to GaN by a dry etching process.

(5) Extraction enhancement in photoluminescence measurements

Photoluminescence measurements have been performed on both unprocessed templates and such patterned with PhCs. As expected, the PL spectra reveal the appearance of some additional feature (mode structure) for the samples with surface PhC in comparison to those without. Unfortunately, no rigorous method to compare the intensities of the emitted light can be developed. Furthermore, we believe that such method cannot allow effectively optimizing the LED and PhC structures and thus our efforts has been directed elsewhere.

In conclusion, we have explored three different techniques for etching PhC in GaN templates. All of them allow obtaining high quality PhC patterns with lattice period as low as 200 nm and etch profile as dept as 300 nm. However, the techniques can be categorized for different task according to their cost, time consumption and versatility. The e-beam lithography is found the optimal tool during the PhC pattern optimization due to its higher versatility compared to the other two. On the other hand, it's a costly and time consuming process which would seriously limit its use in large scale LED production. The holography lithography is able produce cheap very large size high quality PhC patterns. However, it is a tricky technique that requires serious preparation and controlled environment. Thus, we find this method to be the best for production of large Si masks for nanoimprint lithography. The latter is found to be the most reliable and fast to produce PhC

patterns on GaN templates. Furthermore, it has the benefit to be very cheap and robust. During this project we have developed nanoimprint process only for patterning GaN LED templates. Nevertheless, we believe that it can be easily adapted to pattern a PhC on top of a LED mesa.

Design, fabrication, characterization, and optimization of AlGaN epitaxial layers (Task 2)

(1) Crack-free high-Al content AlGaN

To achieve higher extraction efficiencies of AlGaN-based PC LEDs, high Al content and high thickness AlGaN layers with surfaces free of cracks are desired. Due to the lattice mismatch, high Al content AlGaN layers grown on GaN are prone to crack even after a few nanometers of growth. We have first investigated the cracking mechanism of AlGaN and examined the theoretical limitation for the thickness of uncracked AlGaN grown on GaN for various Al compositions. The growth studies have been carried out using a plasma-assisted molecular beam epitaxy (PAMBE). The test samples are then examined by atomic force microscopy (AFM). The experimental values are compared in Figure 4. The AFM images showing the typical topography of three $Al_{0.31}Ga_{0.69}N$ layers with different thicknesses are also given to exemplify the different crack morphology. The experimental findings match well with Griffith's criterion (solid lines in Figure 4) for brittle fracture as discussed by Hutchinson *et al.*, (Advanced in Applied Mechanics (Academic, San Diego, 1992), Vol. 29, pp. 63-191). Here, one can conclude that with standard growth techniques achieving an AlGaN layer with parameters for optimal light extraction is extremely difficult.

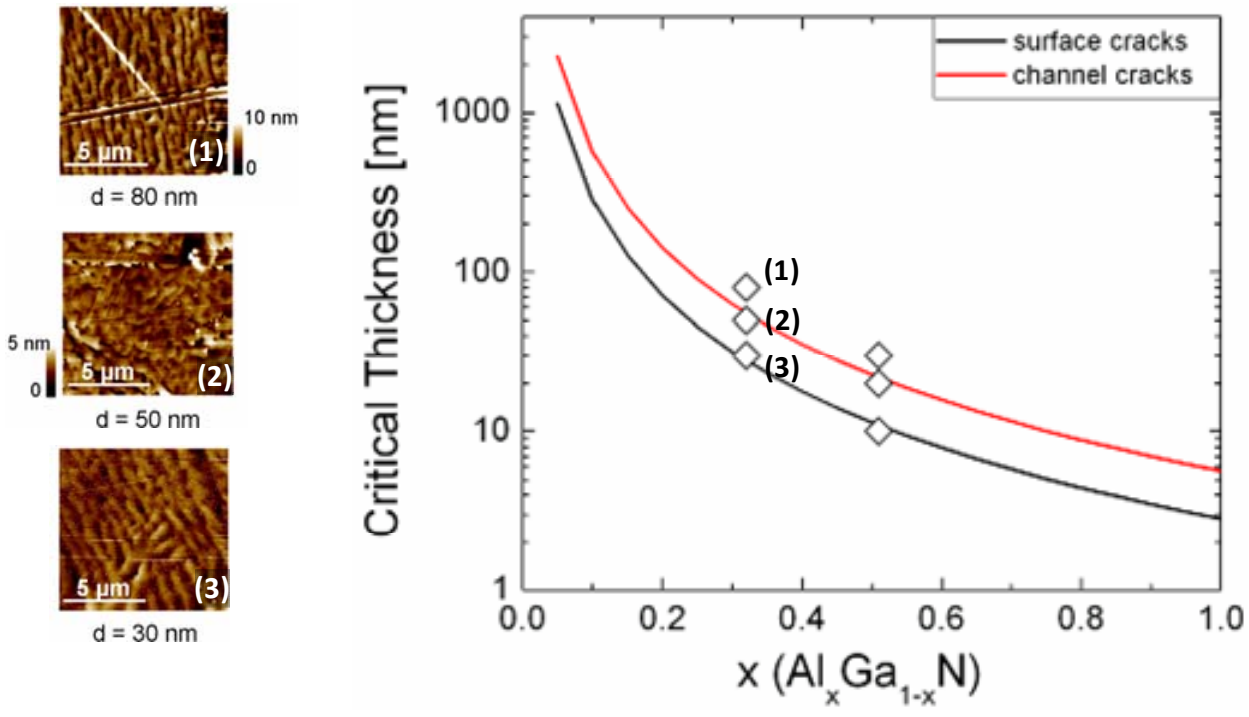

Figure 4 The critical thickness for AlGaN film grown on GaN. The 3 images on the left side show the AFM topography of $Al_{0.31}Ga_{0.69}N$ surfaces at the different film thickness indicated with each figure.

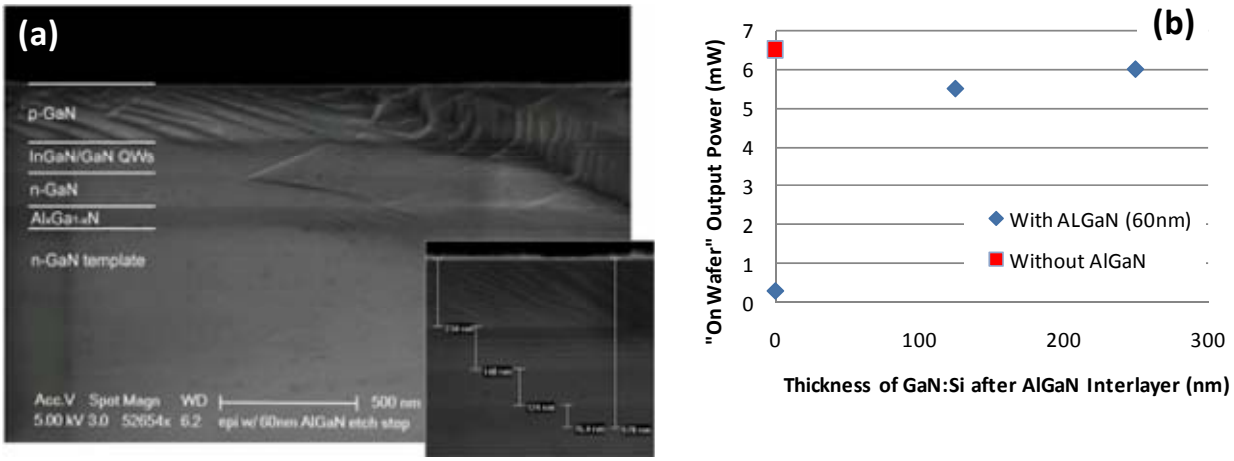

Figure 5 (a) The SEM image of an LED wafer with the AlGaN interlayer; (b) On-wafer output power of LED wafers with AlGaN interlayers at 20 mA.

(2) Growth of 700 nm thick $Al_{0.75}Ga_{0.25}N$ layer on GaN:

An interesting approach to overcome the barrier of critical thickness for AlGaN on GaN is to bury the cracks by growing thicker AlGaN layers. Growth conditions promoting higher lateral diffusion and growth are necessary. Thus, significant research effort was undertaken to explore the growth kinetics for achieving thick AlGaN layers.

At current stage we are able to grow a 700 nm thick AlGaN layer with Al composition of 75% on a Ga-face GaN template. The growth conditions used in the PAMBE system are set to promote high adatom surface mobility, namely Ga rich droplet regime and relatively high substrate temperature (720^{o}C). Subsequent to the AlGaN growth, a 300 nm thick GaN cap layer can be grown under the same conditions to allow surface studies on a structure close enough to a real LED template. The surface quality and the crack network of such samples are studied during growth by reflection high energy electron diffraction and after growth by scanning electron microscopy and atomic force microscopy. Both AlGaN and GaN terminating surface were relatively smooth. The mean surface roughness for the GaN top surface is typically under 2 nm over an area of 20x20 μm^2 area. Only a few cracks were left on the surface that could be easily avoided when etching down the LED mesas. Samples exhibit clear evidence that the cracks were partially overgrown by high lateral growth along their facets. Finally, along with the material overgrowth available MOCVD, the current approach provides a viable mean to fabricate thick AlGaN light confining layers that could be used to maximize the extraction from the PhC LEDs.

(3) High quality AlGaN by MOCVD

The studies performed in PAMBE allowed gaining essential knowledge about the critical parameters for growth of thick AlGaN layers (most relevant parameter being the layer thickness). However, commercial nitride-based LEDs are grown by MOCVD. Thus we need to develop a robust AlGaN deposition process for atmospheric pressure MOCVD. A particular issue is to find a set of growth condition that does not suffer from pre-reaction effects when tri-methyl-aluminum (TMAl) and NH_3 are introduced in the reaction chamber. This required the characterization of the prereaction mechanisms in correlation with film quality and reproducibility. Under the growth condition optimized for standard *c*-plane LEDs, pre-reaction effects are observed for Al

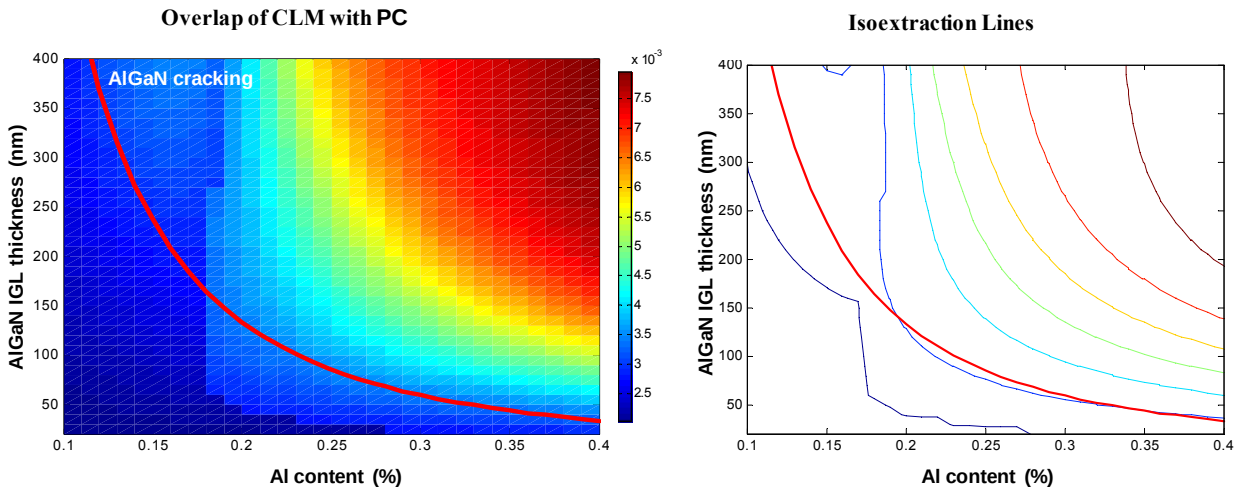

Figure 6 Overlap of cap layer mode with photonic crystal as a function of AlGaN thickness and Al composition.

compositions greater than 14% and TMAl flow rate larger than 1.5 sccm. With further increase in TMAl flow rate, the achieved Al composition in the final structure is actually decreased. Much effort has been made to prevent this parasitic pre-reaction effect and thus to control the Al composition and AlGaN quality.

Eventually, high quality AlGaN layers were achieved by modification of deposition conditions (essentially growth temperature 1100°C, N_2 carrier gas) which allowed the mitigation of prereactions of TMAl and NH_3. The properties of these AlGaN layers were evaluated with optical microscopy, XRD, and AFM analysis. Growth rates were quantified for various AlGaN compositions through the characterization of AlGaN/GaN heterostructures. Under the optimized growth condition, the Al composition could be accurately controlled by the TMAl flow rate without suffering from prereaction effects for Al compositions as high as 35%. Finally, LED templates containing crack-free $Al_{0.15}Ga_{0.85}N$ light confining layers with a thickness ranging between 60 nm ~ 500 nm could be easily achieved in the optimized growth conditions (Figure 5). These structures are tested to verify their power output performance as compared to LEDs without an AlGaN interlayer. Initial power measurements showed a drastic degradation in performance with the insertion of an AlGaN layer prior to the deposition of a quantum well active region. However, this issue was readily resolved by the insertion of a thin, high quality, silicon doped GaN layer before deposition of the active region. We can achieve a comparable output power as shown in Figure 5b.

(4) Design of the AlGaN light confining layer for increased PhC light extraction

In some previous simulations concerning the effect of the AlGaN light confining layer, it have been shown that the confinement of the cap layer mode increases with both the Al composition and the confining layer thickness. However, as we have discussed earlier, the AlGaN layer cracks when it is grown above a certain critical thickness that depends on the Al content. Thus we have performed simulations optimizing the AlGaN confining layer parameters along the AlGaN cracking limit (Figure 6). The goal is to obtain a structure with the best PhC extraction, but with no degradation of the quantum efficiency caused by cracks. As the efficiency of the photonic crystal extraction is proportional to the overlap of electromagnetic modes with the photonic crystal layer the latter is suitable as optimizing parameter. Thus, the variation of the overlap of the

cap layer mode (CLM) with the Photonic crystal as a function of the Al content in the AlGaN layer and the AlGaN thickness is presented in Figure 6. One can see that although a high Al content or a thick AlGaN layer would result in a high overlap of the CLM with the photonic crystal, it would also result in a cracked AlGaN layer (region above the red line in Figure 6). For a structure without cracks, one can calculate the structure that yields the maximum overlap with the photonic crystal along the AlGaN cracking line. The optimal uncracked structure should have the following parameters:

- Optimal Al content: 21%
- AlGaN thickness: 120 nm
- Optimal quantum well position: 193 nm within the GaN Cap Layer (60% relative position);
- Optimal GaN cap layer thickness 320 nm (minimal thickness to support *pn* junction).

This structure yields an overlap of the CLM mode with the photonic crystal of 0.38%. The optimized structure compared with the previous AlGaN confined LED (non optimized) would have a 3 times higher overlap of the CLM with the PhC added to and higher quantum efficiency (no cracking).

(5) AlGaN etch stop layer for LLO microcavity LEDs

Stepping aside from the direct goals of the current task we should comment on another use of the developed high quality AlGaN layer. One of major challenges for reliable processing of LLO PhC LEDs is the process of thinning down the microcavity. When the LLO process is carried out for a conventional *c*-plane LED wafer, the resulting GaN surface has the opposite crystalline polarity. The so called N-face GaN has a very rough surface morphology due to LLO as well as the inherent film quality grown on the sapphire substrate.

To fabricate microcavity LEDs out of LLO mesas, repeated chemical mechanical polishing and dry etching are required. However, this processing scheme suffers from low yield and poor reproducibility. Furthermore, the high precision required to keep submicron cavity thickness uniform is unreasonable for a reliable and reproducible process. Here, possible solution would be to introduce etch stop layer (layer with very low etch rate in the normal etching conditions of GaN). In general, such etch selectivity has been known among various semiconductor heterostructures, for example, Ga-face GaN and Ga-face AlGaN. Being sufficiently high, this can allow an accurate and reliable thinning process. Indeed, a selectivity of ~1:10 for $Al_{0.5}Ga_{0.5}N$:GaN was found for a SF_6-based ICP etching process. Our MBE study of growth kinetics and critical thicknesses has allowed the growth of high-quality test samples for the characterization of this etch selectivity, which is then confirmed in LLO microcavity LED processing with the MOCVD wafers (see report on task 4).

In conclusion to Task 2, we have explored the processes that govern the growth of thick AlGaN layer with high Al amount necessary for introducing light confining layers in PhC LEDs. We have verified the limit thickness for uncracked layers and we have demonstrated a solution to evade this limitation by burring the cracks in surface diffusion enhanced PAMBE growth. For the more production adapted MOCVD system we have chosen to work with layers under the crack limit. The growth of such layers has been optimized and achieving on-wafer power comparable to that for a standard UCSB LED template. The necessary AlGaN layer thickness and composition have been optimized to obtain maximal CLM overlap with the photonic crystal without inducing cracks in the LED template. For the optimal parameters one can expect a three time increase of the extraction efficiency of the CLM compared to similar previous structures. Actual values of the obtained extraction efficiency for processed samples will be discussed in the discussion of Task 3.

Design, fabrication, characterization, and optimization of AlGaN PhC-LEDs (Task 3)

(1) AlGaN PhC-LED test structure for electrical injection

The effect of the vertical light confinement in PhC LEDs is studied by comparing two types of LED structures; a new structure with the AlGaN index guiding layer (IGL) and a conventional one without the IGL. Both templates are grown by metal-organic chemical vapor deposition (MOCVD) on double-side polished sapphire substrates. The test structures consists of 4 μm thick standard *n*-GaN template layer followed by: a 100 nm *n*-InGaN, a 500 nm – 600 nm *n*-$Al_{0.12}Ga_{0.88}N$ (Δn~0.06) IGL, 100 nm n-GaN contact layer, InGaN/GaN multi-quantum well region, a 20 nm $Al_{0.20}Ga_{0.80}N$ electron blocking layer, and finally a 280 nm *p*-GaN layer. LEDs mesas with 800 μm x 800 μm in plane dimensions were formed on the wafer. We employed either ITO or Ni/Au for the *p*-contact that was placed in the center of each LED with a diameter of 100 μm. Triangular lattice PhCs with lattice constants of 185 nm, 200 nm, 215 nm and 230 nm and air fill factor of 30% were formed by electron beam lithography and reactive ion etching using a SiO_2 mask. The depth of the PhCs is between 150 nm - 250 nm, above the active region. The PhC pattern was placed around the *p*-contact with the extent of 400 μm x 400 μm (ITO LEDs) or 500 μm x 500 μm (Ni/Au LEDs) as shown in Figure 7a.

In our experiments, direct comparisons are made only for nearby LEDs on the same wafer in order to eliminate the effects of the material variation. For all samples the electrical characteristics of non-PhC LEDs were identical to PhC LEDs, indicating that the PhC patterning did not have any detrimental effects as seen in Figure 7b. In the case of AlGaN IGL LEDs, we observed a degradation of the electrical performance when our contact was placed on the AlGaN IGL. But these effects can be avoided by having the *n*-contact on the *n*-GaN layer that is above the AlGaN IGL. Furthermore, we found no limitations in *n*-GaN current spreading as a result of the AlGaN IGL. Finally, the PhC-LED with the AlGaN IGL (Figure 7c) demonstrated enhanced brightness as compared to the non-PhC-LED (Figure 7d).

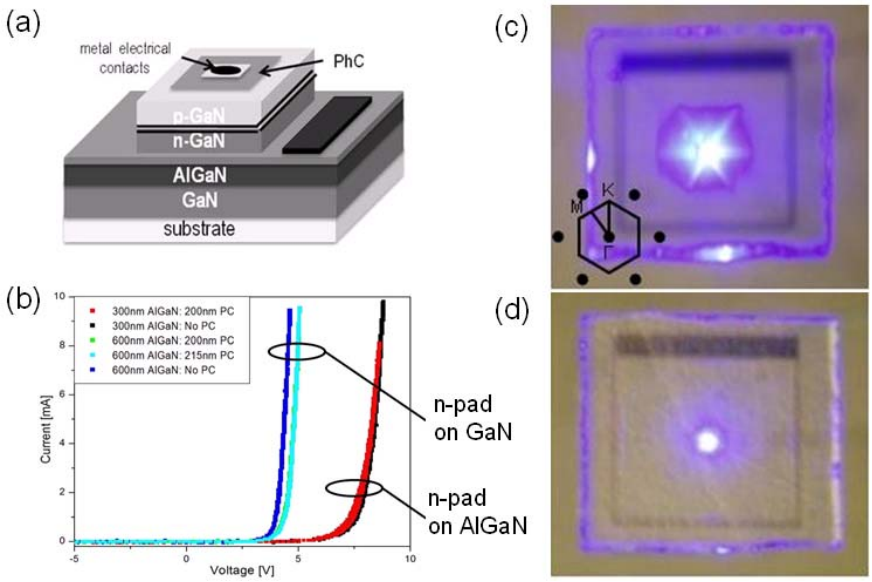

Figure 7 AlGaN PhC LED: (a) A schematic diagram of a device structure (b) The current vs. voltage data for PhC and non-PhC LEDs. (c) The picture of AlGaN PhC LED, showing the increased diffraction from the PhC especially along the ΓM directions of the triangular lattice with 200 nm periodicity. Inset: the PhC orientation in reciprocal space. (d) The picture of non-PhC LED.

(2) The effects of the AlGaN IGL on the performance of PhC-LEDs

At first stage we compare the total output powers of PhC-LEDs with and without the AlGaN IGL in integrating sphere experiments. As the LED internal quantum efficiency varies from one wafer to another we can compare only nearby LEDs on the same wafer which imposes to compare the increase of extraction efficiency of PhC LED over nearby LED without patterned PhC rather than the direct power outputs. For devices with PhC periodicity of 200 nm, these overall enhancements were 2.1 times for the sample with the AlGaN IGN and 1.7 times for that without the IGL. This means that the AlGaN IGL has enabled a 17% increase in the total output power. However, this should be considered as a conservative estimate as the integrating sphere experiment take into account not only the top side emission (the one affected by the PhC) but also side emissions that are not affected by the AlGaN IGL. In fact, the introduction of IGL leads to redistribution of the intensity emission pattern. Indeed, the near vertical output power for a 200 nm PhC LED, measured with a back side photodetector (NA ~ 0.85), is increased by 2.9 times for a structure including an AlGaN IGL and only 2.1 times for that without IGL. That corresponds to a 40% increase in the optical output when an AlGaN IGL is present. This enhancement of the vertical emitted light is related to the appearance of the cap layer mode. To evidence this we can compare the angular resolved intensity profile for given wavelength (Figure 8). It is marked feature that increasing the AlGaN layer thickness (similar effect is also expected for a reduction of the AlGaN refractive index) leads to increase in the relative intensity of the CLM compared to all other (high order) modes. Concentrating the light in a single guided mode is an interesting feature that can be easily exploited. Indeed, by tuning up the lattice period we can achieve near vertical extraction of the CLM when the conditions for second order diffraction are satisfied. Thus, we have processed to optimization of the PhC lattice parameters to study and evidence such enhancement of the light directionality.

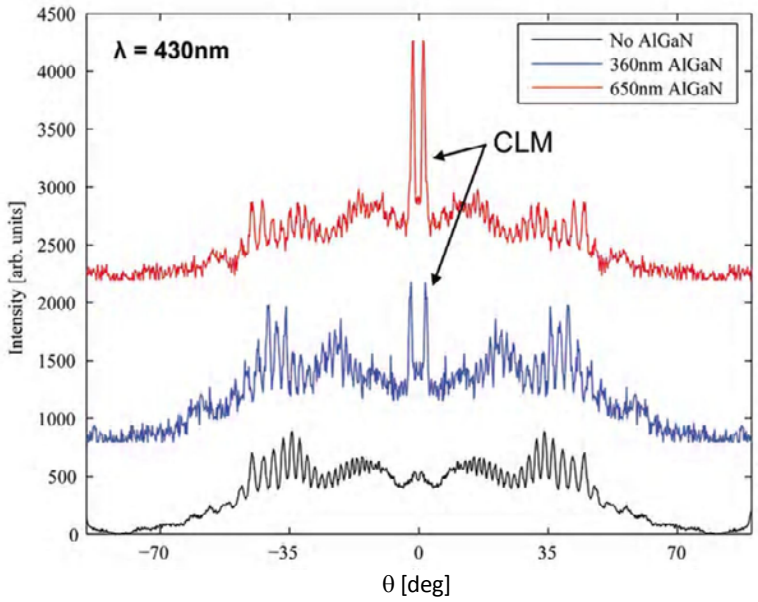

Figure 8 Angular-resolved intensity profile for the electroluminescence at 430 nm measured along the ΓM direction.

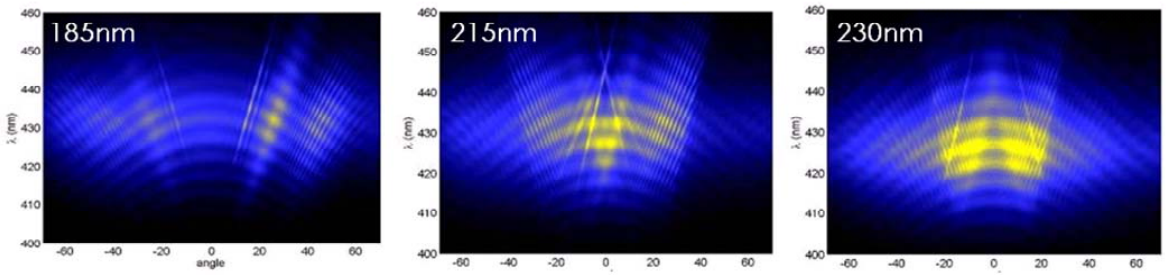

Figure 9 Angle-resolved electroluminescence of the AlGaN PhC-LEDs with different periodicities.

(3) The effects of variation in lattice period on the directionality

To reveal the effects of PhC lattice on the vertical emission, we have investigated the far-field emission of series of test devices having the same overall geometry (two types of contacts were tested) but varying the PhC lattice period $a \in \{185\ nm, 200\ nm, 215\ nm, 230\ nm\}$. One can see the effect of the lattice parameter change on the far field emission pattern in Figure 9. Those angular resolved electroluminescence (EL) are measured in the ΓM direction of the PhCs for LEDs with various PhC lattice period. The sharp emission lines arising from PhC diffraction are visible along with background emission, weakly modulated by Fabry-Pérot interference. Each of these lines corresponds to a guided mode that has been diffracted above the light line by the PhC. The more intense line in both the angular emission and the band structure corresponds to the cap layer mode (CLM), the mode confined by the AlGaN IGL. It can be easily seen that for the case of $a/\lambda \sim 0.5$ (where a is the lattice period of the PhC and λ is the peak wavelength) the CLM is extracted in a light cone of $\pm 20°$ from the vertical direction. This feature has serious impact on the total directionality of our AlGaN PhC LEDs. The far field emission pattern (integrated over the whole spectrum emitted by the QWs) as a function of the PhC lattice period is presented in Figure 10 for two different sets of samples with different *p*-contacts. The enhancement of the vertical emission is stronger for PhC with periodicity of 200 and 215 nm for the LEDs emitting at 405 and 430 nm, respectively. To quantify this enhancement of the vertically emitted light we measured the LEDs output power with a photodetector in a geometry that allowed a collection angle of $\pm 20°$ from normal direction. The highest increase of 3.5 times in the vertically outcoupled power is observed for the AlGaN PhC LEDs with the PhC lattice constant of 215 nm

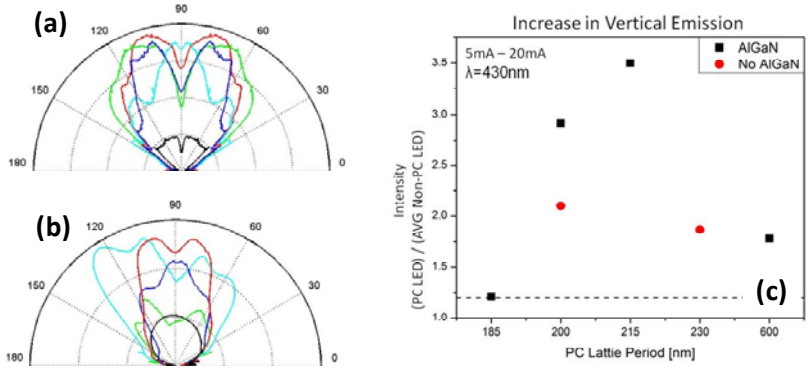

Figure 10 Directional emission in the far field (a) AlGaN Ph-LED with the ITO p-contact and the peak wavelength of 430 nm. (b) AlGaN Ph-LED with the Ni/Au p-contact and the peak wavelength of 405 nm. (c) The observed enhancement of light emission to the vertical direction.

and the peak wavelength of 430 nm. Note that this enhancement was achieved without the use of a backside mirror. For completeness, we can compare the PhC related enhancements in vertical output power for both PhC LEDs with and without IGL. While for the latter the improvement remains generally independent on the PhC lattice period the former devices exhibit a peak improvement when the CLM is extracted vertically (a/λ = 0.485). In that case, the output power is 3.5 times in the case of a LED with AlGaN IGL and only 2.26 times for the case without. That corresponds to an improvement of the vertically outcoupled light of over 75% just by adding an AlGaN IGL. This enhancement in the vertical emission is quite large, even with the relatively small index contrast of the AlGaN and defines the niche advantage of the AlGaN PhC LEDs for achieving high brightness LEDs.

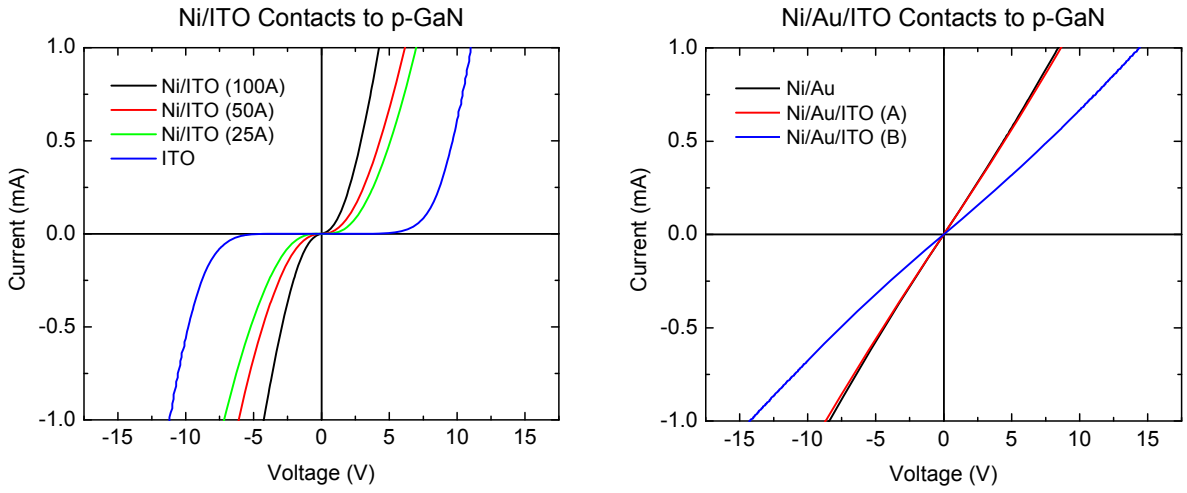

Figure 11 Electrical properties of different ITO based *p*-contacts

(4) ITO contacts for efficient current spreading

One of the disadvantages of the geometry studied above is the fact that the light emission actually occurs in a small area under the p-contact. To overcome this problem we have developed transparent ITO contact that covers the entire LED mesa. The material for the transparent current spreading contact is a sputtered ITO (e-beam evaporation was also considered but it did not give satisfying results). The deposition and post annealing conditions were carefully optimized to achieve high transparency material while maintaining low resistivity. The optimized material parameters are: $\rho = 2.5\,x\,10^{-4}\Omega\,cm$, $R_{sh} = 9.5\,\Omega/\blacksquare$, T = 99% at 480 nm and an absorption coefficient $\alpha = 500\ \mathrm{cm}^{-1}$ at 450nm. We have studied several different *p*-GaN contact stacks. The contact resistance of ITO to *p*-GaN has been measured to be quite elevated for our layers. However, the inclusion of a thin (less than 30 Å) Ni interlayer dramatically improves the contact resistance (Figure 11). For achieving a low resistance an additional thin Au layer has been introduced. After an optimized annealing process the contact resistance was reduced to $9.0 \times 10^{-3}\Omega\,cm^2$, which is only 1.5 times higher than a standard Ni/Au contact. Finally, a process for RIE etching of ITO has been established using a $CH_4/H_2/Ar$ based chemistry. That allowed etching down a PhC inside the ITO current spreading layer and fabricating an AlGaN PhC LEDs with current spreading layer. The measured devices with PhC exhibit a 1.3 times increase of the vertically emitted light (NA = 0.45) over a non-PhC LED with the same current spreading layer.

In summary for Task 3, we have demonstrated optimized PhC LED design that incorporates an AlGaN IGL for increased light extraction. A direct comparison of the output power measured in an integrating sphere shows only about 20% increased that can be attributed to the incorporation of the AlGaN IGL. However, the incorporation of the IGL allows a noteworthy increase in the vertical emission within a limited polar angle. The improvement measured in vertically outcoupled power is over a 50% greater that of a standard PhC LED. The latter is achieved by modifying the vertical structure and tailoring the PhC lattice constant without using any metal reflector. That features defines the niche benefits of using IGL inside a PhC LEDs, namely, the possibility to precisely tailor the LED far field emission pattern and achieve high brightness LEDs.

Design, fabrication, characterization, and optimization of lifted-off LEDs on metal substrate (Tasks 4 and 6)

(1) 3D simulations for advanced device design

Many parameters should be considered for the design of PhC MC LEDs. Basically, in these devices there are two mechanisms that lead to increased light extraction. First the microcavity effect helps to outcouple significant part of the QW emission into a directly emitted light. The remainder (guided modes) is then extracted by the photonic crystal. Several parameters have to be considered to maximize the extraction efficiency. The latter is first done by the means of rigorous 3D simulation based on a scattering matrix algorithm.

First, we consider the microcavity effect. The direct light extraction enhancement is governed by two parameters: the total cavity thickness and the QW positions. Their effect on the direct light outcoupling has been simulated in a scattering matrix formalism including a quantum well emission model. The results in Figure 12a provide valuable guidance. First, the higher extraction is achieved for the thinnest microcavity. Unfortunately, this is not achievable because the minimal thickness to support a good *p-n* junction is about 500 nm. That condition plus some processing difficulties usually forces us to work with typical microcavity thicknesses in the range of 0.5 to 1 μm. In this regime, one can expect that about 30% of the emitted light will be directly emitted to

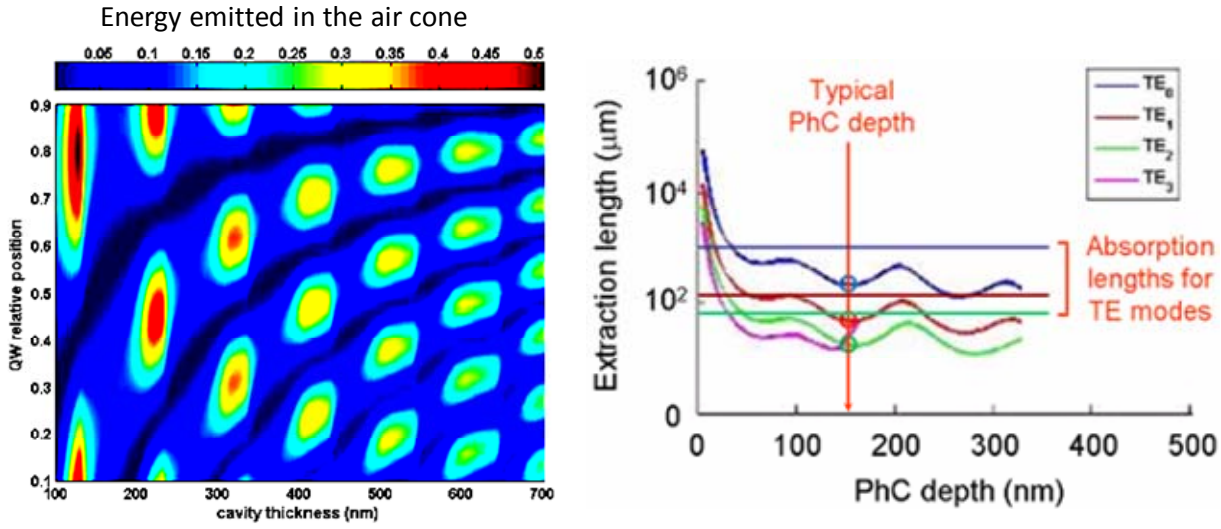

Figure 12 (a) Simulation of the directly outcoupled light in MC LED as a function of the cavity thickness and the active region relative position; (b) Simulated extraction length for the first few guided modes as a function of the PhC depth.

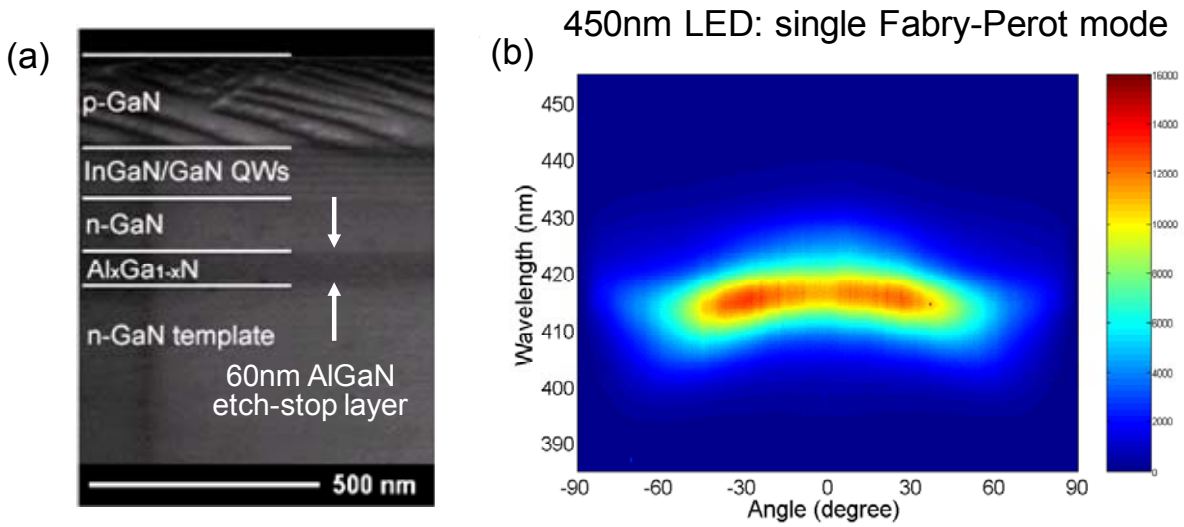

Figure 13 (a) Cross-sectional SEM of as-grown wafer with AlGaN etch-stop layer for selective-etch cavity thinning process. (b) Angle-resolved EL spectrum for 450 nm-thick thin-film microcavity LED.

air. The latter, however, is only available when the QW position is well optimized which is not often straightforward. However, the former condition becomes less relevant when adding the effect of the PhC on the overall light extraction. Indeed, the light that is not directly emitted in air due the cavity effect remains in the LED as guided modes that are outcoupled by the PhC. Here, important parameter is the modal extraction length. The latter has to be shorter that the device size and more importantly than the modal absorption length (for detailed discussion see Appendix 2). While the former is usually easily achievable, the latter can be rather difficult. In fact the light extraction for the guided modes is in competition with the metal absorption due to the *p*-side metallic mirror. One of the least evident but very important parameters that can be tweaked to benefit the light extraction over the absorption is the PhC depth. The simulated extraction lengths (for the first few low order guide modes) as a function of the PhC etch depth is presented in Figure 12b. The expected extraction lengths are compared to the metallic modal absorption. Here, one can conclude the PhC depth should be higher than 100 nm to benefit the extraction over the absorption and the further increase of the PhC depth is beneficial for the extraction length. This effect can be easily exploited provided that no damage to the active structure occurs during the PhC fabrication. In all cases, the PhC depth should remain optimized with respect to the total cavity thickness and QW position (to be in the minimum of the observed oscillations).

(2) Device processing for increased yield and repeatability

The development of a reproducible fabrication process with reasonable yield is an essential component even for the study of microcavity (MC) PhC LEDs. An overview of the the optimized process is described here. The starting material consisted of a conventional LED wafer on sapphire substrate, with a total III-nitride thickness of around 5 µm. First, III-nitride mesas extending down to the sapphire substrate were formed by ICP etching. Subsequently, the sidewalls of these III-nitride mesas were passivated with a thin layer of SiO_2, and an Ag-based mirror is deposited as the p-type contact. On top of the mirror, bonding metals consisting of a Ni diffusion barrier and a thick layer of Au were deposited. The sample was then flip-chip bonded to an Au-coated Si submount and the sapphire substrate was removed by laser-assisted lift-off. At this point, ICP etching was used to remove the exposed GaN base layer and thin down the

underlying *n*-GaN, and a grid type Al-based *n*-contact is deposited. Finally, PhCs were formed on the n-GaN surface by e-beam lithography and ICP etching.

The two most critical components in this process were the flip-chip bonding and laser lift-off. Optimization of these two steps has led to a dramatically improved yield compared to that in the beginning of this project. Today, by the means of Au-Au diffusion bonding at 300°C and single shot lift-off with a KrF excimer laser, we can reliably fabricate thin film LEDs with 70% yield over a sample size of 1 x 1 cm^2!

However, simply fabricating conventional flip-chip LEDs is insufficient. In fact, a precise control of the LED cavity thickness to within ± 15 nm is necessary in order to harness the full potential of microcavity light extraction. This level of precision has been achieved by employing a thin $Al_{0.15}Ga_{0.85}N$ etch-stop layer, which provides an adequate selectivity to GaN during an ICP etch in SF_6/BCl_3 based chemistry (GaN etches about 5 times faster than AlGaN in these conditions). The development of this method is described in the results for Task 2.

A cross sectional SEM of the as grown structure used for such MC LED processing is shown in Figure 13a. The angle-resolved EL spectrum of a 450 nm-thick MC LED is shown in Figure 13b. Notice that the spectrum contains only a single Fabry-Perot mode – a signature of the low order cavity.

(3) Experimental optimization of key device parameters

The particularities of the MCLEDs require that several parameters are carefully tuned to optimize the extraction efficiency. Thus, we have performed studies on the p-contact reflector, the PhC etching depth and the PhC lattice parameter.

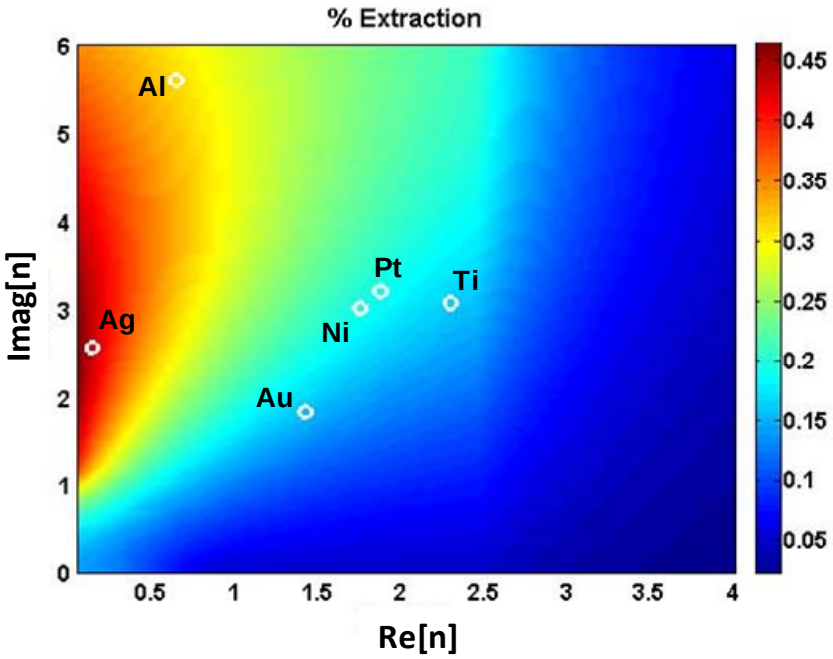

Figure 14 Influence of the metal mirror optical properties (real and imaginary parts of the refractive index) on the direct extraction into the air cone. The highest direct extraction is presented in red according to the color-scale on the right side. For comparison, the optical parameters at 450 nm for the most commonly used metals for p-contacts are denoted with white circles.

(a) Choice for reflective *p*-contact

The choice of the reflective *p*-contact for MC LEDs is one of the most important elements of the system. It has to offer very high reflectivity for the emitted by the QW light while in the same time providing good electrical characteristics (low resistivity ohmic contact). Various metals can be considered for *p*-GaN side mirrors. We have calculated the impact of the contact metal on the direct outcoupling from a MC LED as a function of the *p*-contact real and imaginary part of the refractive index (Figure 14). In Figure 14 are also noted the corresponding values for all metals commonly used as LED contacts. As seen two choices for contact metal offer significantly higher direct extraction than the others. Those are silver (Ag) and aluminum (Al). Indeed, for LEDs operating at 460 nm the reflectivity of a thick Al mirror is 91.5% (n = 0.474, k = 4.509 as determined by Elipsometry measurements and for a thick Ag mirror is 96% (n = 0.068, k = 2.651). Unfortunately, neither Ag nor Al forms an ohmic contact when directly deposited on *p*-GaN. Thus, a thin intermediate layer of Ni, Pt or Pd with thickness is 1 – 3 nm should be introduced. The most common contact to *p*-GaN is Ni/Ag (1 nm of Ni). In our first studies we have encountered that the commonly used Ni/Ag based mirror suffers damage during the flip-chip bonding process. This imposed a search for some alternate combination that does not contain Ag. A comparison of the optical and electrical properties of few test structures is given in Figure 15. The test LEDs (300 x 300 μm^2 wide mesas) have a standard *p*-GaN side up geometry with a large high reflectivity *p*-contact designed for light extraction through the Sapphire substrate. It should be noted that the values varies within a range of few percents from one device to another and the presented data represents the best obtained values for each design. As expected, we observe a drop of the light that is extracted from the LED structures that have Al based mirrors. However, Pt/Al and Pd/Al mirrors have the same electrical characteristics as the Ni/Al one for a optical loss of 25% (prior annealing/flip-chip bonding) and could be an interesting alternative to the Ni/Ag mirror. However, all further studies have been suspended as the developed Au-Au bonding process eliminated the previously observed degradation of the Ag mirrors (probably related to diffusion of the tin bonding layer) and none of the Al containing ones offers any other advantage. Besides, the high imaginary part of the Al refractive index would be significantly detrimental for the extraction of all guided modes. In conclusion, all MC LEDs will use a standard Ni/Ag high reflectivity *p*-contact.

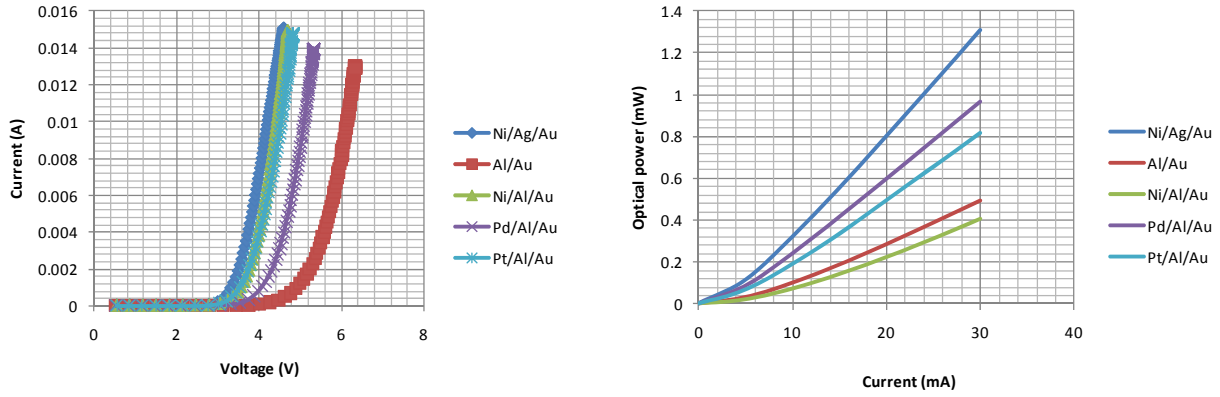

Figure 15 Electrical and Optical performance of 300 x 300 um2 wide LEDs with different p-contacts for an LED emitting at 440 nm

(b) Impact of PhC etch depth on output power

For thin devices such as MC LEDs the optimization of the vertical dimensions is much more important than for thick conventional PhC LED. In particular, our simulations have predicted that the extraction coefficient of the guided modes should be better for thinner cavities. The extraction length of the lowest order mode scales approximately as t^{-3}, where t is the thickness of the (unetched) core below the PhC. This trend alone suggests that as long as the unetched core is thick enough to support at least a single guided mode, the extraction efficiency should continue to increase as the thickness of the core is decreased. However, thinner designs also introduce a number of competing effects that can be detrimental to device performance. Specifically, reducing the cavity thickness can lead to increased absorption of the guided modes via the metal mirror and

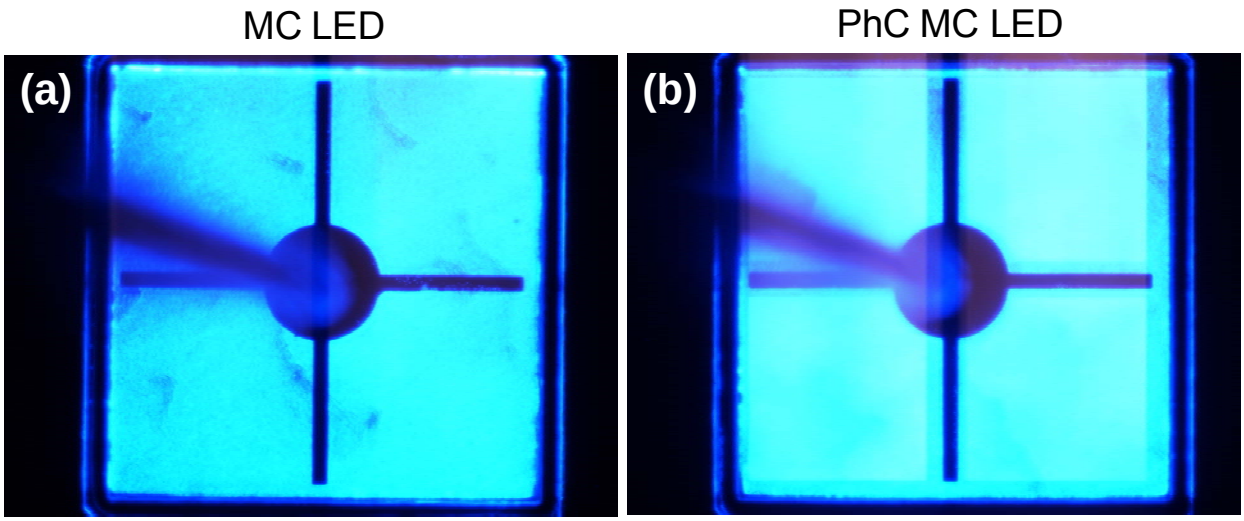

Figure 16 CCD images of 970 nm-thick microcavity LED (a) without PhC; (b) with PhC with etch depth of 260 nm.

increased spreading resistance in the *n*-type GaN. In addition, the device fabrication becomes more challenging, and etch induced damage proximal to active region may become a concern. To investigate these competing effects, 970 nm-thick MC PhC LEDs were fabricated with PhC etch depths of 90 nm, 260 nm and 440 nm, corresponding to core thicknesses of 880 nm, 710 nm, and 530 nm.

Optical microscope images of the unpatterned MC LED and the PhC MC LED with PhC depth of 260 nm operating under electrical injection at 5 mA are shown in Figure 16. Despite the thin nature of the *n*-type GaN, the emission appears uniform across both devices, indicating good current-spreading and uniform light extraction.

The on-chip output power at 20 mA, measured with a top-side photodetector (collection angle of ± 20°), is plotted for all measured devices as a function of etch depth of Figure 17a. The total output power (in integrating sphere), measured on-header without encapsulation, is plotted as a function of current in Figure 17b. The disparity between the top-side and total power enhancements is simply an indicator of the directionality of the PhC extraction.

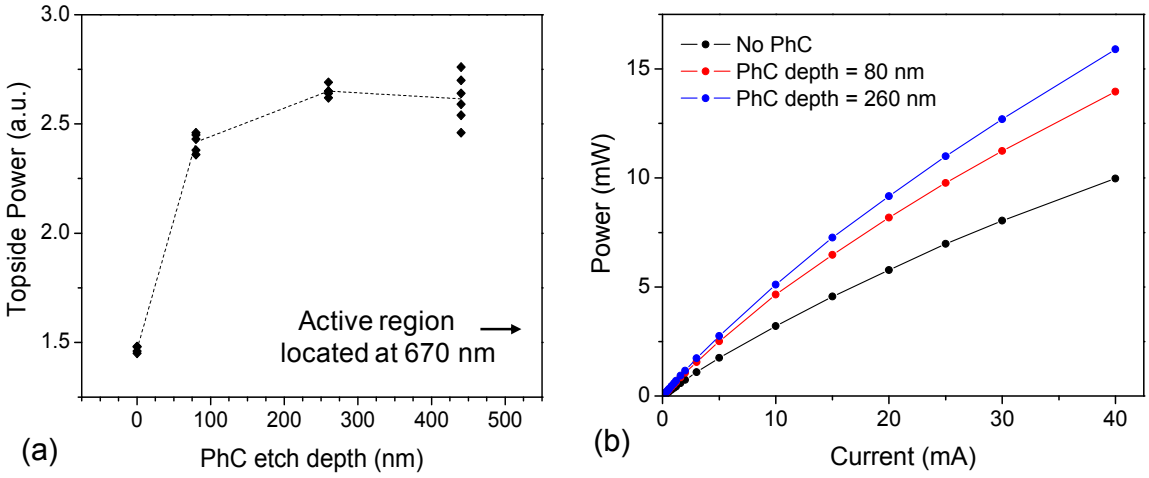

Figure 17 (a) L-I curves for unencapsulated microcavity PhC LEDs on-header, measured in integrating sphere. (b) On-wafer topside power at 20mA as a function of PhC etch depth.

For the shallowest PhC etch depth of 90 nm, the increase in topside output power over the unpatterned microcavity LED is 65%, corresponding to a 45% increase in total power. As the etch depth was increased to 260 nm, these enhancements grew to 80% and 65%, respectively. Devices with 260 nm-deep PhCs have an average output power of 9.1 mW at 20 mA, and a peak EQE of 21% at about 2 mA.

Further increase in the etch depth from 260 nm to 440 nm leads to limited increase of the output power, but also to a markedly increased scattering in the measured values. The origin of this scattering is related to the increased process variability across the sample due to the longer PhC etching times.

While an additional optimization study is still required. Currently, we can establish that a reduction of the core thickness down to 710 nm leads to increased light extraction, while the benefits of even thinner structures are limited by the added fabrication difficulty.

(c) Impact of core thickness on far-field patterns

Beyond the total extraction efficiency, the vertical dimensions of PhC MC LEDs can also be expected to have a strong impact on the directionality of the far-field emission. Specifically, the thickness of the unetched core below the PhC can be used to engineer both the number of supported guided modes and the overlap of each mode with the MQW, which will determine the fraction of the total emission that is carried by each mode. To explore this possibility, we have fabricated PhC MC LEDs with a total cavity thickness of 790 nm and PhC etch depths of 90 nm, 330 nm, and 440 nm. Notice that the thickness of the unetched core is reduced by half – from 700 nm to 350 nm – as the PhC depth is increased.

The angle-resolved EL emission patterns in TE-polarization along the ΓK direction are shown in Figure 18a, along with the corresponding wavelength-integrated far-field patterns in Figure 18b. For the thickest core, a relatively large number of modes is observed and the emission is distributed fairly equally amongst them, resulting in a far-field pattern without strong directionality at any particular angle. However, as the thickness of the unetched core is decreased, the number of modes decreases. For the thinnest core the majority of emission is concentrated in just two modes, and because these two modes are extracted near the center of the air cone (property tuned by the PhC lattice parameter), a strongly directional far-field pattern is obtained.

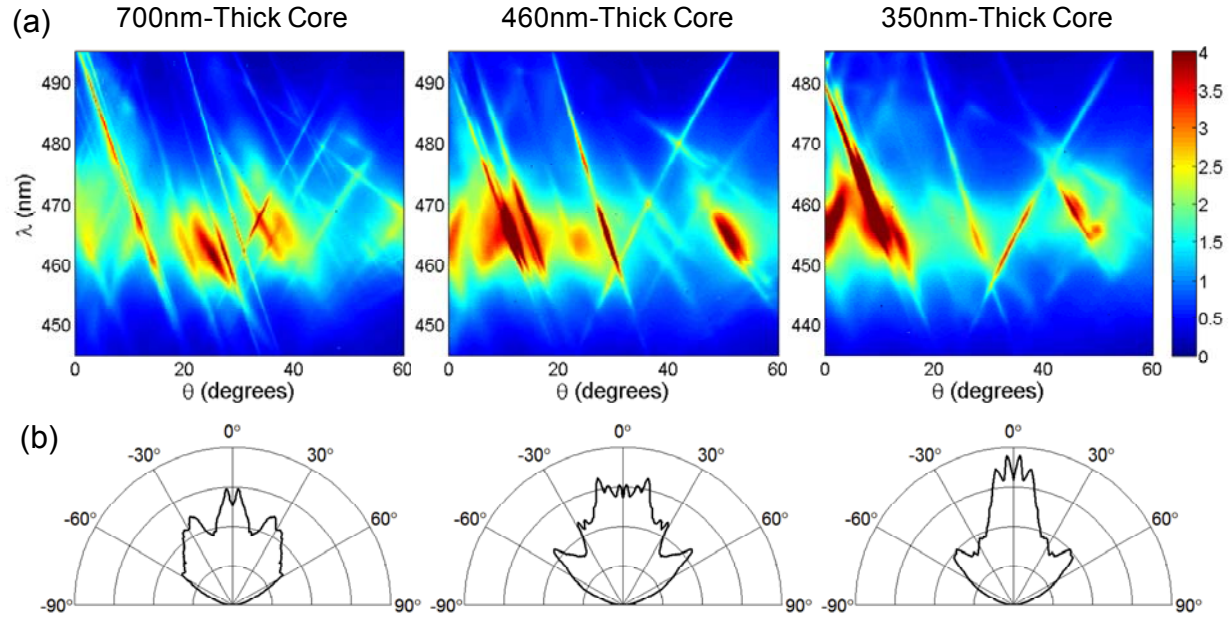

Figure 18 (a) Angle-resolved EL in TE-polarization along the ΓK direction for PhC MC LEDs with varying core thickness. (b) Corresponding wavelength-integrated far-field patterns.

These results demonstrate the power of vertical engineering as a tool to select a small number of well excited and extracted modes with which to tailor the overall beam shape of the MC PhC LED.

(d) The role of PhC lattice constant

Due to the absence of the sapphire substrate and the wider range of in-plane wave vectors amongst the set of guided modes, the optimal PhC lattice constants for thin-film LEDs will not be the same as for conventional GaN-on-sapphire devices. To investigate the role of the PhC lattice constant, 800 nm-thick microcavity LEDs were fabricated with triangular-lattice PhCs with lattice constants of a = 240 nm, 300 nm and 350 nm. The measured band structure for the device with a = 240 nm is plotted in Figure 18. The data is plotted along the ΓM direction and normalized by the lineshape of the quantum well emission. Notably, the structure supports a total of six guided modes and all of these modes were clearly observed in the measured data. This is in contrast to the case of a conventional thick LED, where it has been observed that low-order guided modes are not well-extracted by a surface-etched photonic crystal.

Measured far-field patterns corresponding to the three lattice constants are shown in Figure 19. In all cases, the emission patterns were strongly modified from Lambertian emission by the presence of the PhC. While the particular lattice constants used in this case resulted in lobed emission, it is possible to harness this same effect to generate vertically-directed emission as it have been exemplified earlier for the thinnest MC LEDs.

It is worth to comment also that the total light extraction increases as the lattice constant is increased beyond the 2nd Bragg order, departing from the case of GaN-on-sapphire devices where longer lattice constants are found to result in increased diffraction to the sapphire substrate.

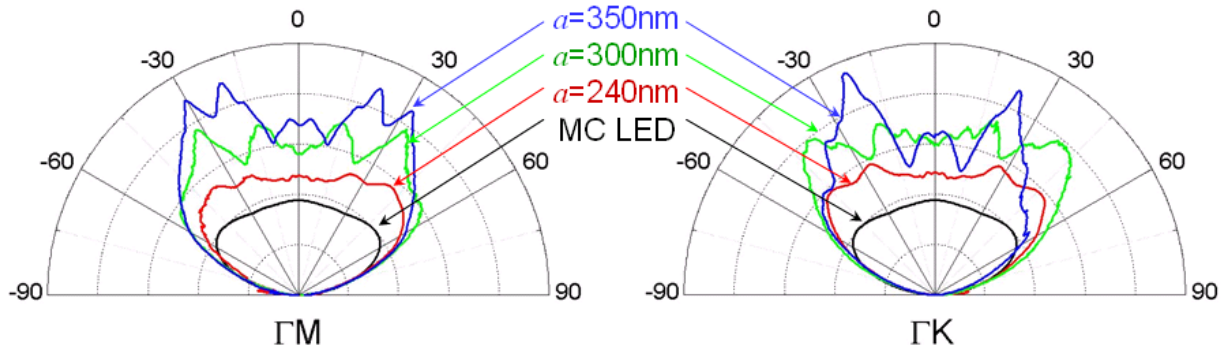

Figure 19 Measured far-field patterns for 800 nm-thick thin-film PC LEDs with varying lattice constant.

The measured output power, EQE, and electrical characteristics of the highest performing devices from this experiment are presented in the following section.

(4) High-performance thin-film PC LEDs

Optimized thin-film PC LEDs emitting at $\lambda \sim 500$ nm were fabricated with a cavity thickness of 800 nm, PC etch depth of $d = 150$ nm, and PC lattice constant of $a = 350$ nm. The PhC MC LEDs devices were compared to standard MC LEDs fabricated on the same wafer. Despite the small thickness of the GaN cavity, the LEDs show no signs of forward breakdown at current densities up to at least 300 A/cm^2. In addition, both the devices with and without PhCs exhibit similar I-V curves over a wide range of injection currents (Figure 20a). These results indicate that fabrication of photonic crystals with relatively shallow etch depths had little or no affect on the electrical characteristics of the device.

The total output power as a function of current is plotted in Figure 20a. The power was measured on unencapsulated devices mounted on silver headers in an integrating sphere. At an injection current of 100 mA, the PC patterning resulted in a 2.5 times increase in total output power over the planar MC LED.

The largest external quantum efficiency (EQE) is recorded at the current density of 25 A/cm^2 in both devices (MC LEDs with and without PhC), as shown in Figure 20b. The PC LED have a peak EQE of 8.8 %, compared with 3.8 % for the unpatterned device. Regarding the relatively low values of EQE, we note that the emission wavelength on the blue-green border may have resulted in lower-than-average internal quantum efficiency (IQE) for these devices. However, this issue remains to be quantified by measurement of the IQE. In addition, absorption by the metal mirror may be a significant source of loss in these devices.

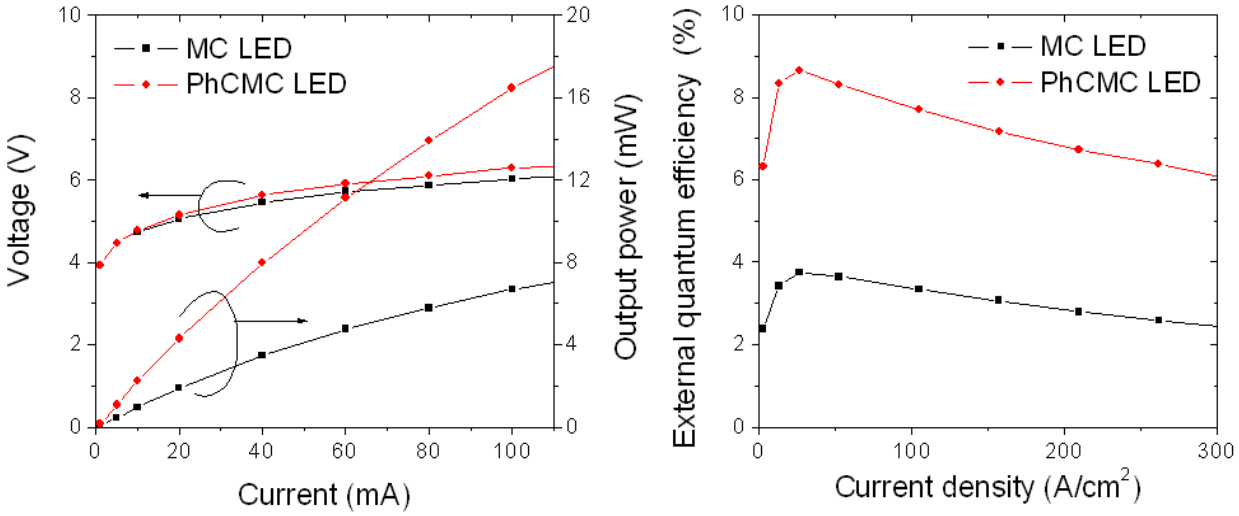

Figure 20 (a) I-V and L-I curves for 800 nm-thick microcavity PC LED with PC lattice constant *a* = 350 nm, and the unpatterned microcavity LED for comparison. (b) EQE-I curves corresponding to the L-I curves shown in (a).

A repeatable, high-yield process has been developed to fabricate thin-film PhC LEDs with GaN cavity thicknesses in the submicron regime. Devices with cavity thicknesses as small as 800 nm exhibited robust electrical characteristics under high current injection and negligible degradation as a result of PhC etching. The impact of PhC etch depth and lattice constant on the total output power, far-field emission pattern, and electrical characteristics of microcavity PhC LEDs have been investigated experimentally, and trends for optimizing these parameters have been determined. PhC extraction of *all* guided modes has been observed via angle-resolved EL, resulting in an increase in total output power of 2.5 times over unpatterned LEDs. A pathway to for fabrication of highly directional light sources has been demonstrated.

Design, fabrication, characterization, and optimization of LEO PhC-LEDs (Task 5 and 6)

Extensive research has been carried out for increasing the light extraction from LEDs by the means of PhC. Most of the effort relies on surface PhCs for which the observed enhancement in light extraction is usually quite lower than the theoretical limit. The latter is at large extent due to the low interaction of the surface PhCs with some of the guided modes. An alternative approach to surface PhCs (subject to the present studies) to increase the interaction of the guided modes with the PhCs is to embed the PhCs within the device. In addition to improved light extraction, advantages of the embedded PhCs include a simpler, planar contacting process, and the absence of possible etch-related damage introduced into the active region. The goal of the described here research effort is to develop and optimize a method to grow PhC LED templates with embedded PhC next to the active region. The proposed method is based on lateral overgrowth of a pre-patterned template which is highly common technique for treading dislocation reduction. Three structures have been developed and studied: dielectric gratings, gratings partially filled with dielectric material and air-gap gratings. The major difference between the final stages of those structures is the offered diffraction strength of the embedded 1D or 2D PhCs which is proportional to the index of refraction mismatch in the PhC layer. Here, the contrast in refractive index between GaN and dielectric materials is smaller than that between GaN and air, therefore we can conclude that embedded PhCs with air-gaps are capable of offering higher diffraction strength than dielectric-based gratings and potentially yield more efficient optoelectronic devices.

Thus, the first structures should be considered as concept demonstrations of air-gap embedded PhC.

(1) 3D simulations for advanced design

An LED with embedded PhC is schematically presented in Figure 21a. Several electromagnetic guided modes are supported in such structure due to the fairly thick GaN slab and we classify them in low order modes, high-order modes and the cap-layer mode (CLM), which of the mode confined in the cap layer by the embedded PhCs (Figure 21a). When PhCs are placed on the surface of the LED, which is the most common configuration, the low order modes interact poorly with the PhCs, due to their evanescent tail overlapping the surface PhCs. On the other hand, low order modes have the highest optical confinement with the QWs, thus are the best optically excited group of modes. Hence, a limited extraction of this group of modes limits considerably the extraction efficiency of surface PhC LEDs. The extraction of low order modes, as well as high order modes, is much improved by embedding the PhCs within the LED structure. The interaction of the PhCs with all the guided modes is fairly improved in this configuration which can be simply understood by the higher overlap of all modes with the embedded PhCs. A thorough optimization of the embedded PhC LED structure requires the consideration of the extraction length of all the supported modes in the structure which is a quite tedious simulation due to the extensive number of modes. A simpler analysis can be done by optimizing the extraction of the poorest extracted mode. The CLM is not only the mode with the lowest interaction with the PhCs, but also the best excited mode by the QWs due to its strong confinement in the cap layer. Therefore, to optimize the embedded PhC structure, one can focus

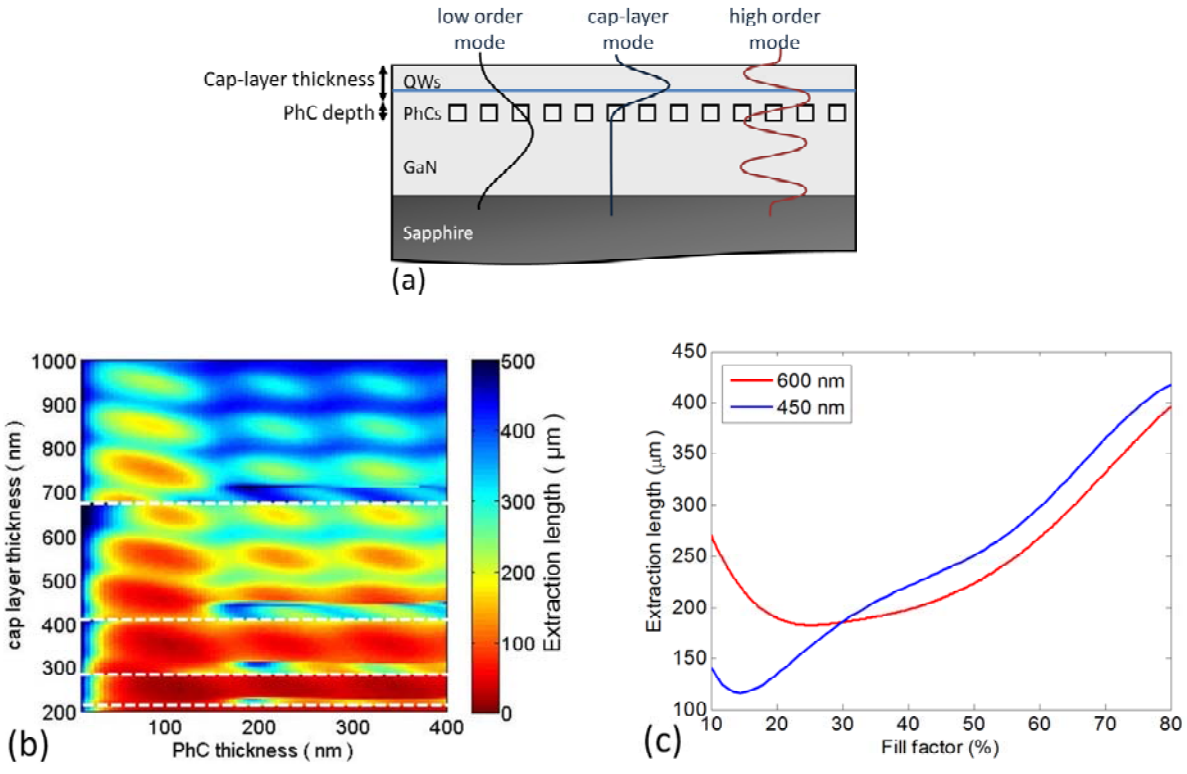

Figure 21 (a) Schematics of the embedded PhC LED. (b) Simulated extraction length of the CLM as a function of the cap layer and PhC thicknesses. (c) Extraction length as a function of the PhC fill factor for a 100 nm-thick PhCs and cap-layer thicknesses of 450 nm and 600 nm.

on the optimization of the extraction of the CLM since generally all the other modes interact well with the PhCs.

The problem is treated numerically to understand the effect of some of the parameter of the structure on the extraction efficiency of the LED, such as thickness of the cap-layer, depth and fill factor of the embedded air-gap PhCs. The diffraction strength of the PhCs on each guided modes is quantified by the characteristic extraction length $L_{extraction}$ which corresponds to the minimum length necessary to extract the guided mode. The modal extraction length is related to the imaginary component of the wavevector of the guide mode (or more precisely, Bloch mode) supported by the structure as $L_{extraction} = 1/2k"$. The wavevector of the guided modes in the complex space was calculated based on a full 3D scattering matrix formalism considering the PhCs with 35% fill factor above a 4 μm-thick GaN layer for a 460 nm wavelength. The simulated extraction length of the CLM as a function of the cap layer and PhC thicknesses is shown on Figure 21b.

The best extraction of the cap-layer mode is achieved for a PhC layer relatively thin (PhC thickness about 100 nm) and the thinnest possible cap-layer. The discontinuities at the dashed lines in this plot are due to the change of the order of the cap-layer mode as the thickness of the cavity varies. The oscillations seen in the extraction length represents variations on the CLM as a function of the cap layer and PhC thicknesses. In general terms, the best extraction of the cap-layer mode is achieved for a PhC layer relatively thin (PhC thickness around 100 nm) and the thinnest possible cap-layer. The discontinuities at the dashed lines in this plot are due to the change of the order of the cap-layer mode as the thickness of the cavity varies. The oscillations seen in the extraction length represents variations on the vertical resonances of the Bloch mode with the PhC layer. A numerical optimization was done for the PhC fill factor. The extraction length as a function of the PhC fill factor was calculated for a PhC thickness of 100 nm and cap-layer thicknesses of 450 nm and 600 nm (Figure 21c) while the rest of the structure was kept the same from the previous simulation. The optimal fill factor was found at 14% for a 450 nm-thick cap layer. These optimal values were used as a target to the fabrication of the structure.

(2) Structures

We have investigated the means to grow GaN-based embedded 2D- PhCs for highly efficient optoelectronic devices. The grating was optimally designed for the diffraction of wavelengths around 450 nm generated by InGaN multi-quantum wells (MQW) on GaN. The 2D triangular lattice grating periodicity ranged from 180 nm to 300 nm. We investigated the growth of three different embedded gratings: dielectric gratings, gratings partially filled with dielectric material and air-gap gratings. The final structures are schematically presented in Figure 22. We have successfully demonstrated embedded PhC gratings prepared by each of these methods.

The first technique is the fabrication of embedded dielectric PhCs. Here, we have demonstrated the coalescence of a GaN layer over the dielectric photonic crystals. The growth over small periodicity dielectric gratings is very sensitive to inhomogeneities in the dielectric mask as well as to mask decomposition at high temperatures. Both problems have been overcome by a two-step growth procedure. Although many extended defects were created in the GaN overgrown layer, they were mostly bent in the semi-polar facets inclined to the growth direction during coalescence. However, the fairly thick GaN layer as well as the relatively low index contrast between the used Si_3N_4 dielectric mask and GaN ($\Delta n \sim 0.4$) realized with this technique makes it less attractive for optoelectronic devices.

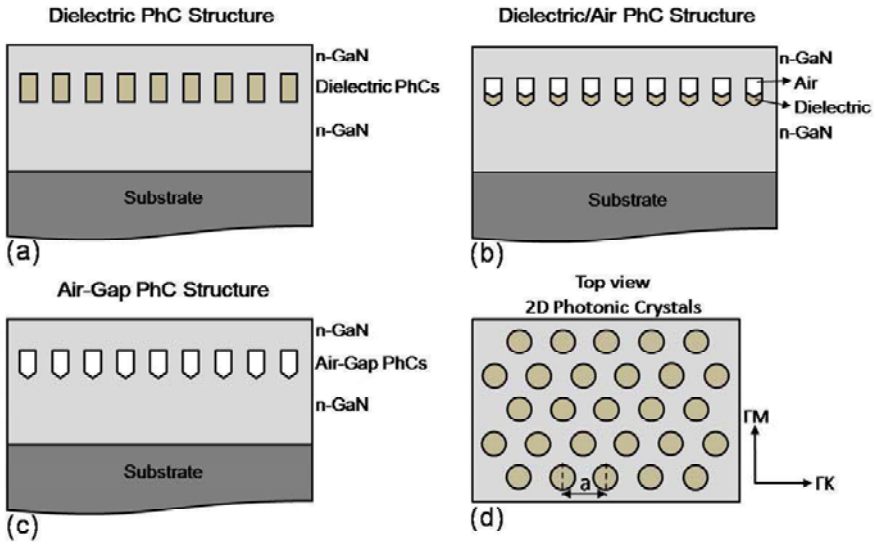

Figure 22 Schematics of the structures studied: (a) Embedded Dielectric PhCs. (b) Embedded Air/Dielectric PhCs. (c) Embedded Air-Gap PhCs. (d) Schematics of the top-view of the *a*-periodic, 2D triangular-lattice PhCs. The highly symmetric directions ΓM and ΓK of the PhC lattice are also shown.

The second technique is for the fabrication of Embedded Dielectric/Air PhCs. The growth over the larger GaN surface with dielectric material inside the small holes appeared more robust in terms of inhomogeneities in the patterned PhC layer and dielectric decomposition at high temperatures. The coalescence of planar and thin GaN layers was achieved in a single growth step. The volume of the embedded grating was mostly void except for the thin initial layer of SiO_2. The final structure is more attractive for optoelectronic devices than in the first technique due to the coalescence of fairly thin GaN layers over PhC holes. Additionally, the holes are mainly composed of air increasing the index of refraction mismatch in the PhC layer.

The third structure is Embedded Air-Gap PhCs. The technique relies on the difference of growth rates for the different crystallographic facets to embed voids within the GaN layer. It revealed to be the most stable technique, being more robust and simpler than all approaches previously described. Air-gap PhCs have been successfully embedded with a coalescence GaN layer that is only 90 nm thick. The coalescence of n-type GaN has been achieved with a RMS roughness of 2.95 nm (20x20 μm^2) for a 200 nm-thick coalesced layer. The coalescence of *p*-type GaN has also been achieved. The layers grown by this method are well adapted for optoelectronic devices due to the fairly thin coalesced layer as well as the high refractive index contrast given by the air-gaps. Furthermore, the embedded PhCs does not create additional defects in the coalesced GaN layer, yielding material of similar quality to the underlying GaN template.

The detailed study on the parameters and conditions to prepare LED templates by all three methods has been published and can be found in the work of Matioli *et al.* (J. Appl. Phys. **106**, 024309 (2009)). Given the significant superiority of the Embedded Air-Gap PhCs over the other two structures it is logically chosen to be pursued and studied more extensively. A detailed description of the technique of preparation of such devices is presented below.

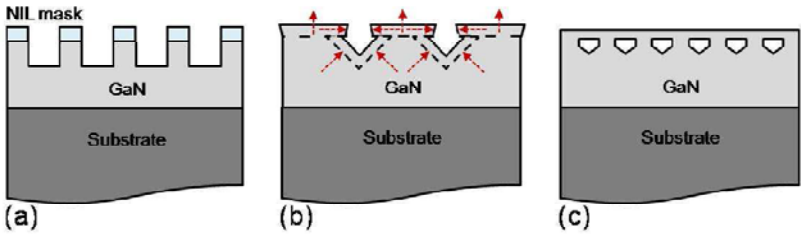

Figure 25 Schematics of the processing and growth of the embedded air-gap PhCs. (a) PhC was patterned by NIL and transferred to GaN. (b) Semipolar facets formed during regrowth by MOCVD which have a lower growth rate than the (0001) plane. (c) Air-gap PhCs were embedded after the overgrowth of GaN by MOCVD.

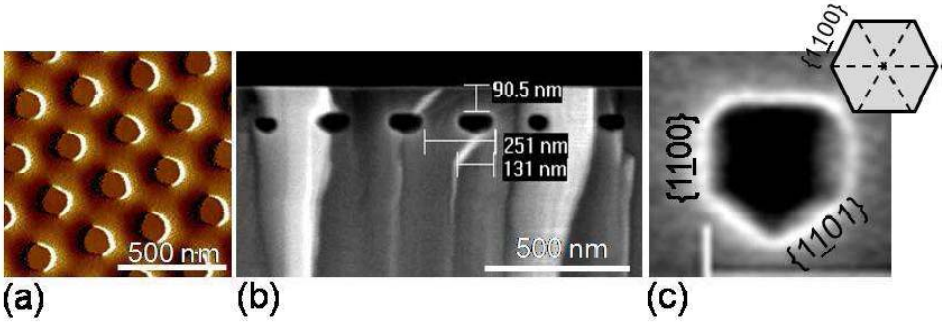

Figure 24 (a) Amplitude AFM image of the processed sample before growth. (b) SEM image of the overgrown coalesced layer over the air-gap PhCs. (c) SEM cross sectional image showing the ({1101}) and ({1100}) facets formed inside the holes during overgrowth. The inset depicts the top-view of the holes showing the orientation of its facets.

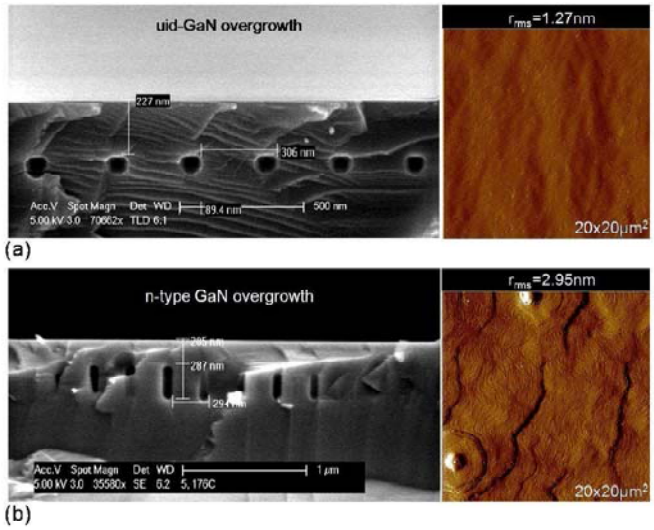

Figure 23 Cross sectional SEM and top-view AFM measurements of the embedded air-gap PhCs structure. (a) 90 nm-thick uid-GaN coalesced over the PhCs. The AFM image shows the surface morphology with an RMS roughness of 1.27 nm for a 20x20 μm^2 scan. (b) Coalescence of n-type GaN over the PhCs. The AFM image shows the formation of hillocks on the surface due to Si-doping. The RMS roughness of this sample is 2.95 nm.

(3) Fabrication of air-gap embedded PhC LEDs

(a) General process

The epitaxial layers are grown by MOCVD using trimethylgallium (TMG), ammonia (NH_3) and disilane (Si_2H_6) as precursors. GaN on sapphire templates are grown using a standard two-step process. Subsequently, a *n*-type GaN layer was grown using 6 slm of ammonia, 58 sccm of TMG, 0.88 sccm of Si_2H_6 and H_2 carrier gas. For the fabrication of embedded Air-Gap PhC structure the template has been subject to the following processing steps: a 250 nm-thick MR-I 7020 resist was deposited and patterned on the GaN surface by nano-imprint lithography (as described in Task 1), then the PhC pattern is transferred to GaN by reactive ion etching (RIE). The fabrication prior to MOCVD regrowth is then completed by removing the MR-I 7020 resist using the 1165 resist stripper at 80^o C.

During the regrowth procedure one can take advantage on the difference in growth rates between different crystallographic facets to embed void holes inside the previously processed structure. A formation of semi-polar facets ({1101}) inside the holes occurs during growth, independent of the original shape of the holes, due to the stability of these facets under the growth condition used. Under optimized growth conditions, the (0001) plane grows faster than the semi-polar facets producing voids after the coalescence of the overgrown layer (Schematics are shown in Figure 25). The *uid*-GaN was grown over the PhCs by MOCVD using the following growth conditions: 1165^o C, 85 Torr using 6 slm of NH_3 and 10 sccm of TMG. The cross section of a sample after the coalescence of a 90 nm-thick GaN layer over the air-gap PhCs is shown on Figure 13b. This cross section corresponds to the ΓK direction in real space. Figure 24c shows the ({1101}) and ({1100}) facets inside the holes that are formed during overgrowth and the inset depict the top-view of the holes, showing the orientation of these facets. Although the shape of the holes changed after growth due to the facet formation, their depth and width does not seem to be considerably altered after the regrowth step, indicating little lateral growth inside the holes. Thus, the PhC thickness can be easily controlled by changing the initial PhC etch depth.

The surface morphology of the overgrown layer is characterized by the formation of large islands that merged together as the lateral growth proceeded, leading to a coalesced film with RMS roughness of 10.6 nm for a 20x20 μm^2 scan. Smoother films can only be realized for thicker coalesced layers by either increasing the overgrowth time or the growth rate. The RMS roughness can be reduced from 10.6 nm to 1.27 nm when the GaN layer thickness was increased from 90 nm to 200 nm (Figure 23).

Although the coalesced layer grown over the air-gap PhCs is fairly thin, the application of this

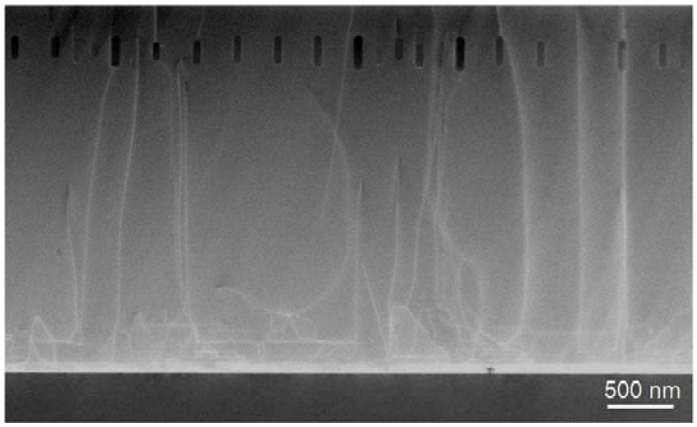

Figure 26 Cross sectional TEM image of the embedded air-gap PhC structure.

structure for optoelectronic devices would require a subsequent growth of the active region (comprising *n*-GaN, MQW and *p*-GaN) over this layer, increasing the overall thickness of the layer above the PhCs, consequently reducing the interaction of the guided modes with the embedded PhCs. It is desirable to obtain directly the coalescence of an *n*-type GaN layer over the PhCs. Figure 23 shows the comparison between the overgrowth of uid and *n*-type GaN, grown at the same conditions (1165^{o} C, 80 Torr, 6 slm of NH_3, 30 sccm of TMG). The n-type GaN was doped with 0.27 sccm of disilane which resulted in a doping concentration of ~ $1x10^{18}$ cm^{-3}. The thickness of the overgrown layer coalesced over the air-gap PhCs is similar for both cases, however the surface morphology is significantly different. The introduction of Si-doping led to the formation of hillocks, as seen in Figure 23d which increased the RMS roughness from 1.27 nm for the *uid*-GaN to 2.95 nm for the *n*-type GaN for a 20x20 μm^2 scan. Despite the rougher n-GaN surface, a bright LED composed of six MQWs and 270 nm-thick *p*-type GaN can be grown on this *n*-type GaN. While the increase in the surface roughness by Si-doping does not seem to be a problem for LEDs, further optimization may be needed when applying this technique to lasers.
The quality of the overgrown GaN layer was assessed by TEM measurements (Figure 26). The embedded air-gap layer did not create any new defects.

(b) Controlling the fill factor of the embedded air-gap PhCs

It is desirable for multiple embedded PhCs applications to be able to control their fill factor. While a higher PhC fill factor increases the diffraction strength of the PhCs, it also reduces the effective refractive index of the embedded PhC due to the higher volume of the air holes, which tends to confine better some of the guided modes away from the PhCs, reducing their spatial overlap. Here, the general trends are: for a higher PhC diffraction efficiency, shallow PhCs are more desirable. For confinement applications where the embedded PhCs serve the purpose of a low effective refractive index medium, higher fill factors are more desirable.
The fabrication of the embedded PhCs, as described earlier, relies on nano-imprint lithography (NIL) using a silicon hard mask to pattern the PhCs. The drawback of the NIL, in opposition to e-beam lithography, is the difficulty to make modifications on the final pattern, which is an exact copy of the hard mask used. Any modification requires the fabrication of new hard masks which can be tedious. The fill factor of the PhCs can be slightly increased after the pattern is transferred to the NIL resist, by the means of O_2 plasma. The fill factor can be even further increased by using longer etch time of GaN. Since the etch selectivity between GaN and the NIL resist is not high, the sidewalls of the resist are etched during the GaN etch, increasing its fill factor. Figure 27 shows the cross sectional SEM image of a sample with 150 nm diameter holes embedded on GaN, resulting in 39% fill factor. The GaN holes are etched with a depth of 300 nm by RIE using

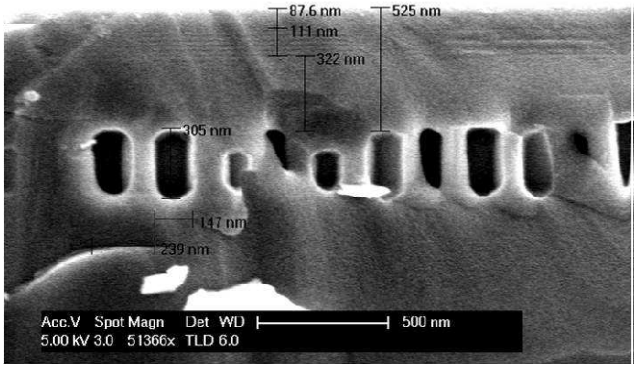

Figure 27 SEM image of the embedded air-gap PhC structure with high fill factor.

patterned NIL resist as etch mask. The resulting hole diameter is increased from 115 nm, for a regular 100 nm-deep embedded PhCs, to 150 nm. To obtain high aspect ratio embedded PhCs, with small diameter deep holes, one needs to deposit an etch mask with higher selectivity to GaN, such as dielectric layers of Si_3N_4 or SiO_2. This avoids the hole diameter to increase during GaN etch.

(c) Growth of embedded air-gap PhCs in p-type GaN

The coalescence of *p*-type GaN over the PhC is not as straightforward as that for the *n*-type GaN. The growth in this case is performed over a sample where the PhCs are etched in the *p*-doped GaN (Figure 28a). Here, the idea is to grow and coalesce a *p*-type layer over the air-gaps resulting in embedded PhCs over the active region. However, introducing Mg during the coalescence step of the p-GaN changes significantly the growth morphology resulting in an entirely coalesced layer, with no air-gaps embedded in the structure. Up to now the only solution for this problem is to

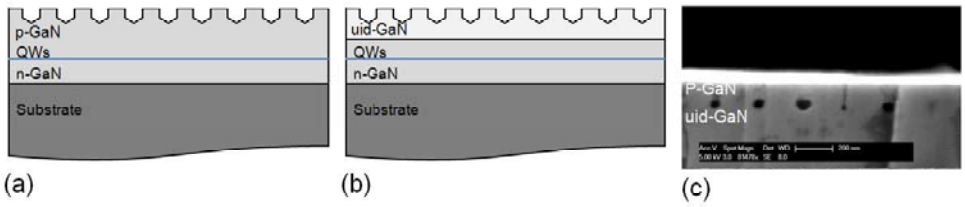

Figure 28 Schematic of the structure that failed (a) and succeeded (b) to embedded PhC on the *p*-type GaN. (c) SEM cross-sectional image of the embedded PhCs in the *p*-doped GaN layer.

pattern the PhCs on an uid-GaN layer above the QWs, perform the growth of uid-GaN until coalescence and subsequently grow *p*-GaN (Figure 28a). For this method, the uid-GaN is grown using similar growth conditions as previously described: 1165°C, 85 Torr using 6 slm of NH_3 and 10 sccm of TMG for 200s, which is the time necessary to achieve coalescence of a planar uid-GaN layer over the PhCs. Subsequently, 200 sccm of Cp_2Mg was used to dope the following layer and another 200 s of growth was performed. A SEM image of the final structure is shown in Figure 28c.

(4) Performance of embedded PhC LEDs

The LED structure of our best performing embedded PhC devices consists of a ~ 3 µm-thick n-GaN followed by a 100 nm-thick layer of air-gap PhCs, with period of 230 nm (12% fill factor),

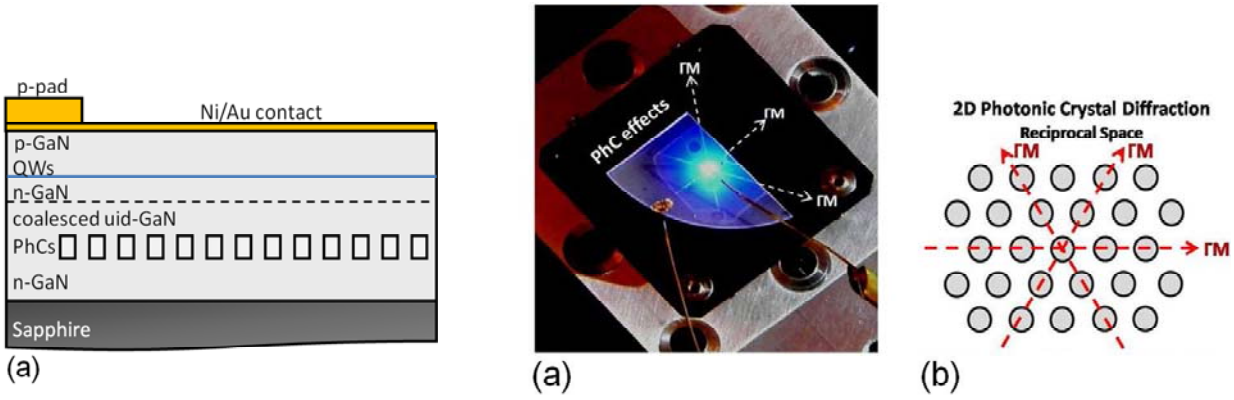

Figure 29 (a) Schematics of embedded 2D-PhC LED. (b) Picture of embedded 2D-PhC under electrical injection in quick test. Note the PhC diffraction in a star shape along the ΓM directions. (c) Schematics of the 2D-PhC reciprocal space indicating the ΓM directions

and a 540 nm-thick active region comprised of a 300 nm-thick n-GaN layer, 6x-InGaN QWs

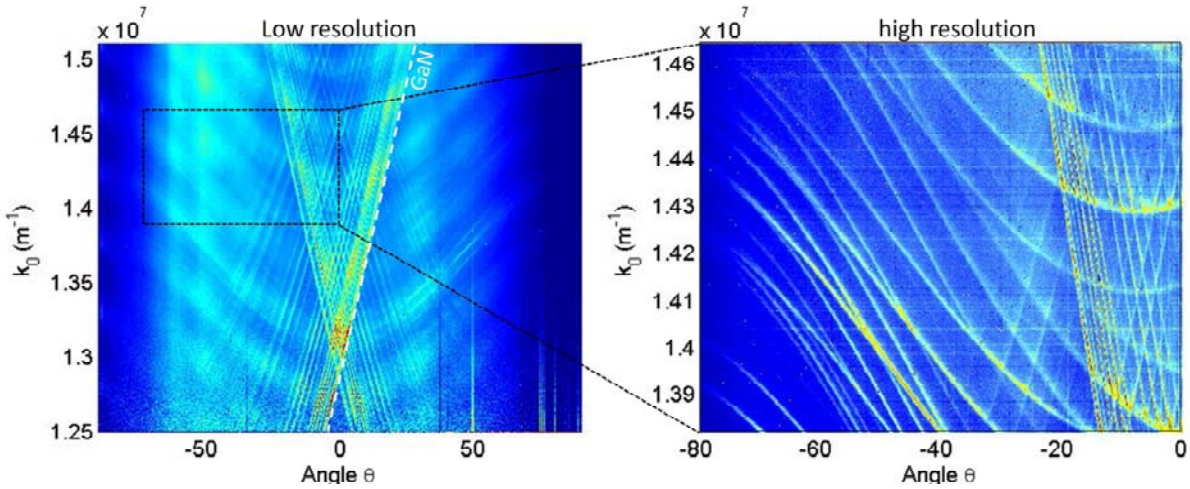

Figure 30 (a)Low resolution angle-resolved measurement of the far field emission from the embedded PhCs LED. (b) High resolution angle-resolved measurement.

emitting at λ = 445 nm and a 110 nm-thick *p*-GaN layer (Figure 29a). The 2D triangular-lattice air-gap PhCs were embedded within the GaN layer by the growth method described earlier. The device size is 800x800 μm^2 and the current are injected through a circular *p*-contact (diameter of 100 μm) in the center of the device to separate the metal absorption from the PhC extraction of the guided modes.

For such devices the vertical resonances of the cap-layer mode are not the same as for the other modes, hence the optimal set of parameters for the cap-layer mode cannot be the same for all of the guided modes. Thus, some modes will be in anti-resonant points and will be less efficiently extracted by the PhCs. However, this is not a concern here since the structure considered is thick enough to support several modes and the resonant effects will average out.

The measurement of the extracted guided modes has been performed by an angle resolved electroluminescence setup, where the spectrum of the LED under electric injection is measured for all angles θ from 0◦ to 180◦. The collection of all the spectra versus angle, after a proper conversion of axis as (θ, λ) → (θ, k_0), reveals the dispersion relation of the extracted guided

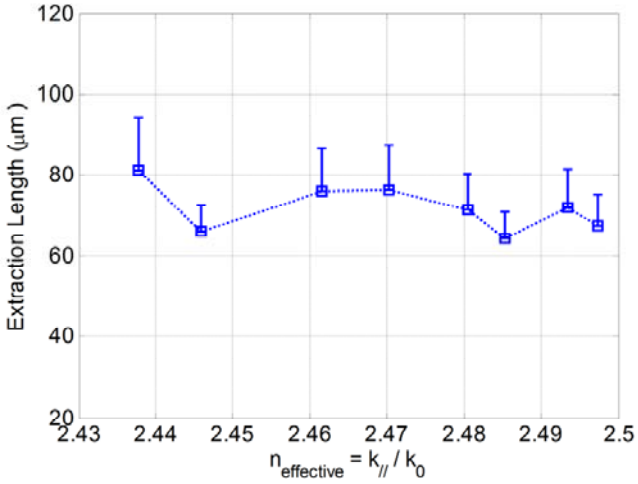

Figure 31 Experimental values of extraction length of the low order modes revealing a much shorter extraction lengths compared to surface PhCs.

modes. The results are presented in Figure 30a. The sharp lines observed in the angular measurement come from the diffraction by the PhCs of the guided modes inside the LED structure. The extraction length of the guided modes is then measured using the method described in the Appendix 3. The high-resolution angle-resolved measurement need for the aforementioned analysis is shown in Figure 30b. It is worthwhile noticing the higher number of modes diffracted by the embedded PhCs, especially the well diffracted modes observed between −80◦ and −20◦ in Figure 30b. Such modes are not observable from the surface PhC LEDs. The extracted values of the extraction length for the low order modes are in the range of 64 - 80 µm (Figure 31). These values are much lower than the 91-120 µm found for the low order modes in a similar structure with surface PhCs (Appendix 3). Moreover, the extraction of all low order modes is observed.
The PhC period a = 230 nm is designed to enhance the LED vertical emission. The directional diffraction of the guided modes can be also seen from the angle resolved measurements on Figure 30a, where the diffracted modes are mostly concentrated in angles between -30◦ and 30◦. The vertically emitted power (NA = 0.5) of the LEDs as a function of the current is measured by placing a power meter 5 mm above the device. The result is presented in Figure 32. The red curves correspond to the non-PhC LED and the blue to the embedded PhC LED. The dotted curves correspond to the extreme performances obtained among all the devices measured. We compare the average performing devices in order to account for the effect of the IQE variation over the wafer (solid lines). Thus, an average enhancement of 3.5 times on the vertical output power was determined. The electrical characteristics are not modified by the inclusion of the embedded PhCs which shows that no additional series resistance is introduced into the device (Figure 32b).
An important figure of merit to quantify the light extraction by the embedded PhCs is the extraction efficiency ($\eta_{extraction}$), defined as $\eta_{extraction} = \eta_{EQE} / \eta_{IQE}$, where η_{EQE} and η_{IQE} are the external and internal quantum efficiencies, respectively. η_{EQE} as a function of the current density is determined from the measurement of the total output power of the average-performing devices in an integrating sphere for both embedded and non-PhC LEDs, presented as dotted lines in Figure 33a,b, respectively. The total output power of the same devices after encapsulation in a silicone dome for both embedded and non-PhC LEDs is also shown in in Figure 33 (solid lines). The internal quantum efficiency (η_{IQE}) of the devices without PhCs is estimated using the model

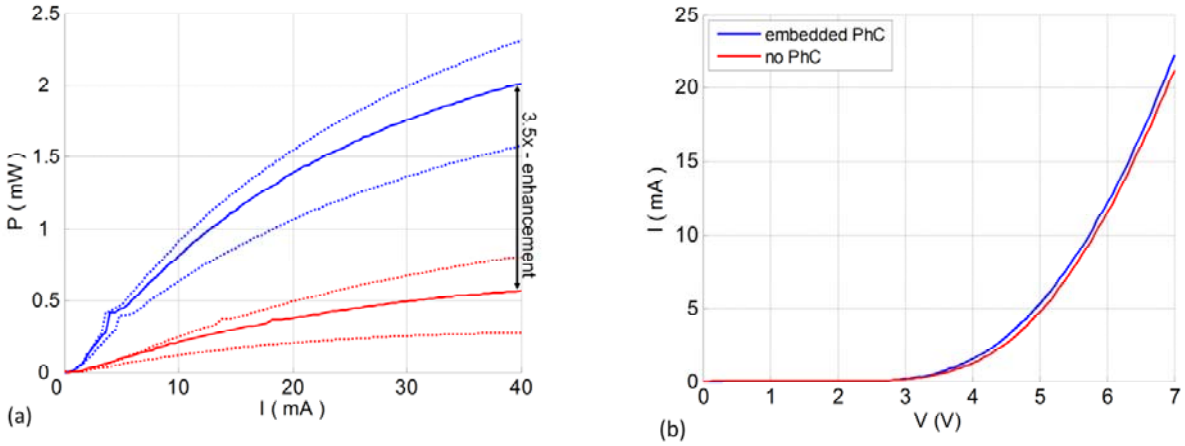

Figure 32 Optical and electrical properties of embedded PhC LEDs. The blue lines correspond to devices with PhC and the red lines correspond to test devices without PhC fabricated by a similar process.

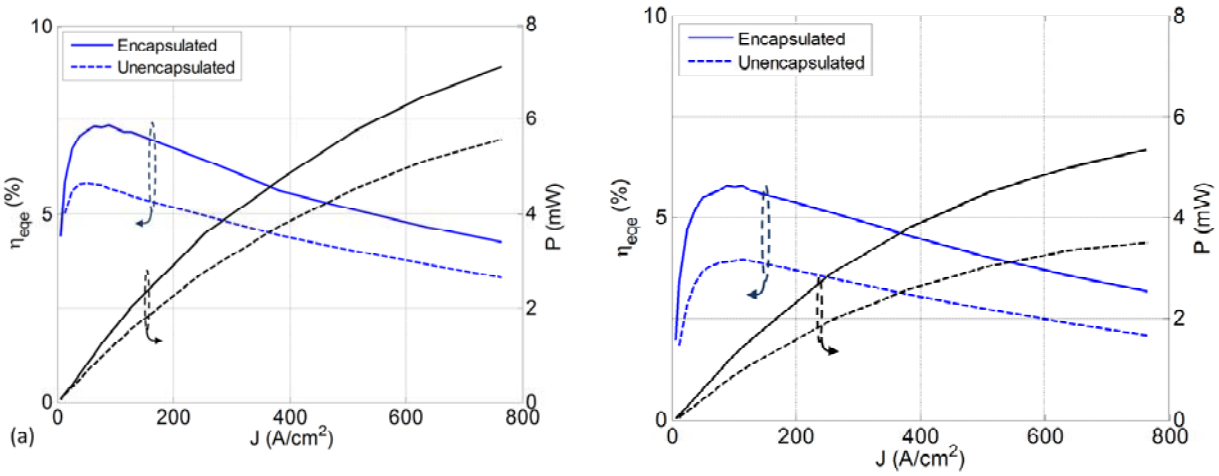

Figure 33 Dependence of the external quantum efficiency (measured in integrating sphere) on the current density: (a) For embedded PhC LED, (b) For a no-PhC LED.

described in Appendix 1. The value of η_{IQE} for these LED templates is found in the range of 7.4-7.9%. We can safely assume that the embedded PhCs do not affect considerably η_{IQE}. This statement is supported, thought not proven, by the negligible change in the shape of the EQE dependence on the injection current. Additionally, the internal quantum efficiency is unlikely to be superior that that of planar LEDs, which in the worst case would result in an underestimated extraction efficiencies for the embedded PhC LEDs. Taking into account the above considerations we can determine the following values for the extraction efficiency of non-encapsulated devices: 68-77%, or an average of 73% for the embedded PhC LED and 49-53%, or an average of 51% for the non-PhC LED. For the embedded PhC LEDs the extraction efficiency is determined to go up to 94% after encapsulation in a silicone dome.

In conclusion, we have demonstrated the possibility of coalescence of very thin GaN layers over void PhCs (as thin as 70 nm). The main parameters of embedded PhCs have been optimized for highest light extraction in LEDs. As a result the embedded PhC LED presents a very directional light emission with an enhancement of 3.5 times compared to the non-PhC LED for the vertically emitted light. An 73% extraction efficiency is achieved for the non-encapsulated embedded PhC LED and a 94% after silicone encapsulation.

Analysis and conclusion

In the framework of the present project we have developed and optimized three different PhC LED structure: AlGaN IGL LEDs, surface PhC MC LEDs and embedded PhC LEDs. We have shown that these structures offer an increased light extraction over both conventional LEDs and surface PhC LEDs. In addition, we have performed series of in depth studies of their properties in order to define the advantages and disadvantages of each design. In the following discussion we will compare the three offered designs in term of their extraction efficiency and emission directionality. As we have demonstrated the technical feasibility of all designs, we comment on the impact on the overall LED efficiency.

Our first structure is AlGaN IGL PhC LED. The elements that are defining its extraction efficiency are the surface photonic crystal and the AlGaN index confining layer which is the novelty in our design. When these structures are compared to similar LEDs without the IGL in terms of overall extraction efficiency, we measured an increase of 17% of the total emitted power. This enhancement is moderate and it comes at a cost. In fact, the incorporation of thick AlGaN layers in LED structure is tricky and results in devices with increased resistivity and reduced process yield. These issues render AlGaN IGL unattractive way to increase the overall extraction efficiency in LEDs. Nonetheless, for the devices with IGL we are measuring an increase of over 75% of the vertically outcoupled light compared to those without. This is an interesting property to consider for highly directional light sources. However, the origin of this improvement is in the much better excitation of the cap layer mode and not in the better overall mode extraction. In fact, the AlGaN IGL confines a single mode in the cap-layer, which is much better excited by the QWs. In the same time experimental measurement of the extraction length of all modes shows that although the CLM is better extracted than the other low order modes, its extraction length is still high compared to the high order modes. The latter also explains the small overall enhancements of the output power. In conclusion, we should state that AlGaN IGL PhC LEDs have limited potential as high efficient light sources where their only major advantage over standard PhC LEDs is the possibility to achieve highly directional light. Meanwhile the ability to observe a single mode that strongly interacts with both the active region and PhC makes the structure very interesting for studies of the light matter interactions in LEDs.

The second structure is a surface PhC MC LED. The direct light extraction in those devices is increased trough the microcavity effect occurring in such thin structures. This enhancement is difficult to assess experimentally as such LEDs cannot be directly compared to standard ones due to significant differences in their vertical dimensions. Nevertheless the microcavity effect is well understood and easily simulated numerically. For our structures we have estimated that about 30% of the emitted light should be directly emitted into air solely due to it. The remaining as guided light is extracted by the added surface photonics crystal. Its effect in our MC LEDs is estimated to increase the extraction by 2.5 times over a similar unpatterned device. In addition the low-number of supported guided modes allows precise tailoring of the far field emission pattern for achieving highly directional light sources. Despite these promising results, the surface PhC MC LEDs still exhibit one significant drawback. In fact the extraction length of the guided modes is still in the same order as the absorption length due to the large modal overlap with the bottom mirror. This issue can be addressed by either reducing the mirror absorption or enhancing the extraction by the PhC. Here the former would require engineering the high reflectivity bottom contact by compromising between low resistivity and low absorption. On the other hand the latter could be readily achieved with the use of embedded PhC instead of surface ones. Finally, we can

conclude that at the current stage the PhC MC LEDs exhibit high light extraction efficiency, good electrical properties and high yield process that allow considering those devices for industrial implementation with good potential.

The final third structure is an embedded PhC LED. Devices based on this design rely on the extraction of the guided modes by a grating introduced between the active region and the substrate, allowing both the appearance of a cap-layer mode and high overlap of all modes with the PhC. We have demonstrated the feasibility of three variations for the PhC grating where there main difference is their refractive index contrast. For the best performing air-gap embedded PhC we have shown an optimized process with high repeatability for high quality LEDs. At the current stage the only concern during the device preparation is the unknown impurity incorporation before the second growth step. Nevertheless, the simplicity of this planar fabrication process makes the embedded PhC very appealing for industry implication. In addition, the performances of the embedded air gratings as light extractor are quite astonishing. The modal extraction lengths are very low, being twice smaller ($L_{extraction} \sim 60 - 80$ μm) than that for most structures based on surface patterning. In terms of extraction efficiency, we can measure values ranging from 61% to 73% for unencapsulated LEDs. Those values were only limited by the large portion of the light emitted in the sapphire substrate. This problem is however easily solved by encapsulating the devices with a silicone dome. The resulting extraction efficiency is 86% on average and goes up to 94% for some devices. In addition to these remarkable results, the embedded PhC LEDs exhibit also highly directional light emission where the measured in vertical direction light is 3.5 times higher than that of a standard LED. In conclusion embedded PhC LEDs are state of the art devices that offer very high light extraction efficiency, where the latter can potential approach unity. In addition, the simple and planar fabrication process makes the technique easy to implement in industry.

Considering the performances and drawbacks of the three designs of PhC LEDs proposed in the framework of the present project we are convinced in the superiority of the embedded PhC gratings. The parameters and fabrication of these structures has been optimized and currently, a high yield planar fabrication process is available, offering state of the art external quantum efficiency up to 94 %. Meanwhile one should not underestimate the potential of MC PhC LEDs where their most interesting property is the possibility to produce highly directional light sources combined with high light extraction efficiency. For these devices we have demonstrated a high yield fabrication process as well as a pathway for tailoring their far-field emission pattern. Here, replacing the surface PhC grating with an embedded one will be the way to eliminate the negative effect of the significant mirror absorption. Finally, the AlGaN IGL PhC LEDs remain as an excellent model system to study the light-matter interaction inside LEDs.

9. Deliverables:

(a) Publications

1. A. Getty, A. David, Y. Wu, C. Weisbuch, and J. S. Speck, Jpn. J. Appl. Phys. Part 2 (Lett. & Express Lett.) **46**, L767 (2007).

2. Y.-S. Choi, M. Iza, E. Matioli, G. Koblmuller, J. S. Speck, C. Weisbuch, and E. L. Hu, Appl. Phys. Lett. **91**, 061120 (2007).

3. Y.-S. Choi, M. Iza, E. Matioli, G. Koblmuller, J. S. Speck, C. Weisbuch, and E. L. Hu, Proceedings of the SPIE - The International Society for Optical Engineering **6910**, 69100R (2008).

4. K. McGroddy, A. David, E. Matioli, M. Iza, S. Nakamura, S. DenBaars, J. S. Speck, C. Weisbuch, and E. L. Hu, Appl. Phys. Lett. **93**, 103502 (3 pp.) (2008).

5. Y.-S. Choi, M. Iza, G. Koblmuller, C. Hurni, J. S. Speck, C. Weisbuch, and E. L. Hu, phys. status solidi (c) **5**, 2306 (2008).

6. Getty, E. Matioli, M. Iza, C. Weisbuch, and J. S. Speck, Appl. Phys. Lett. **94**, 181102 (3 pp.) (2009).

7. E. Matioli, S. Keller, F. Wu, Y.-S. Choi, E. Hu, J. Speck, and C. Weisbuch, J. of Appl. Phys. **106**, 024309 (8 pp.) (2009).

8. E. Matioli, M. Iza, Y.-S. Choi, F. Wu, S. Keller, H. Masui, E. Hu, J. Speck, and C. Weisbuch, phys. status solidi (c) **6**, S675 (2009).

9. E. Matioli, E. Rangel, M. Iza, B. Fleury, N. Pfaff, J. Speck, E. Hu, and C. Weisbuch, Appl. Phys. Lett., **96**, 031108, (2010).

10. E. Matioli, B. Fleury, E. Rangel, E. Hu, J. Speck, and C. Weisbuch, J. Appl. Phys. **107**, 053114 (2010);.

11. E. Matioli, B. Fleury, E. Rangel, T. Melo, E. Hu, J. Speck, and C. Weisbuch, Appl. Phys. Express, **3**, 032103, (2010).

(b) Networks and collaborations fostered

Not applicable

(c) Technologies/Techniques

Not applicable

(d) Inventions/Patent Applications

The following patent disclosures have been submitted under the support of this DOE program:

2007-460: SELECTIVE DRY ETCHING OF N-FACE (Al,In,Ga)N HETEROSTRUCTURES (disclosure received 2/27/07)

2007-594: HIGH QUALITY GROUP-III NITRIDE GROWTH BY PLASMA-ASSISTED MOLECULAR BEAM EPITAXY UNDER N-RICH AND HIGH-TEMPERATURE GROWTH CONDITIONS (disclosure received 4/30/07)

2008-201: HIGH EFFICIENCY LIGHT EMITTING DIODE (LED) WITH SHAPED LIGHT EXTRACTORS GROWN OVER (disclosure received 9/18/07)

2008-466: HIGH EFFICIENCY THIN FILM LIGHT EMITTING DIODE (LED) WITH OPTIMIZED CONTACT ELECTRODE (disclosure received 1/24/08)

2009-493: OPTOELECTRONIC DEVICES WITH EMBEDDED VOID STRUCTURES

(e) Other products

Not applicable

Appendix 1 - Electroluminescent measurement of the internal quantum efficiency of light emitting diodes

The determination of internal quantum efficiency (IQE) in nitride-based light-emitting diodes (LEDs) is an ongoing challenge. Many factors affect how carriers are injected electrically in the active material, recombine via radiative or nonradiative processes, and how generated photons are emitted outside or reflected internally within the device and potentially dissipated into the material (e.g., by metal contacts, quantum wells, defects, *etc.*). That is the reason to be interested in development of a robust method to determine

Description

The most easily accessible efficiency parameter to measure for a given LED is the external quantum efficiency (EQE) which defined as the ratio of optical output power to injected electron-hole pairs:

$$P_{out} = \eta_{EQE}\left(\frac{h\upsilon}{q}\right)I$$

And is related to the three efficiency parameters:

$$\eta_{EQE} = \eta_{injection}\eta_{radiative}\eta_{extraction}$$

Here, I is the injected current and P_{out} is the emitted power measured by a detector such as an integrating sphere. Separating the components of η_{EQE} is a difficult challenge. The injection efficiency ($\eta_{injection}$) is the fraction of injected carriers which become excited e-h pairs in the active layer. The radiative efficiency ($\eta_{\mathrm{radiative}}$) is the fraction of electron-hole recombinations in the active region which generate photons. The combined efficiency of $\eta_{injection}\eta_{radiative}$ is referred to as internal quantum efficiency (η_{IQE}). Finally, the extraction efficiency ($\eta_{extraction}$) is the fraction of the generated photons that escapes the material. It depends on device geometry and the optical characteristics of the materials.

Temperature dependent photoluminescence (PL) is the most common method for the measurement of IQE [1-3]. For this method the nonradiative recombination processes, being phonon mediated, are assumed to be completely suppressed at low temperature (LT) resulting in $\eta_{IQE} = 1$, so at any higher temperature $\eta_{IQE}(T) = \frac{P_{out}(T)}{P_{out}(LT)}$. This implies that absorption, injection, and extraction efficiencies do not change with temperature. Estimating the LED's IQE with this method also presumes that the efficiency exhibited with PL is the same as with electroluminescence (EL) in devices, despite fundamental differences between PL and EL such as the mechanism by which carriers are delivered to the quantum wells, the band profile changes under bias (EL) and without bias (PL), and the resulting changes in emission wavelength, effective well width, and wave function overlap in polar materials exhibiting the quantum-confined Stark effect.

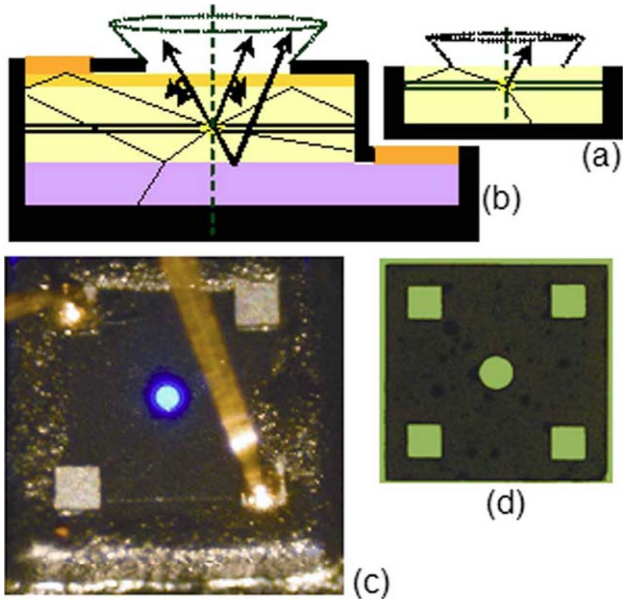

Figure 1-1 (a) Cross section of a simplistic device for modeling light extraction. (b) Cross section of the fabricated and modeled device for IQE measurement. (c) Illuminated LED device with patterned absorber. (d) Patterned photoresist-carbon black mixture for topside of LED devices. Extraction apertures range in diameter from 5 to 300 μm.

An alternative to the PL based IQE-measurement method, we propose the fabrication of an optically simple device designed for EL operation, whose extraction efficiency can be rigorously modeled, thus allowing us determining IQE from the measurement of EQE and the calculation of $\eta_{extraction}$. There are two prerequisites to this method: a device of sufficient optical simplicity and a sufficiently rigorous simulation of the light extraction.

The simplest device to model would be a slab of semiconductor with a planar quantum well embedded within, surrounded on the backside and sidewalls with an indexmatched, optically absorbing material Figure 1-1a. Only EL photons striking the uncoated top side of the device within the critical angle would be emitted and detected; photons with any other direction would be absorbed. In practice, a more complex device and model are required Figure 1-1b. Here, typical LEDs are grown via heteroepitaxy and include an interface at the substrate. The latter is responsible for appearance of Fabry–Pérot interference and extraction of some back emitted light after reflection on the substrate interface. In addition, to achieve uniform recombination across the whole device, a thin current-spreading layer of indium tin oxide or Ni/Au would be added to the top *p*-type layer, which will absorb some of the emitted photons. Contacts for electrical injection must be included, along with associated mesa sidewalls. To separate these optical features with uncertain properties from the area of photon collection, the topside of the device can be covered with a light absorbing material, except in the area of a circular aperture laterally separated from the contacts pads and sidewalls by tens to hundreds of microns. Additionally, the top surface of the semiconductor must be smooth, as light extraction from a rough surface is difficult to model.

An optical image of the LED described above is presented in Figure 1-1. Except for the circular aperture and contact pads, the device is entirely coated with absorbing material: Flat black paint on the backside and sidewalls and a mixture of carbon nanoparticles (4 nm particle diameter, Superior Graphite Co.) and photoresist (AZ4210), patterned via lift-off, for the top side. The top side absorber mask design with an aperture for light collection and windows over the

contact pads is shown in Figure 1-1d. The Aperture diameters are varied from 5 to 300 μm. The LED within correspond to the structure whose IQE we are interested in. Here for example we use standard multiple QW layer grown on sapphire substrate. The QWs emission is centered at 445 nm with a linewidth of 20 nm (full width at half maximum).

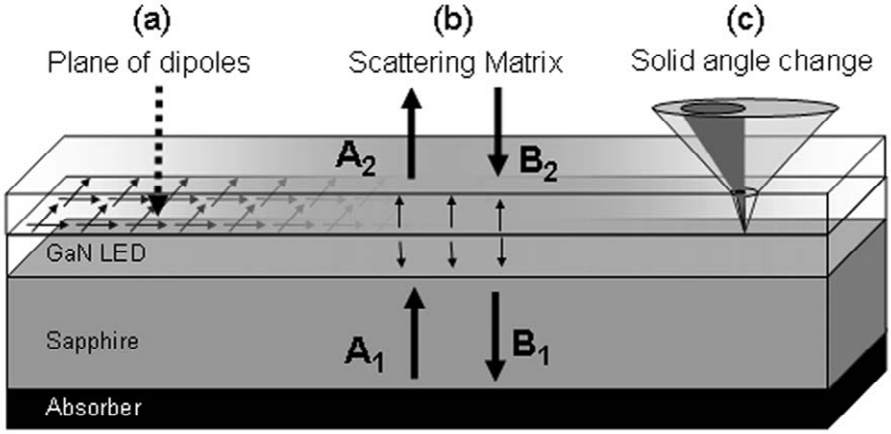

Figure 1-2 (a) Light emission from the quantum wells was modeled as a plane of uniformly distributed dipoles at the top (*p*-side) surface of the quantum wells. (b) Emitted light from the dipole sources was propagated through the structure using the scattering matrix technique. The sources appear as a discontinuity in the scalar electromagnetic fields. All light impinging upon the backside absorber is lost (A_1=0). (c) The final emission pattern within the material is then diffracted through the top surface, widening the emission cone and decreasing the power density.

The extraction length is calculated for the exact test device using a model based on dipole emission and scattering matrix formalism written in MATLAB. The rate of spontaneous transitions of electron-hole pairs between the conduction and valence bands in a quantum well given by the Fermi's golden rule is proportional to the optical matrix element $|\langle i|\vec{\eta}\vec{p}|f\rangle|^2$, where $\langle i|$ and $|f\rangle$ are the initial and final quantum states of the conduction and valence bands, respectively. $\vec{\eta}$ is the polarization vector of light being $(sin\varphi, -cos\theta, 0)$ for TE polarization and $(-cos\theta cos\varphi, -cos\theta sin\varphi, sin\theta)$ for TM polarization. $\vec{p}$ is the momentum operator. The explicit optical matrix elements for the TE and TM polarizations are given by:

For the electron-heavy hole transition:

$$|\langle i|\vec{\eta}\vec{p}|f\rangle|^2 = \frac{\Pi_1^2}{2}\,(\text{TE}) \text{ and } |\langle i|\vec{\eta}\vec{p}|f\rangle|^2 = \frac{\Pi_1^2}{2}\cos^2\theta\,(\text{TM})$$

For the electron-light hole transition:

$$|\langle i|\vec{\eta}\vec{p}|f\rangle|^2 = \frac{\Pi_1^2}{6}\,(\text{TE}) \text{ and } |\langle i|\vec{\eta}\vec{p}|f\rangle|^2 = \frac{\Pi_1^2}{6}(\cos^2\theta + 4\sin^2\theta \pm sin\theta cos\theta cos\varphi)\,(\text{TM})$$

Where Π_1 is the constant power per unit solid angle at the source layer, φ is the azimuthal angle and θ the zenith angle.

The previous expressions are similar to the radiation of a horizontal dipole which therefore can correctly model electron-heavy hole transitions [4]. The expressions are only partially described by a combination of horizontal and vertical dipoles. However, the contribution of electron-light hole recombination can be neglected at low injections due to the nondegeneracy of the light hole band at the minimum of energy and to the considerably lower density of states of this energy band. The light emission in the quantum wells can thus be well described by a planar uniform distribution of horizontal dipoles placed in the same position as the quantum well closest to the *p*-GaN, which is the one that emits most of the light in GaN-based LEDs Figure 1-2a [5].

The angular emission was then propagated through the layers of the LED structure using the scattering matrix formalism Figure 1-2b. Complex refractive indices for all materials in the model were previously measured using variable angle spectroscopic ellipsometry. The output power P_{extrac} was calculated by integrating the angular emission inside the light cone (defined by the critical angle of total internal reflection θ_c) after correcting the power density Π for the change in solid angle caused by diffraction at the material interfaces Figure 1-2c. The extraction

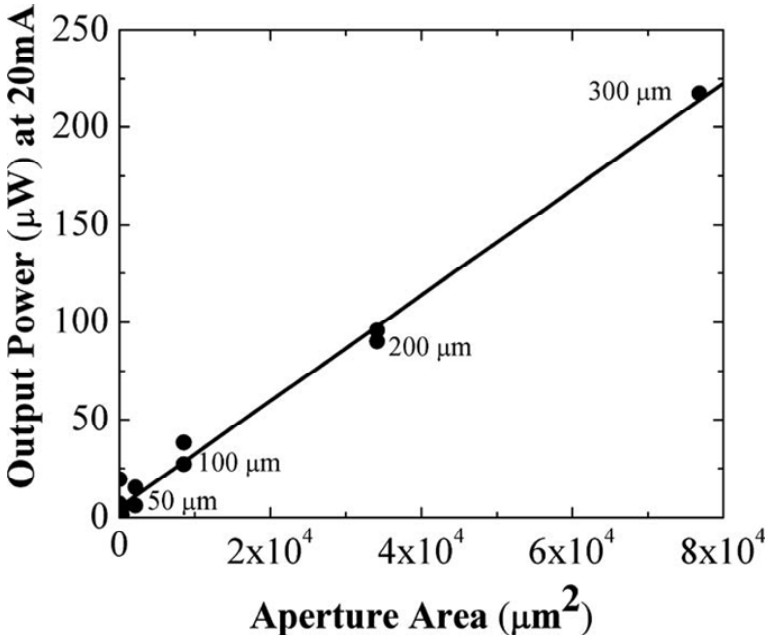

Figure 1-3 Power output for devices of varying aperture diameter

efficiency was then simply the ratio of the output power to the total emitted power:

$$\eta_{extraction} = P_{extracted}/P_{emitted} = \frac{\int_0^{\theta_c} 2\pi\Pi(\theta)\sin(\theta)d\theta}{\int_0^{\frac{\pi}{2}} 2\pi\Pi(\theta)\sin(\theta)d\theta}$$

Rotational symmetry and the uniform planar distribution of the dipoles allow us neglecting the effects of the aperture edge on the extraction.

For a particular testing LED we estimate $\eta_{extraction} = 3.03\ \%$ considering that the device has a smooth material to air interface. This value is much lower than the 4.1% given by the solid angle ratio (considering Π(θ) constant), due to the metal absorption of the semitransparent contacts. Total light output of the same device is then measured in an integrating sphere. We find that it varies linearly with aperture area Figure 1-3 which is indicates a uniform emission across the device surface (the latter is an assumption of the simulation). For this particular device we measure an output power per unit area of 2900 W/m^2 at an injection current density of 7.9 A/cm^2. This gives us a value for IQE of 0.43 at a current density of 7.9 A/cm^2.

Effect of surface roughness

In spite of the care of our approach, this value must be taken as a first crude EL measurement of the IQE. The model calculation assumes a flat surface, while the usual device material has a typical atomic force microscope measured surface roughness of about 10 nm (root mean squared). This roughness probably enhances the extraction efficiency of the device compared to the modeled structure and thus leads to an overestimate of the IQE. To check the

quality of the modeling and the impact of roughness, we compared simulated angular emission patterns from our model to patterns measured using variable-angle detection Figure 1-4. We observe an emission pattern with significantly washed out features compared to modeling. Adding a small amount of Lambertian emission to the calculated angular emission pattern allows it to match the measured pattern very well Figure 1-4. The latter proves the exactitude of the light extraction model, and points to an added extraction through surface roughness of about 30%. Including this extraction enhancement in the estimate of IQE however requires further detailed analysis that needs to be checked by comparing samples with varying surface roughness.

In conclusion, we have demonstrated a detailed method for the measurement of IQE based on electroluminescence. We believe this method will provide more accurate IQE values

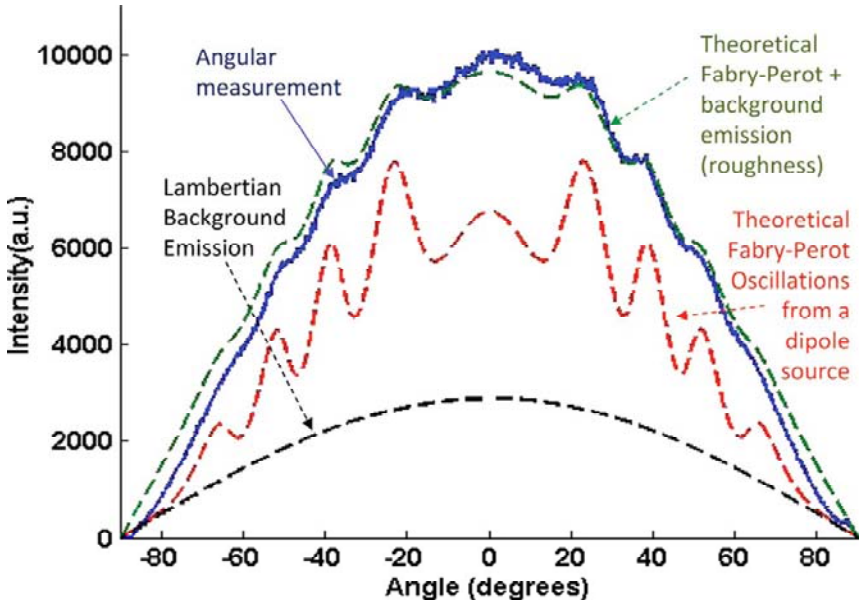

Figure 1-4 Measured and calculated angular emission patterns for the fabricated LED material with Ni/Au p-spreading layer. The idealized Fabry–Pérot emission pattern was produced from the simulations described here. A small amount of Lambertian background emission (30% of total emission) must be added to this to account for the surface roughness. The result is an emission pattern well matched to the measured profile.

for device analysis than the standard PL method currently employed, as the excitation of carriers and the band structure better reflect the conditions under which devices normally operate. This experiment will at least serve to corroborate the accuracy of the PL method. However, future improvements to the procedure, including improved modeling of extraction due to surface roughness, and alternate device geometries to eliminate the effect of roughness, need to be pursued. The device structure which limits collected light to photons coming directly from the quantum well can also be used for other applications, such as measuring the polarization of light emitted from a LED, and measuring the extraction enhancement provided by surface structuring such as by photonic crystal patterning.

1. Boroditsky, M., et al., *Surface recombination measurements on III--V candidate materials for nanostructure light-emitting diodes.* Journal of Applied Physics, 2000. **87**(7): p. 3497-3504.

2. Hangleiter, A., et al., *Towards understanding the emission efficiency of nitride quantum wells.* physica status solidi (a), 2004. **201**(12): p. 2808-2813.
3. Fuhrmann, D., et al., *Large internal quantum efficiency of In-free UV-emitting GaN/AlGaN quantum-well structures.* Applied Physics Letters, 2006. **88**(19): p. 191108-3.
4. Benisty, H., R. Stanley, and M. Mayer, *Method of source terms for dipole emission modification in modes of arbitrary planar structures.* J. Opt. Soc. Am. A, 1998. **15**(5): p. 1192-1201.
5. David, A., et al., *Carrier distribution in (0001)InGaN/GaN multiple quantum well light-emitting diodes.* Applied Physics Letters, 2008. **92**(5): p. 053502-3.

Appendix 2 - Modal tomography of photonic crystal LEDs: understanding device characteristics from analysis of dynamical diffraction of light

In this appendix, we present the analysis of the light extraction by PhCs in LEDs based on a 3D angle-spectrum-resolved measurement. The collection of the spectra for all the in-plane and out-of-plane angles(θ-φ angles) on 2D PhC LEDs yields detailed and precise information on the kinematic and dynamical diffraction properties, as well as, on the 2D diffraction symmetry of PhCs. The intimate analysis of the 3D modal diffraction of the PhCs at a broad spectral range yields complete information also on the device level, such as directional emission as well as enhancement on light extraction by the PhCs. Previous works have utilized such 3D angle-resolved measurements at a fixed wavelength, and the novelty of the present work lies on the inclusion of the spectral analysis.

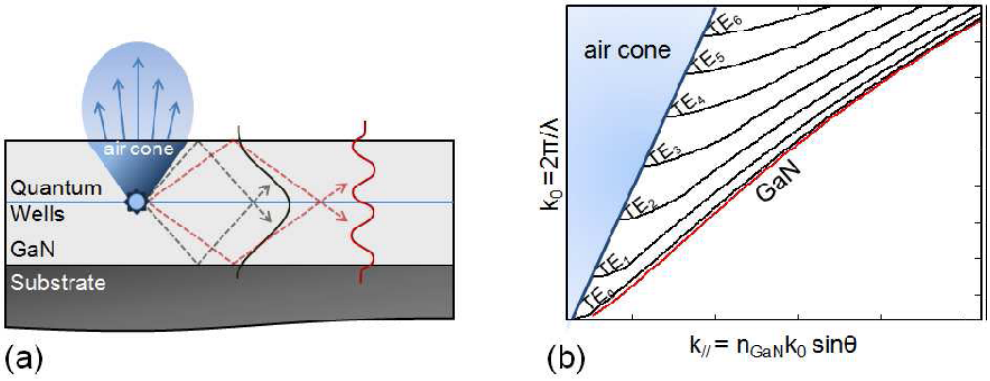

Figure 2-1 (a) Schematics of a simple planar LED showing the formation of the guided modes. (b) Dispersion relation of the guided modes in a planar LED structure.

The resolution in θ-φ angles and wavelength of the measurements presented in this work enables us to understand the interaction between the guided modes and the PhCs. Optimization of light extraction efficiency in such LEDs requires a structure design that enhances the interaction of the guided modes with the PhCs, that matches the PhC structure with vertical position and emission wavelength of the quantum-wells (QWs) in the LED, and a selection of the PhC parameters to ensure full guided light extraction and directional emission. All of these details can be revealed through the 3D spectrum-angle-resolved measurements and their representation.

Dynamical diffraction in 2D PhCs

In a simple planar LED, only a small fraction of the light created in the QWs is emitted to air. The remainder stays inside the structure as guided modes due to total internal reflections on the semiconductor/air interfaces (Figure 2-1a). In other words, an electromagnetic mode is guided in the LED structure when its in-plane wavevector is larger than the air wavevector (Figure 2-1b). A finite set of guided modes propagate inside the LED structure, each represented by a plane wave $\vec{E}^l(\vec{r}) = \vec{E}_o^l e^{i\vec{k}_l\vec{r}}$, where $\vec{k}_l = \overrightarrow{k_{\|_l}} + \overrightarrow{k_{z_l}}$ and l labels each mode (the index l will be abandoned in the remainder of the appendix for simplicity).

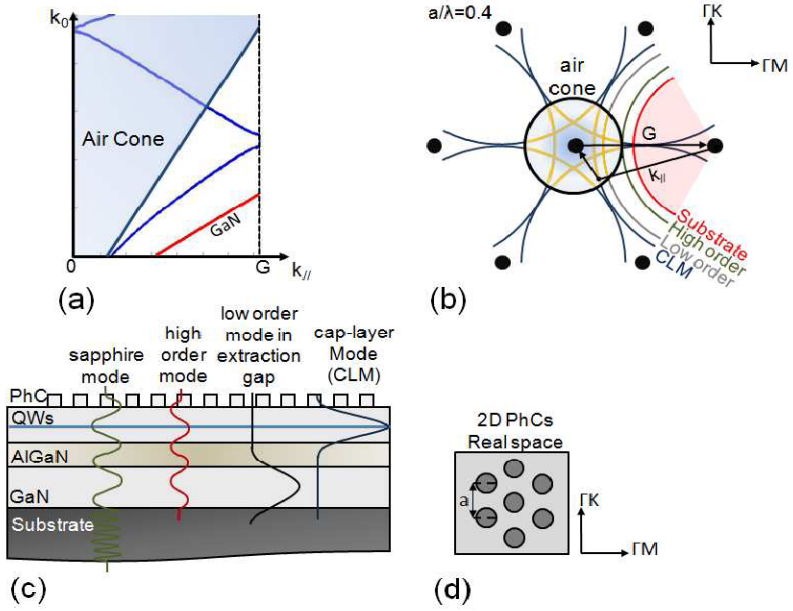

Figure 2-2 (a) Effect of 1D PhCs on the dispersion relation of a single guided mode. (b)Representation of the diffraction of guided modes, in the reciprocal space, by 2D PhCs. (c) Schematics of the LED structure used in the measurements. (d) Schematics of the top view of the photonic crystals in real space.

The PhC, introduced on the LED as a periodic spatial modulation of the index of refraction, acts as a diffraction grating for the guided modes. Thus it out-couples them into the air. The PhCs with a 2D triangular lattice of period ***a*** can be described in reciprocal space by the reciprocal vectors $\vec{G}_{n,m} = \left(n\vec{b}_1 + m\vec{b}_2\right)$ where $\vec{b}_1 = \frac{2\pi}{a}\left(1, -\frac{\sqrt{3}}{3}\right)$, $\vec{b}_2 = \frac{2\pi}{a}\left(0, \frac{2\sqrt{3}}{3}\right)$ and n, m are integers. The PhCs out-couples the guided modes by changing their in-plane wavevector $\vec{k}_{\|,G} = \vec{k}_{\|} + \vec{G}_{n,m}$. The guided modes, previously represented by their in-plane wavevector component $k_{\|}$ in a waveguide, acquire now an infinite set of harmonics $\vec{k}_{\|,G}$. The propagating modes, designated Bloch modes, are electromagnetic solutions of such periodic medium, and are represented by the sum of all the harmonics $\vec{E}(\vec{r}) = \sum_{\vec{G}} \vec{E}_{\vec{G}} e^{i\left(\vec{k}_{\|,\vec{G}}\,\vec{r}_{\|} + k_z z\right)}$, where $\vec{r}_{\|} = x\vec{e}_x + y\vec{e}_y$ and $\vec{k}_{\|} = k_x\vec{e}_x + k_y\vec{e}_y$ are the in-plane spatial vector and wavevector, respectively, and z and k_z are their out-of-plane components. The Bloch mode is diffracted to air (leading to leaky modes) when one of its harmonics is within the air cone, or in other words, satisfying the relationship $\left|\vec{k}_{\|,G}\right| < k_0$. The effect of a 1D PhC on the dispersion relation of the guided modes (Figure 2-1b), is depicted in Figure 2-2a for a single mode. The dispersion relation of the Bloch modes is periodic in k-space, and there is a spectral range in which the in-plane component of its wavevector satisfies the relationship $\left|\vec{k}_{\|,G}\right| < k_0$.

The in-plane diffraction of the guided modes by 2D PhCs is depicted in Figure 2-2b. The black dots represent the 2D reciprocal lattice of the PhCs. The black circle of radius k_0 corresponds to the in-plane projection of the air cone. Each guided mode, commonly labeled by its effective index $n_{eff} = \frac{k_{\|}}{k_0}$, is shown in this in-plane representation by a circle of radius $k_{\|} = n_{eff}k_0$ (blue, grey, green circles) and in red is the sapphire circle (radius $n_{sapphire}k_0$). The schematics of each group of modes supported by the structure measured in this example are shown on Fig.2c. As it is explained next section, the GaN-based LED structure contained an

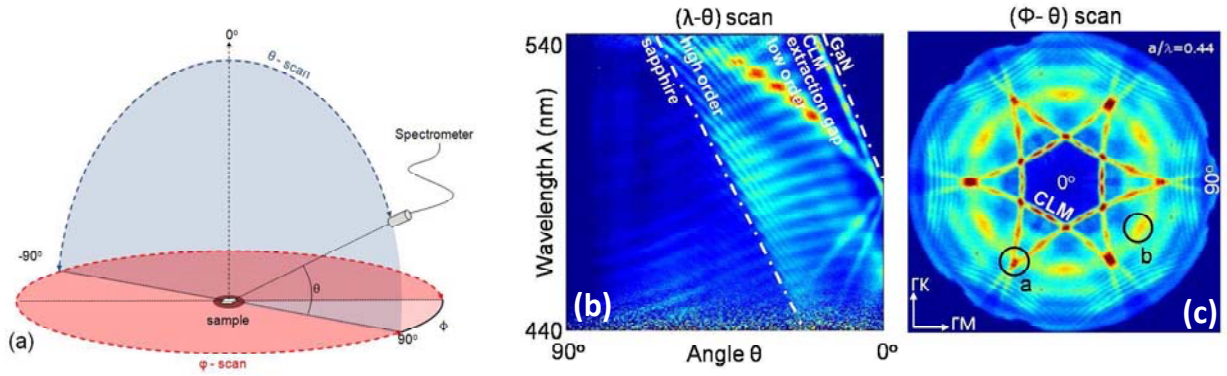

Figure 2-3 (a) Schematics of the 3D angular measurement where ϕ is the in-plane angle and θ the out-of-plane. Example of (b)λ − θ scan and (c) ϕ − θ scan measurements at a fixed λ

embedded layer of lower index of refraction (AlGaN) that confines a low order mode in the GaN cap-layer, called the cap-layer mode (CLM), represented by the blue mode in Figure 2-2c. This structure also supports low order modes in the GaN layer below the AlGaN which are neither well excited by the QWs, nor well extracted by the PhCs, represented by the black mode in Figure 2-2c. It supports two other families of guided modes, the high order modes guided in the GaN layer and the sapphire modes (red and green modes respectively in Figure 2-2c), extending over the entire LED structure, mostly in the sapphire substrate due to its much larger thickness compared to the GaN layer.

The condition $\left|\vec{k}_{\parallel,G}\right| < k_0$ is satisfied when the modes enter the air cone, represented in yellow for the CLM and a low order mode in Fig.2b. These harmonics radiate to air, which introduces an imaginary component k'' to the Bloch mode wavevector. The energy of this leaky mode decreases exponentially as it propagates in the structure from the emission point as $I = \left|\vec{E}(\vec{r})\right|^2 = |\vec{E}_0|^2 e^{-2k''r_\parallel}$ due to diffraction to air by the PhCs and an extraction length can be defined as $L_{extraction} = \frac{1}{2k''}$.

This exponentially decreasing intensity in real space corresponds to a Lorentzian function in k-space, which is seen from a simple Fourier transformation $\mathcal{F}[I\,](k) = \frac{4k''\left|\vec{E}_0\right|^2}{4k''^2 + k^2}$ whose full width at half maximum (FWHM), equal to $4k''$. The FWHM of the Lorentzian corresponding to the extracted modes by the PhCs is related to the extraction length as $FWHM = \frac{2}{L_{extraction}}$ Therefore, the FWHM of a diffracted mode reveals the efficiency of the PhC in extracting this guided mode and the diffracted band in reciprocal space corresponding to this guided modes is thick for short extraction length.

The far field emission of the LED, being related to the Fourier transformation of the light diffracted by the PhCs, is a direct measurement of the modal diffraction in reciprocal space. Therefore, the measurement of the far field emission of PhC LEDs reveals the diffraction of the guided modes in reciprocal space. Additionally, the measurement of the FWHM of the diffracted modes allows us to assess its extraction length, which reveals how well this mode is extracted by the PhCs (see Appendix 3). In this example, we present a 3D angle-spectrum-resolved measurement of the far field emission of LEDs which allows for the complete measurement of the 2D diffraction of PhCs including extraction and absorption mechanisms inside the LED

through the FWHM of each guided mode. A complete understanding of the LED in the device level is possible from the intimate knowledge of the modal behavior.

Experiment description

The GaN-based LEDs measured here were grown by metal-organic chemical vapor deposition (MOCVD) on a sapphire substrate. The LED structure consists of a ~ 3μm-thick n-GaN followed by a 650 nm-thick $Al_{0.16}Ga_{0.84}N$ confining layer and a 550 nm-thick active region comprised of a n-GaN layer, 6x-InGaN QWs emitting at λ = 465 nm and a p-GaN layer (Figure 2-2b). The $Al_{0.16}Ga_{0.84}N$ confines a low order mode in the cap-layer, increasing this mode's interaction with both the PhCs and the QWs. The 150 nm-deep PhC with triangular lattice was patterned on the LED top surface with period of 224 and 248 nm (Figure 2-2d). The device size was 800x800 μm^2 and the current was injected through a circular p-contact (diameter of 100 μm) in the center of the device to separate the metal absorption from the PhC extraction of the guided modes. The 3D angle-spectrum-resolved measurement is based on the collection of the spectra for all the in-plane (φ) and out-of-plane (θ) angles over the entire semi-sphere. The far-field emission from the sample was collected by a optical fiber placed on a 15 cm-radius rotating arm after a proper selection of the TE or TM modes by a polarizer placed in front of the optical fiber. The measured spectra were sent through the optical fiber to a spectrometer (Triax 550- Horiba Jobin-Yvon) with a 0.2 mm entrance slit and a 300 g/mm diffraction grating, which offers a high spectral range for the measurement (Δλ ~ 100 nm). For each value of in-plane angle φ, a complete out-of-plane measurement was performed for θ varying from -90° to 90°, with a 0.5° step. The φ angles were scanned from 0° to 60° which was more than enough to measure all the necessary in- plane data due to the 30°-symmetry of the 2D PhCs. The schematic of the rotating setup is shown in Figure 2-3.

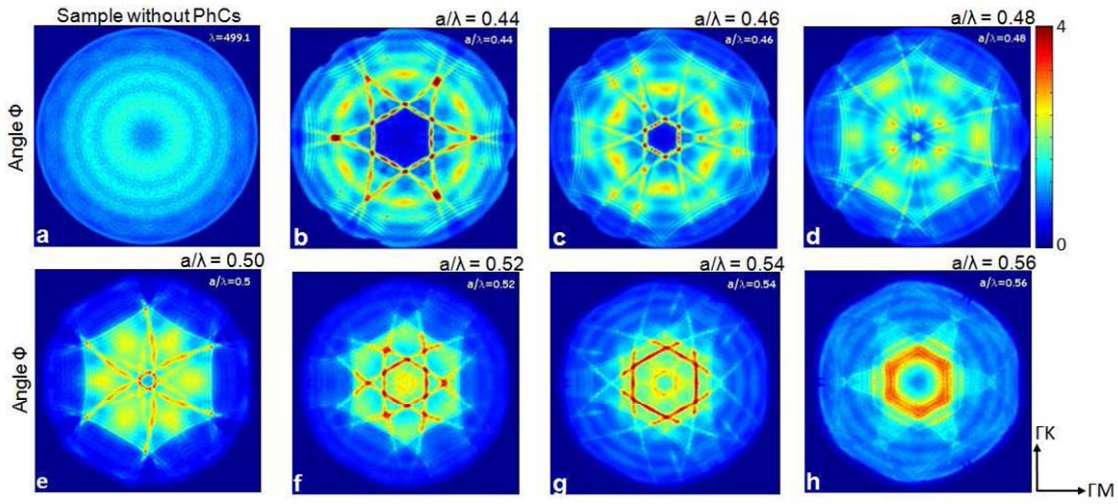

Figure 2-4 Experimental representation of the ϕ − θ diffraction of guided modes by 2D PhCs for different wavelengths.

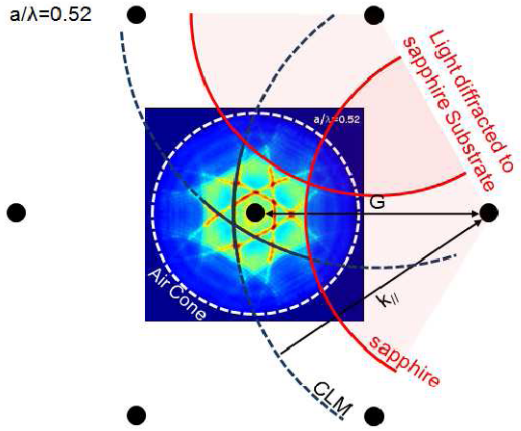

Figure 2-5 Combination of the ϕ − θ scan with the simulation of the 2D PhC diffraction represented in the reciprocal space for a/λ = 0.52.

Results and discussion

The λ − θ and φ − θ scans from the 3D angular setup are shown in Fig. 3b,c, respectively. The sharp lines in these measurements correspond to the extracted guided modes by the PhCs. The out-of-plane angle-resolved measurement (Fig. 3b) reveals the diffraction of all the guided modes. The modes guided in the GaN slab over the substrate have effective indexes of refraction between the GaN (n_{GaN}) and sapphire ($n_{sapphire}$) indexes. The first mode observed near the GaN line, which is also the brightest among all measured modes, is the CLM mode, represented in blue in Figure 2-2c. The extraction gap observed between the CLM and the next diffracted mode corresponds to the modes guided in the GaN layer below the $Al_{0.16}Ga_{0.84}N$, which are neither well excited by the QWs nor extracted by the PhCs (black mode in Figure 2-2c). Additionally, two other family of modes are observed in the λ − θ scan, the low and high order modes guided in the GaN slab, represented in Figure 2-2c. The modes originally guided in the sapphire slab are not seen in this measurement: they extend over the entire ~500 µm-sapphire slab, which is much thicker than the ~4 µm-thick GaN, hence their overlap with the PhCs is weak, or in other words, they also are not extracted by the PhCs. For this same reason, each sapphire mode is also much less excited by the QWs than the GaN modes. Although the energy carried per mode is small, due to the large number of sapphire modes, the total fraction of optical energy guided in the sapphire layer is considerable high (~22%). The φ − θ scan shows the diffraction of modes in different directions of symmetry of the PhCs, ΓM and ΓK. It also presents the emission of the LED for the out-of-plane θ angles from 90° to 0°. The φ − θ scan allows us measuring the interaction and coupling between different guided modes from different in-plane directions, seen for example in point a in Figure 2-3c. In the case shown in point ***a*** of Figure 2-3c, the higher intensity in the intersection of the CLMs diffracted from different directions of the PhC comes from a simple superposition of the diffracted bands, and no coupling between these modes is observed. In case of coupling, a better light diffraction would be observed, leading to a higher imaginary component of the wavevector k'' and thus a smaller FWHM at the intersection point. This measurement also shows the interaction between guided modes and Fabry-Perot modes seen in point ***b*** in Figure 2-3c.

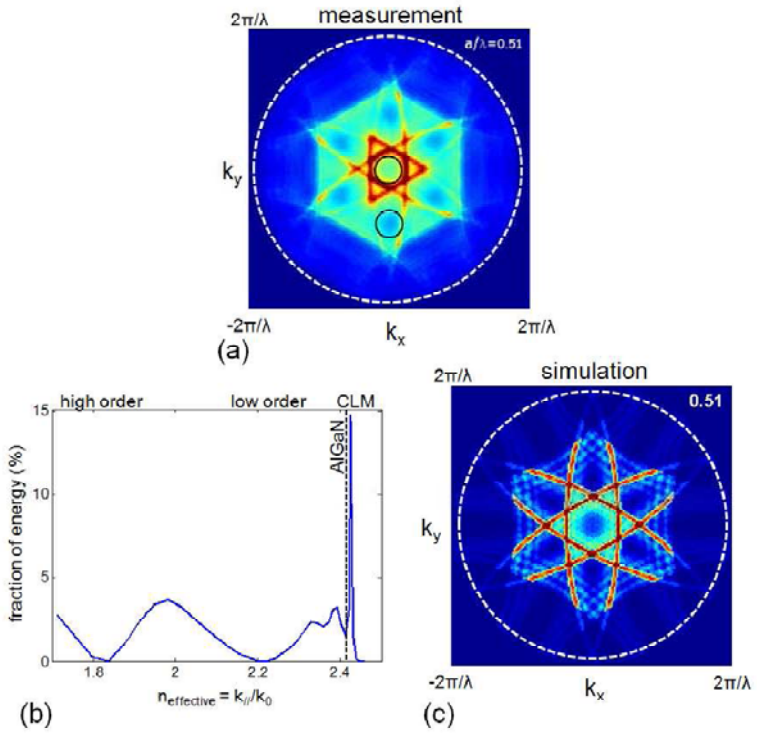

Figure 2-6 (a $\phi - \theta$ scan from the 2D PhC LED for $a/\lambda = 0.51$. (b) Simulated fraction of energy emitted into each guide mode by the QWs. (c) Simulation of the diffraction of the guided modes by the PhCs combining the position of the diffracted modes due to the 2D PhCs and the fraction of energy received from the QWs.

The variation of the $\varphi - \theta$ diffraction with wavelength is shown on the snapshots in Figure 2-4. The effect of the PhCs on the diffraction of the guided modes can be clearly seen by comparing the $\varphi - \theta$ scans of samples with and without PhCs (from the same wafer). The $\varphi - \theta$ scans of the device without PhCs (shown in Figure 2-4a) reveals only the Fabry-Perot modes coming from the interference of the direct emitted light on the interfaces of GaN with air and sapphire. The measurements of Figure 2-4 b-h show, in addition to the Fabry-Perot modulations, the sharp arc of circles corresponding to the diffracted guided modes by the PhCs. Figure 2-4b-d correspond to the results of the 224 nm-period PhC sample and Figure 2-4 e-h correspond to the 248 nm-period PhC. All of the measurements are on the same color scale and it is worth noticing the higher intensity in the measurements of the PhC samples compared to the non PhC ones, indicating their higher light emission. To compare the results of both PhC samples (periodicity of 224 nm and 248 nm), the wavelength was normalized by the PhC period ***a***.

To better understand all the features in these measurements, Fig. 5 combines the $\varphi - \theta$ scan with a similar simulation of the PhC diffraction shown in Figure 2-2b, both at $a/\lambda = 0.52$. The blue dotted circle in Figure 2-5 matches well the measured diffracted CLM. It correspond to $k_{\parallel} = \frac{2\pi n_{effective}}{\lambda}$, where $n_{effective}$ is the calculated value of the effective index of the CLM at this wavelength. All the less intense modes falling in between the CLM and the sapphire (red) circles correspond to the diffraction of all the other modes. Notice that no modes are seen below the sapphire circle, which is partially due, as explained previously, to the much lower QW excitation and PhC extraction of these modes. However, the intensities of all modes beyond this circle are quite reduced, which corresponds to the diffraction to sapphire of modes originally guided in the GaN slab and this can be seen as a loss since these modes can no longer be fully extracted to air.

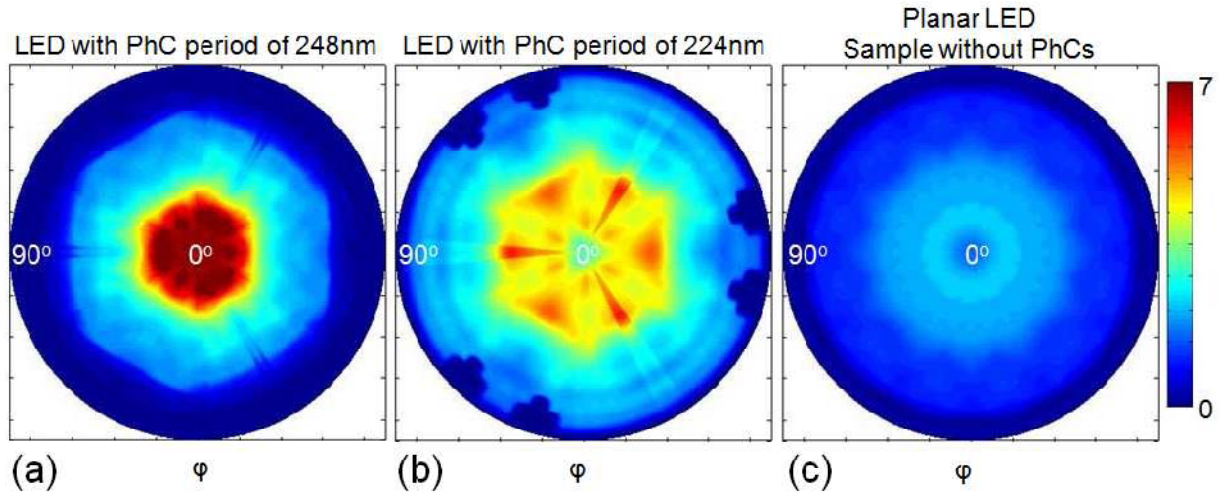

Figure 2-7 (a) Schematics of the 3D angular measurement where ϕ is the in-plane angle and θ the out-of-plane. (b) Schematics of the LED structure used in the measurements. (c) Schematics of the top view of the photonic crystals.

The PhCs diffract guided modes to air or to sapphire depending on the a/λ ratio, and a proper design of the PhCs is required to avoid the losses to the substrate.

Let us go back to the results in Fig. 4: For a/λ = 0.44 (Figure 2-4b), no loss to sapphire is observed, however the extraction of guided modes does not occur in the vertical direction, as would be desirable. As the a/λ ratio increases, the guided modes are extracted more vertically, increasing the directional emission of the device, but also increasing the sapphire loss (for θ close to 90°). The emission of the PhC LED is more vertical for a/λ = 0.52 when the middle order modes ($n_{effective} \sim 2.1$) diffracted from all the different PhC reciprocal points intercept each other in the center of this measurement, which implies that both the low and high order modes are also diffracted in the vertical direction. The high directionality of PhC LEDs with sapphire substrates is due to the sapphire loss of the diffracted modes at higher angles. The losses to sapphire are more pronounced at a/λ = 0.56, where even the CLM is diffracted to the substrate. The information from the snapshots shown in Figure 2-4 is better presented in the form of a video that shows the evolution of the diffracted modes as the wavelength varies (supplementary information). It presents an experimental observation of the Ewald's representation of the in-plane 2D diffraction of PhCs, revealing the dynamical interaction of different modes. Some other interesting features can be seen in the φ − θ scan of Figure 2-6a at a/λ = 0.51. While the intensity of the lines corresponding to the CLM is the most pronounced in this measurement, other regions have very low intensities, as indicated by the black circles (plus its symmetric positions). The intensity in these regions is determined by the modal excitation by the QWs. As explained previously, the intense CLM lines in this plot is due to the higher overlap this mode with the QWs. Similarly, the modes overlap differently the QWs and thus, are differently excited. Fig. 6b shows the simulated fraction of energy emitted into each guided mode, represented by its $n_{effective}$. This result is based on a simulation of the angular light emission by the QWs inside the LED, from a dipole method [1]. The fraction of energy of each mode was calculated from the area of the peak corresponding to the guided modes. Although the structure contains 6x-QWs, we considered in this simulation just a single emitting QW, placed on the interface between the first QW and the p-type GaN [2].The fraction of energy of the modes varies almost smoothly from the high order to the low order modes, which can be simply understood from their smooth change in overlap with the QWs. Some modes do not receive any energy from the QWs, corresponding to a null overlap with the QW (only because just one QW was considered in this

simulation). The peak after the AlGaN line (black dotted line) corresponds to the CLM, which, as indicated previously, is the most excited mode of all. The FWHM of the diffracted modes is inversely proportional to their extraction length, as explained in Section II, which determines the thickness of the diffracted bands in the φ−θ scan (or the FWHM of the Lorentzian corresponding to each guided mode). Figure 2-6c presents a simulation of the diffraction of the guided modes by the 2D PhCs combining the position of the diffracted modes (Section II) with the fraction of energy that they receive from the QWs. The non-zero linewidth of the modes in this simulation comes from their extraction length as $FWHM = \frac{2}{L_{extraction}}$. Notice that the simulated diffracted modes present a very good match with the experiment. In addition, the regions of lower intensity shown in Figure 2-6a are also observed in the simulation. These regions correspond to the overlap of a poorly excited group of modes, diffracted from different reciprocal space points of the PhCs.

The directional emission of the device can be assessed by integrating in wavelength the θ − φ measurements. Figure 2-7 a-c shows the integrated in-plane emission of the LEDs with 224 nm, 248 nm-period and without PhCs, respectively. Both samples with PhCs have an improved emission compared to the non PhC sample. The directional emission is the highest for the 248 nm-PhC sample, but some of the light emitted at angles close to 90° was lost into the sapphire substrate. The least amount of light lost in the sapphire substrate was for the 224 nm-PhC sample, however in this case, the light emission was concentrated at $\theta \sim 25^{o}$. The integrated emission of the three different LEDs, shown in Figure 2-7, as a function of the out-of-plane angle for both directions of symmetry of the PhCs (ΓM and ΓK) is presented in Figure 2-8a. It is clearly seen the directional emission from the 248 nm-PhC sample and the enhancement on light extraction when compared to the non PhC device. Figure 2-8b shows the integrated emission as a function of the in-plane angle φ for the 248 nm-PhC and the non-PhC samples. While the emission from the non-PhC sample is isotropic, the PhCs show anisotropy in their in-plane light emission with a higher emission along the ΓK direction of the PhCs, revealing their slightly better extraction along this direction.

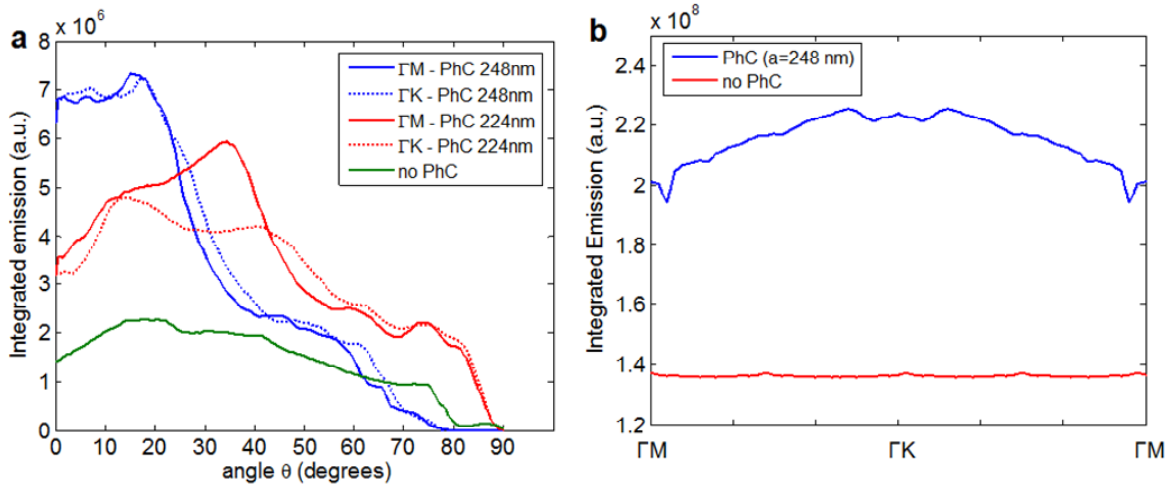

Figure 2-8 (a)Integrated emission of the three different LEDs as a function of the out-of-plane angle for both directions of symmetry of the PhCs. (b)Integrated emission as a function of the in-plane angle ϕ for the 248 nm-PhC and the non-PhC samples.

In conclusion, the 3D analysis of the dynamical diffraction of 2D PhCs allows us a more profound understanding of the interaction of all guided modes with the PhCs, among themselves and the Fabry-Perot modes. This method allows us to identify well and poorly extracted modes by the PhCs and intimately optimize the vertical dimensions of the LED structure by designing a structure that enhances the interaction of the guided modes with the PhCs, that matches the PhC structure with vertical position and emission wavelength of the quantum-wells (QWs) in the LED, and a selection of the PhC parameters to ensure full guided light extraction and directional emission. The integration of the data for all wavelengths yields a global behavior of the devices, more clearly revealing their directional out-of-plane as well as isotropic in-plane emission.

1. Benisty, H., R. Stanley, and M. Mayer, *Method of source terms for dipole emission modification in modes of arbitrary planar structures.* J. Opt. Soc. Am. A, 1998. **15**(5): p. 1192-1201.
2. David, A., et al., *Carrier distribution in (0001)InGaN/GaN multiple quantum well light-emitting diodes.* Applied Physics Letters, 2008. **92**(5): p. 053502-3.

Appendix 3 - Measurement and analysis of the guided modes extinction length and its relation to the photonic crystal extraction length

Achieving high light-extraction efficiencies requires a LED structure design that optimizes the interaction of the guided modes with the PhCs through an appropriate selection of both the vertical and in-plane device parameters such as layer thicknesses, PhC depth, quantum well position, PhC period and fill factor *etc.*. Such structure should characterize with a guided modes light extraction length that is shorter than any dissipation length. Here, the latter is a parameter that quantifies the effect of competitive light loss mechanisms such as active layer re-absorption, dissipation losses from contacting materials *etc.*. PhC-LED optimization has relied so far on simulations of PhC extraction length and on some modeling of the losses [1-3]. The PhC enhancement in light extraction is commonly assessed by output power measurements, which only reveal the global effect of the PhCs on the total light extraction of the guided inside the LED light. Here, experimental determination of the PhC light extraction length as well as the characteristic length of the other dissipation processes is important to reveal the competition between beneficial (PhC extraction) and detrimental (QW re-absorption, contacts absorption etc.) extinction of the guided modes.

Here, we resume an experimental technique that to obtain the extinction lengths of the guided modes. This method is further enhanced to separately determine the light extraction length due to the PhC interaction and the optical re-absorption of QWs. In addition we the variation of these parameters with photon energy can be measured.

PhC light extraction length – theoretical considerations

As we know, an extended source emitting light inside a semiconductor slab excites a finite set of guided modes that propagate at well defined discrete angles with the waveguide interface (Figure 3-1a). The dispersion relation of these guided modes inside the waveguide (Figure 3-1b) implies that, for a given wavelength, only a finite set of modes is supported by the waveguide.

Considering a diffracting grating (or PhC) on the surface of this waveguide, each guided

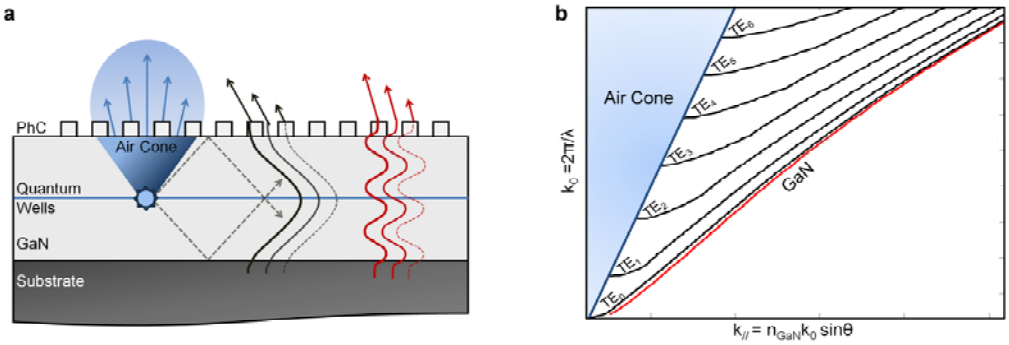

Figure 3-1 (a) Schematics of a simple planar LED showing the formation of the guided modes. (b) Dispersion relation of the guided modes in a planar LED structure.

mode will be diffracted out of the waveguide at a well defined angle. Thus, each diffracted guided mode will act as a separate monochromatic source sampling of the PhC. Here, one can show that there is an analytical relation between the mode linewidth and the distance where the guided mode interacts with the PhC. That distance is defined as the mode extraction (extinction) length and it can be used to analyze the effectiveness of guide mode coupling to the PhC and its competition with the different dissipative process that also appear in a real structure.

In a simple planar structure with embedded QWs, such as planar LEDs, only the small fraction of the QW luminescence that falls within the air cone is directly emitted into the air (Figure 3-1a). The rest stays inside the structure as guided modes confined in the structure due to total internal reflection on the semiconductor/air interfaces. Those modes are characterized with in-plane wavevectors that are larger than the air wavevector (Figure 3-1b). The guided light propagating inside the LED structure can be decomposed as a finite set of guided modes, each represented by a plane wave $\vec{E}^n(\vec{r}) = \vec{E}_0^n e^{i\vec{k}_n\vec{r}}$, where $\vec{k}_n = \vec{k}_{\|_n} + \vec{k}_{z_n}$ and n labels each mode (the index n will be abandoned in the remainder of the paper for simplicity). The spatial modulation of index of refraction in real space of the PhCs, described in reciprocal space by a reciprocal vector $\vec{G}$, out-couples the guided modes by changing their in-plane wavevector as $\vec{k}_{\|,m} = \vec{k}_{\|} + m\vec{G}$, where m is an integer. The infinite set of harmonics diffracted by the PhCs form a single mode (Bloch mode) which is an electromagnetic solution of this periodic medium and is represented by $\vec{E}(\vec{r}) = \sum_m E_m e^{i(\vec{k}_{\|,m}\vec{r}_{\|}+k_z z)}$, where $\vec{r}_{\|} = x\vec{e}_x + y\vec{e}_y$ and $\vec{k}_{\|} = k_x\vec{e}_x + k_y\vec{e}_y$ are the in-plane spatial vector and wavevector, respectively, and z and k_z are their out-of-plane components. The diffracted in-plane harmonics that fall inside the air cone (in other words, satisfying the relationship $|\vec{k}_{\|,m}| < k_0$) radiate to air and introduce an imaginary component to the Bloch mode wavevector k". The energy of such leaky mode decreases exponentially as it propagates in the structure from the emission point as $I = |\vec{E}(\vec{r})|^2 = |\vec{E}_0|^2 e^{-2k"r_{\|}}$ due to diffraction to air by the PhCs [2]. The extraction length for each guided mode then can be defined as:

$$L_{extraction} = \frac{1}{2\,k''}$$

The effect of an exponentially decreasing intensity in real space ($r_{\|}$) can be studied in reciprocal space by its the correspondent conjugate variable k, obtained by a Fourier transformation:

$$\mathcal{F}[I](k) = \frac{4k''|\vec{E}_0|^2}{4k''^2 + k^2}$$

This function is Lorentian and its full width at half maximum (FWHM), designated here Δ_{kk}, is equal to $4k''$ and can be related to $L_{extraction}$ as:

$$FWHM = \Delta_{kk} = \frac{2}{L_{extraction}}$$

The extraction length of all guided modes than can be determined from the measurement of Δ_{kk}. The latter is assessed from far-field emission pattern of the studied LED.

For real structure one should consider all other scattering and dissipation processes. Their effect could be easily accounted for by adding a corresponding term in the expression for the wavevector imaginary part.

$$k'' = k''_{scattering} + k''_{absorption} + k''_{PhC\ extraction}$$

Where the terms $k''_{scattering}$, $k''_{absorption}$, and $k''_{PhC\ extraction}$ denote the imaginary wavevector components of the scattering, absorption and extraction, respectively. Thus, the measured decay length should now be referred as an extinction length:

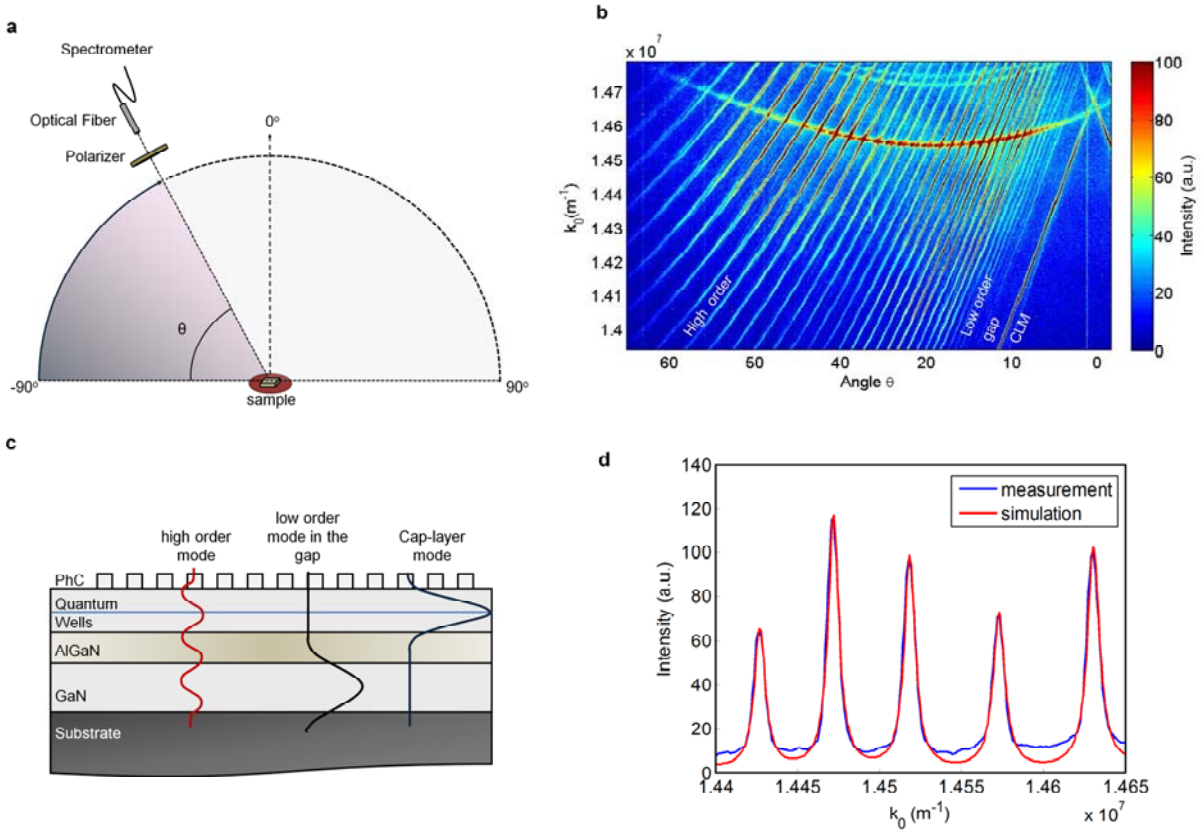

Figure 3-2 Angle-resolved measurements. (a) Schematics of the set-up. (b) High-resolution angle-resolved measurement where the wavelength λ was converted into $k_0 = 2\pi/\lambda$. The sharp lines correspond to the extracted guided modes by the PhCs. (c) Schematics of the side-view of the PhC LED structure along with the guided modes supported: Cap-layer mode (blue), low order mode in the gap (black) and a high order mode (red). (d) Cross-section of the angle-resolved measurement at a given angle (blue) along with the theoretical Lorentzian-shaped fit (red).

$$L_{extinction} = 1/2\left(k''_{scattering} + k''_{absorption} + k''_{PhC\ extraction}\right)$$

A model to decouple the contributions of the absorption and PhC extraction will be introduced in one of the following subsections.

PhC light extraction length – measurement

The measurement of the extracted guided modes in the reciprocal space is done by high-resolution angle-resolved electroluminescence. The spectrum of the LED under electric bias is measured for all angles θ from -90^o to 90^o. Here, the far-field emission from the sample is collected by a 100 μm clear aperture optical fiber placed on a 21 cm long rotating arm. The proper selection of the TE or TM modes is assured by a polarizer placed immediately in front of the optical fiber. No lenses are used to increase the fiber collection angle as this is detrimental to the set-up angular resolution. The luminescence is then analyzed in a single diffraction grating (here 1800 g/mm) spectrometer (Triax 550 – Horiba Jobin-Yvon). The entrance slit opening is varied between 0.1 mm and 0.2 mm in, compromising either the signal intensity or the setup

spectral resolution, respectively. For clarity, a schematic of the rotating setup is shown in Fig. 2a. The luminescence spectra for all angles are collected and then stacked to produce a dispersion maps similar to that in Figure 3-2b. For convenience, a proper conversion of axis is chosen, following the relation $(\theta, \lambda) \longrightarrow (k_{\parallel}, m = k_0 sin(\theta), k_0)$. Here, $k_{\parallel}, m$ is the parallel component of the diffracted wavevector and $k_0 = \frac{2\pi}{\lambda}$. Each mode can be labeled by its effective index of refraction $n_{eff} = \frac{k_{\parallel}}{k_0}$ and its extraction length can be obtained from a measurement of its FWHM using equation (2).

Here, we present an example of an angle-resolved measurement (Figure 3-2b) along the ΓK direction of the test LED structure. The latter consisted of a ~3 μm thick GaN template followed by a 650 nm-thick $Al_{0.16}Ga_{0.84}N$ confining layer and a 550 nm thick active region comprised GaN pn junction and a set of six InGaN QWs emitting at λ = 445 nm (Figure 3-2c). A 95 nm deep PhC with triangular lattice and 28% fill factor was patterned on the LED top surface. The lattice period is chosen to be 200 nm. The device size was 800x800 μm^2 and the current was

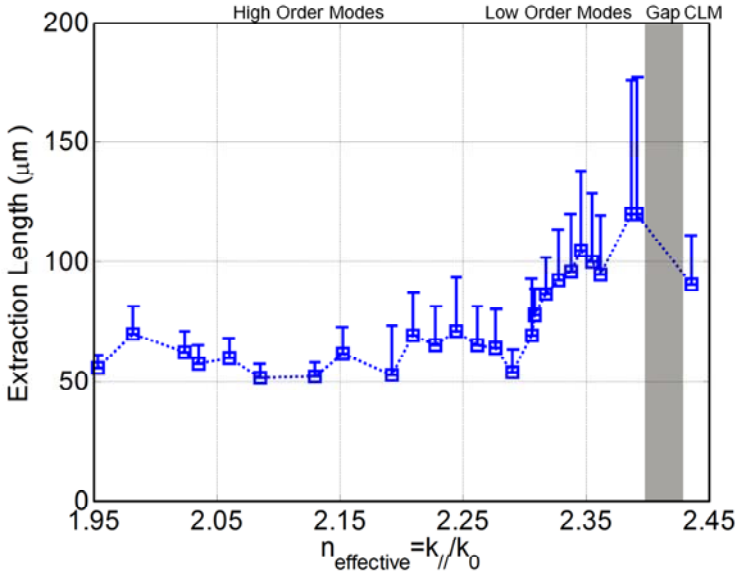

Figure 3-3 Extraction length $L_{extraction}$ as a function of the effective index of the guided modes.

injected through a circular *p*-contact (diameter of 100μm) in the center of the device to separate the metal absorption from the PhC extraction of the guided modes. The dispersion map of the electroluminescence corresponding to the device described above is presented in Figure 3-2b. Here, the sharp oblique lines correspond to the PhC extraction of modes guided in the LED structure (guided modes represented in Figure 3-2c). It is important to note that the $Al_{0.16}Ga_{0.84}N$ layer confines one low order mode in the top layer. This mode has a high interaction with both the PhCs and the QWs [1]. This mode is referred to as cap-layer mode (CLM). The gap between the extracted modes and the CLM in Fig. 2b corresponds to the low order modes guided in the GaN layer below the AlGaN confining layer. Those are neither well excited by the QWs nor extracted by the PhCs. The modes diffracted at higher angles have higher mode order.

The precision on the measurement $\Delta k_{\parallel}$ depends largely on the angular resolution of the setup. In the present case, the collection solid angle of the optical fiber, determined by its 100 μm aperture placer at a distance of 21 cm to the sample, limits the angular resolution of the setup to $\Delta\theta \approx 0.027°$ (see also the supplementary discussion on the setup precision at the end of this

text). To overcome the limited angular resolution of this setup, one can take advantage of the higher spectral resolution and measure the FWHM of the modes intensity peak along k_0 (denoted as Δk_0). The latter can be converted to $\Delta k_{\parallel}$ using the dispersion relation of the guided modes $\Delta k_{\parallel} = n_{eff}\Delta k_0$. Thus, the modified expression of the extraction length is:

$$L_{extraction} = \frac{2}{n_{eff}\Delta k_0}$$

A vertical cut (the electroluminescence for a given angle) of the dispersion is shown in Fig. 2d. Here, the experimental curve (blue line) is compared to the Lorentzian fit as predicted by

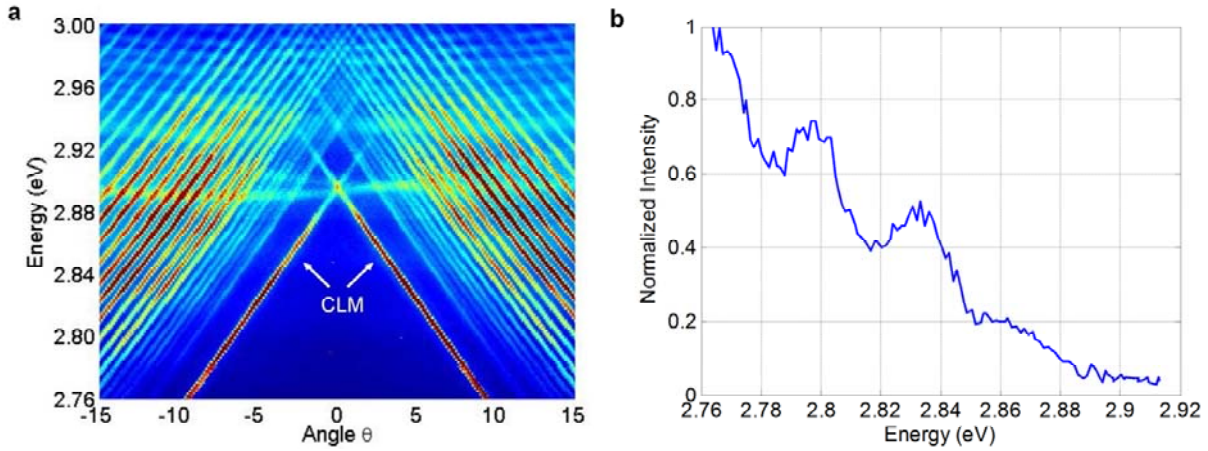

Figure 3-4 Absorption of the CLM. (a) Low resolution angle-resolved measurement converted into photon energy versus angle showing that the CLM disappears for energies above 2.93 eV. (b) Normalized intensity of the CLM as a function of the photon energy. The oscillations are from Fabry-Perot interference that modulate the intensity of the CLM.

equation (1) (red line). For all the modes at $k_0 = 1.43x10^7 m^{-1}$ the values of Δk_0 are measured and converted into such for the mode extraction length ($L_{extraction}$) according to equation (3). The results are presented in (Figure 3-3). The error bars in Figure 3-3 denote an estimation of the underestimation of the extraction length due to the broadening of the measured luminescence peaks due to the finite angular aperture of the optical fiber. In conclusion we should not that the measured extraction length of the modes varies between 55-120 μm and matches our theoretical predictions.

Measurement of the quantum well absorption

The described above procedure can be further extended to allow determining the material absorption inside the active region. The technique is based on the analysis of the two competing extinction mechanism for the cap layer guided mode (CLM), namely the material absorption and extraction trough the PhC. The choice of the use of the CLM over all other modes is mostly evident. In fact the introduction of thick low refraction index AlGaN confining layer in the LED structure confines very strongly the lowest order mode in the active region. Consequently this top (cap) layer mode (CLM) will have much higher overlap with the QWs than that of any other mode, thus making it the most suitable to study the QW absorption. A simple calculation of the overlap of the guided modes with the QWs shows that the confinement factor Γ of the CLM is at least eight times higher than that of any other mode (Γ_{CLM} ~ 4 %). Another condition for the success of the presented technique is to render the PhC less effective. Thus, the surface PhCs in the current test structure will be intentionally shallowly etched (95 nm deep) to yield a “poor” extraction length, so that the QW reabsorption competes effectively with the PhC extraction. We

will also benefit on the large InGaN QW spectral linewidth ($\Delta\lambda \sim 20\,nm$) so that the CLM can probe the variation of the QW reabsorption as a function of the photon energy.

The angular resolved measurements (low resolution) of the electroluminesnce spectra of our test structure are presented in Figure 3-4. One can see that the CLM completely disappears above 2.93 eV while all the other modes can still be observed. The absorption of the CLM can also be more clearly observed in Figure 3-4b where we show a plot of its intensity as a function of the photon energy. The intensity profile is first normalized by its value at 2.76 eV, where the absorption was assumed to be negligible. The spectrum line is then subsequently normalized by the lineshape of the QW emission in this energy range. As seen the intensity of the CLM decreases for higher energies and eventually reaches zero at 2.92 eV. The wavy modulations observed in the CLM intensity come from Fabry-Perot interference in the cavity formed by the

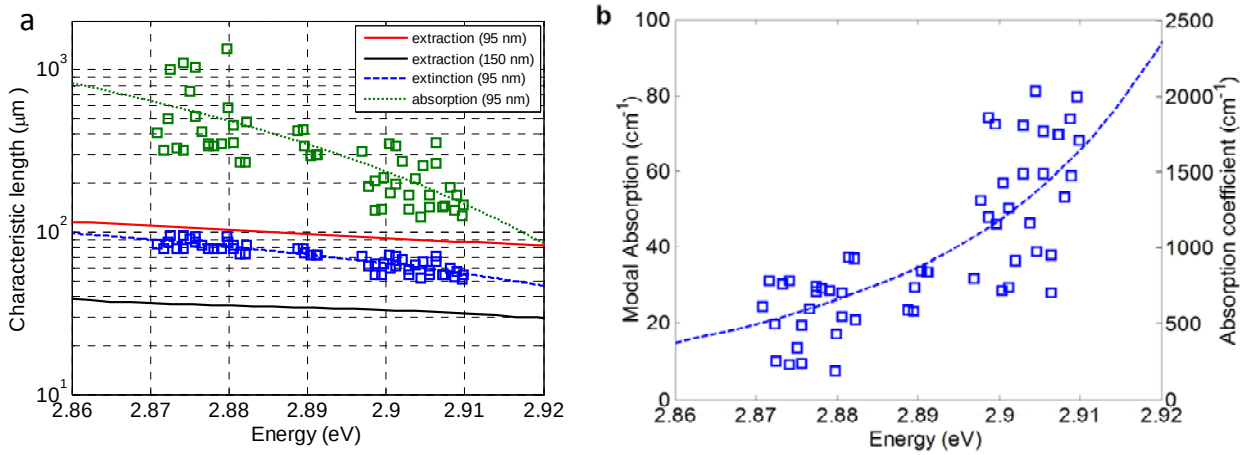

Figure 3-5 (a) Dependence of the extinction (blue curve), extraction (red curve) and absorption (green curve) lengths of the CLM on energy. The black curve is the CLM extraction length for a 150 nm-deep PhC, which has a better extraction than the 95 nm-deep PhC (red curve). (b) Modal absorption coefficient for the CLM (left ordinate axis) and bulk absorption (right ordinate axis) of the InGaN-based QWs as a function of energy.

GaN slab.

Assuming that the QW reabsorption and the PhC diffraction are the most important loss mechanisms for the CLM, one can define the extinction length as a function of energy:

$$L_{extinction}(\mathrm{E}) = \frac{1}{2k''(\mathrm{E}) + \alpha(\mathrm{E})}$$

Where $\alpha(\mathrm{E})$ is the modal QW absorption coefficient per length as a function of the mode energy. Here, the experimentally measured value of the extinction length is a function of two unknown parameters ($2k''(\mathrm{E})$ and $\alpha(\mathrm{E})$). In order to decouple them one can consider either a second set of measurements (For example the mode intensity decay while traveling away from the contact) or to obtain one of them by a numerical simulation. Here, CLM extraction length as a function of the energy is calculated from the complex in-plane wavevector of the Bloch modes supported in the structure. The numerical simulation is based on scattering-matrix formalism and considers the exact 3D structure (the nominal values are described above) [4, 5]. The theoretically determined extraction length of the CLM is shown in Figure 3-5a (red line). As a result, the QW absorption length can be deduced from the extinction and extraction length curves by using the following relation:

$$L^{-1}_{absorption}(\mathrm{E}) = L^{-1}_{extinction}(\mathrm{E}) - L^{-1}_{extraction}(\mathrm{E})$$

Where the absorption length is defined as $L_{absorption}^{-1}(\mathrm{E}) = \alpha(\mathrm{E})$. The latter is presented also in Figure 3-5a (green line). Here one can briefly comment on the importance of this information. For example, one can see that for the 95 nm deep PhC (extraction shown with wavy line in Fig 5a) for energies above 2.92 eV the QW absorption is a more efficient extinction mechanism than the PhC extraction. On the other hand, the shorter extraction length obtained for the common 150 nm deep PhCs (thick solid line in Figure 3-5a) allows efficiently pulling light out of the mode before it gets reabsorbed in the QW. Finally one can use the modal QW absorption coefficient $\alpha(\mathrm{E})$ to estimate the absorption coefficient of the InGaN QW by $\frac{\alpha(\mathrm{E})}{\Gamma_{CLM}}$, assuming that Γ_{CLM} does not vary significantly over the range of energies considered. The modal and volume absorption coefficients are shown in Figure 3-5b. While this is the first direct measurement of the modal absorption in optoelectronic devices, the estimated absorption coefficient of the InGaN QWs is in agreement with previous results [6, 7].

In conclusion, we developed a unique technique for experimental determination of the modal extraction length. This methodology represents an important tool for modal engineering that allows a thorough analysis of the extraction and dissipation properties of guided modes in PhC LEDs.

1. David, A., et al., *Photonic crystal laser lift-off GaN light-emitting diodes.* Applied Physics Letters, 2006. **88**(13): p. 133514-3.
2. David, A., H. Benisty, and C. Weisbuch, *Optimization of Light-Diffracting Photonic-Crystals for High Extraction Efficiency LEDs.* J. Display Technol., 2007. **3**(2): p. 133-148.
3. Matioli, E., et al., *GaN-based embedded 2D photonic crystal LEDs: Numerical optimization and device characterization.* physica status solidi (c), 2009. **6**(S2): p. S675-S679.
4. David, A., et al., *Photonic bands in two-dimensionally patterned multimode GaN waveguides for light extraction.* Applied Physics Letters, 2005. **87**(10): p. 101107-3.
5. Tikhodeev, S.G., et al., *Quasiguided modes and optical properties of photonic crystal slabs.* Physical Review B, 2002. **66**(4): p. 045102.
6. Renner, F., et al., *Quantitative analysis of the polarization fields and absorption changes in InGaN/GaN quantum wells with electroabsorption spectroscopy.* Applied Physics Letters, 2002. **81**(3): p. 490-492.
7. Kvietkova, J., et al., *Optical Investigations and Absorption Coefficient Determination of InGaN/GaN Quantum Wells.* physica status solidi (a), 2002. **190**(1): p. 135-140.